DEVELOPMENT OF A PRELIMINARY DESIGN AND A ONE-DIMENSIONAL MODEL FOR A DIRECT CONTACT HEAT EXCHANGER

A Dissertation
Presented to
The Academic Faculty

by

Abdullah Ali Mohammed Ba Gunaid

In Partial Fulfillment
of the Requirements for the Degree
Master of Science in the
School of Mechanical Engineering

Georgia Institute of Technology
December 2022

DEVELOPMENT OF A PRELIMINARY DESIGN AND A ONE-DIMENSIONAL MODEL FOR A DIRECT CONTACT HEAT EXCHANGER

Approved by:

Dr. Sheldon M. Jeter, Advisor
School of Mechanical Engineering, retired
Georgia Institute of Technology

Dr. Said I. Abdel-Khalik
School of Mechanical Engineering
Georgia Institute of Technology

Dr. Hany A. Al-Ansary
School of Mechanical Engineering
King Saud University

Date Approved: December 05, 2022

To the source of my happiness, strength, patience, and hope, my mother and father

ACKNOWLEDGEMENTS

I would like to take this opportunity to thank my academic adviser, Professor Sheldon Jeter, for his genuine care, ongoing support, utter inspiration, and unending encouragement during my master's program. Professor Jeter has not only guided me through my studies and helped me enhance and broaden my knowledge, but he has also assisted me in taking care of my health when necessary. I learned how to carry out research, assess issues, tackle them, and have an engineering mentality while working under his supervision. I would also like to express my gratitude to Professor Said Abdel-Khalik and Professor Hany Al-Ansary for participating on the reading committee for my thesis. I am very appreciative of their time and work in assisting and guiding me with my thesis. I would also like to thank Hadramout Foundation for supporting me throughout my education and looking out for me. Finally, I will never be able to adequately thank my mother, father, siblings, and friends for everything they have given me along this trip; I am fortunate to have them in my life.

TABLE OF CONTENTS

LIST OF TABLES

LIST OF FIGURES

LIST OF SYMBOLS AND ABBREVIATIONS

F_p Total force acting on the particle

F_g Gravity force of the particle

F_D Drag force on the particle

F_b Buoyancy force of the particle

m_p Mass of the particle

ρ_p Density of the particle

V_p Volume of the particle

ρ_{air} Density of the air

C_D The drag coefficient

A_{CS} The particle projected area normal to the direction of the movement

V_{rel} The relative velocity of air with respect to particle

V_{ter} Terminal velocity of the particle

Re_p Reynold's number of the particle

D_p	Diameter of the particle
μ_{air}	Dynamic viscosity of the air
$\dot{Q}$	Heat transfer rate
h	The heat transfer coefficient
$A_{p,s}$	The particle surface area
T_p	The particle surface temperature
T_{air}	The air temperature
Nu	Nusselt number
k	The gas (air) thermal conductivity
Pr	Prandtl number
μ_s	Dynamic viscosity evaluated at the particle surface temperature
$\rho_{p,bulk}$	Bulk density of particles
$V_{p,hy}$	Hydrodynamic volume of particle
f_{SV}	The fraction of particle solid volume
f_{VV}	The fraction of particle void volume
S	Allowable stress

σ	Ultimate tensile stress
SF	Safety factor
UA	The total thermal conductance
U	Overall heat transfer coefficient
$LMTD$	Log mean temperature difference
ΔT_{air}	Air temperature difference
ΔT_{p}	Particle temperature difference
ρ_{N}	The particle number density, the number of particles in control volume per volume unit
$\dot{m}_{ECM}$	Mass flow rate of particles (energy carrier medium)
$A_{CS,DCHX}$	Cross sectional area of direct contact heat exchanger
V_{air}	Velocity of air
$\dot{m}_{air}$	Mass flow rate of air
V_{p}	Velocity of particle
$A_{CS,p}$	Cross sectional area of particle
$\vec{n}$	The unit normal vector
P_{Bot}	Pressure at the bottom of the heat exchanger

P_{Top}	Pressure at the top of the heat exchanger
ΔP_{DCHX}	Pressure drop of the heat exchanger
$F_{\text{g,ECM}}$	Weight of the energy carrier medium (particles) in the heat exchanger
ΔP_{drag}	Pressure drop due to drag
ΔP_{mom}	Pressure drop due to momentum
C_{air}	Heat capacity rate of the air
C_{ECM}	Heat capacity rate of the energy carrier medium

SUMMARY

A physics-based, one-dimensional model of a direct contact heat exchanger (DCHX) that is suited for use in a concentrated solar power (CSP) system that is based on a central receiver power tower (CRPT) particle heating receiver (PHR) is created. In the course of the study, CRPT systems were analyzed, including molten salt, water, air, and particulates. There are a variety of alternate designs for the particle-to-fluid heat exchanger (PFHX), which are discussed in this thesis. In this study, more investigation was conducted into the falling particle DCHX and its performance. A one-dimensional model is constructed using equation-solving software to simulate the thermal and fluid behavior of a monodisperse particle-to-fluid direct contact heat exchanger (DCHX). Literature research has been conducted on the available high-temperature materials and alloys, which could be used to manufacture the heat exchanger's body that operates at extremely high temperatures and moderate pressure. The thermal and fluid dynamical performance is presented, including the total heat transfer coefficient, the temperature and velocity of the one-size particles and the air, and the pressure drop. It was shown that particles with a diameter of 0.6 mm generate much better results than those with 0.3 or 0.9 mm in diameter. According to the parametric experiments' findings, increasing the terminal temperature difference or the particle mass flow rate results in an improvement in the DCHX's thermal performance. Additional parametric tests were conducted to investigate the heat exchanger's performance in various circumstances. Ultimately, a preferred concept is identified and justified.

CHAPTER 1. INTRODUCTION

The energy demand has increased exponentially over the past few decades due to technological advancements and the increased use of energy to power various devices in homes, workplaces, and industries. Population and economic growth are predicted to result in a rise in global energy consumption and carbon dioxide emissions related to energy use through 2050 if current policy and technological trends continue [1]. In 2021, utility-scale electricity generation plants in the United States produced around 4,116 billion kWh of electricity [2]. Coal, natural gas, petroleum, and other gases accounted for approximately 61% of this energy output. 20% was obtained from renewable energy sources, while 19% was derived from nuclear energy [2]. Governments must endeavor to transition to more sustainable energy sources because of climate change, dwindling natural resources, and tense political environments.

In 2021, diverse solar technologies produced 115 billion kWh, or 2.8% of U.S. energy production [2]. Concentrated solar power (CSP) is one potential technology that could enhance the amount of energy generated from solar sources. CSP uses a series of mirrors or lenses to concentrate direct solar irradiance from a broad area onto a smaller region. This causes the radiation to be concentrated in a small space, resulting in the concentration of energy. Then, this energy is used to raise the temperature of an energy carrier medium (ECM), which transfers the heat to a working fluid that is then employed in generating electricity. Because CSP technology utilizes direct solar irradiation, it would be most effective in environments like deserts where there will not be many clouds. CSP systems are typically combined with storage or a hybrid system to continue functioning at night [3]. Hybrid systems are formed by integrating two types of

technology; for example, a solar power plant and a natural gas power plant can be combined to create a hybrid system. The system will be powered by real-time solar energy throughout the day and stored thermal energy or natural gas in the evening.

1.1 Problem Statement

As energy consumption continues to skyrocket and carbon footprint grows, there is a growing need for renewable energy solutions. Utilizing solar tower power plants to generate electricity using solar thermal energy from the sun is an approach that can help alleviate these problems. Solar tower power plants necessitate an ECM, which the system utilizes to absorb the sun's heat. This ECM is then routed through a heat exchanger to transfer the sun's heat to a working fluid. After passing through a turbine, the working fluid generates power. Importantly due to second law consideration, the greater the fluid temperature, the greater is the system's ability to generate power. An efficient heat exchanger that transfers heat from the ECM to the fluid is required to achieve these elevated temperatures. Most of these facilities now utilize indirect contact heat exchangers with limited surface area. Indirect contact heat exchangers, such as shell-and-tube or shell-and-plate, have a high system cost because they need expensive metal alloys. Therefore, this research aims to develop a direct contact heat exchanger design that efficiently transfers heat from the ECM to the fluid. A greater surface area between the two working components, air and particulates, within the heat exchanger improves the heat transmission between those two substances. This design will also assist minimize the solar tower power plant's running expenses and boost its overall efficiency.

1.2 Objectives

This research aims to develop a direct contact heat exchanger capable of efficiently transferring heat from particles to gas. This thesis will detail the conceptual and preliminary designs of a particle-to-fluid direct contact heat exchanger optimized for use in solar towers. In this context, the performance of the heat exchanger system and a rough approximation of its cost will be estimated.

The conceptual design will evaluate a variety of configurations, including fluidized bed heat exchangers, moving bed heat exchangers, cyclone heat exchanger, and falling particles heat exchangers. Another point of concentration will be placed on the possible materials and alloys employed to manufacture the heat exchanger. The allowable stress and other mechanical and physical parameters of several stainless-steel metals and nickel-based alloys are researched to find the best suitable material for manufacturing this heat exchanger. Studying the particle size effect on the dynamics and thermal performance of the DCHX. In addition, certain parametric studies will be carried out to analyze this heat exchanger's crucial aspects and enhance its effectiveness. A preliminary cost analysis will be conducted to check the feasibility of DCHX.

CHAPTER 2. BACKGROUND

2.1 Solar Thermal Energy

Solar energy consists of two components, the light that comes directly from the sun's rays is the direct component of solar energy. In contrast, the light dispersed through the atmosphere is the diffuse part of solar energy. In conditions with a clear sky, solar insolation from the direct component typically accounts for 60–80 percent of the total solar insolation. This percentage drops with increasing humidity, cloud cover, and atmospheric aerosols such as dust or pollution plumes [4]. Clear skies are ideal for receiving the maximum amount of direct solar insolation.

The use of technologies like CSP plants, which operate on the direct sun component, is restricted to arid regions due to their optimal performance in sites with high levels of direct normal irradiance. Photovoltaic panels, a nonconcentrated solar technology, can employ both direct and diffuse solar components and can be installed in a wider variety of geographic locations. The following map illustrates the daily and annual amounts of direct normal solar irradiation received around the planet [5].

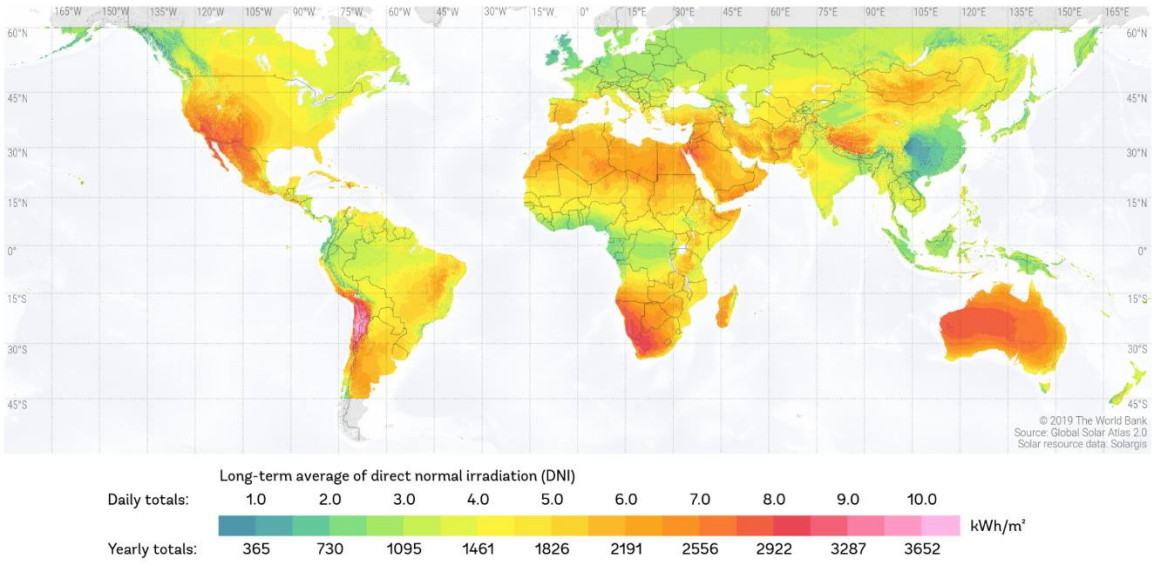

Figure 1. Normal direct solar irradiation map [5].

2.2 Solar Energy Potential and Technologies

Deserts cover 20% of Earth's land area [1] and get an average global horizontal solar irradiance of 5.5 kWh/m^2 [1]. The annual average global horizontal solar irradiance that is received by the arid area is 2008 kWh/m^2. Therefore, the annual total energy received by the arid area is 6.103×10^{16} kWh which is equal to 2.197×10^{14} GJ, mostly consisting of beam radiation useful for CSP. In 2019, the global primary energy consumption was around 6.372×10^{11} GJ [3]. Thus, the ratio of the annual energy received by the arid area to the global consumption is 345.

Two approaches can be taken to harness the sun's energy to generate power directly. The first technology focuses the sun's heat on a particular region and then utilizes the concentrated energy to operate a heat engine. There are four primary types of concentrated solar power plants: solar towers, parabolic trough power plants, Fresnel lens plants, and solar dishes. A combined cycle gas turbine facility may also incorporate a concentrated solar power mechanism into its operations. The second technology involves absorbing the energy in a device, such as solar cells,

to generate electricity by collecting and converting the light energy into electricity. Solar cells are the third most major renewable source of electric power behind hydropower and wind power [6]. CSP technologies will be the subject of immediate attention throughout the following sections.

2.3 Solar Cells

Solar cells are utilized to directly convert solar radiation into electricity. They are commonly known as photovoltaics (PV) cells because the light, photons, is converted into electrons, voltage. A solar cell comprises two adjacent layers of two silicon-based semiconductors created by injecting impurities into the silicon to enhance the electrical conductivity. The p-type layer is silicon doped with elements possessing one fewer electron at its outer energy level than silicon, such as boron, to form an electron vacancy, a hole, at the outer energy level. The n-type layer is silicon doped with elements, such as phosphorus, that have one additional electron at its outer energy level than silicon to have a free electron at the outer energy level. Near the junction of the two layers, the excess electrons in the n-type layer migrate to the p-type layer to fill the excess holes, forming a depletion zone [7]. Due to the mobility of the electrons, the p-type side now includes negatively charged ions, whereas the n-type side has positively charged ions. The existence of these ions with opposing charges generates an internal electric field that inhibits electrons in the n-type layer from filling holes in the p-type layer. However, when sunlight, electromagnetic radiation, strikes a solar cell, electrons gain energy, overcome the electric field, and move to fill a hole in the p-type layer. Hence, a flow of electricity is created by connecting the n-type and p-type layers with a metallic wire [7]. Solar panels are constructed by connecting several individual solar cells, while solar arrays are comprised of multiple solar panels joined together. The functioning procedure of the solar cells is illustrated in Figure 2 [8].

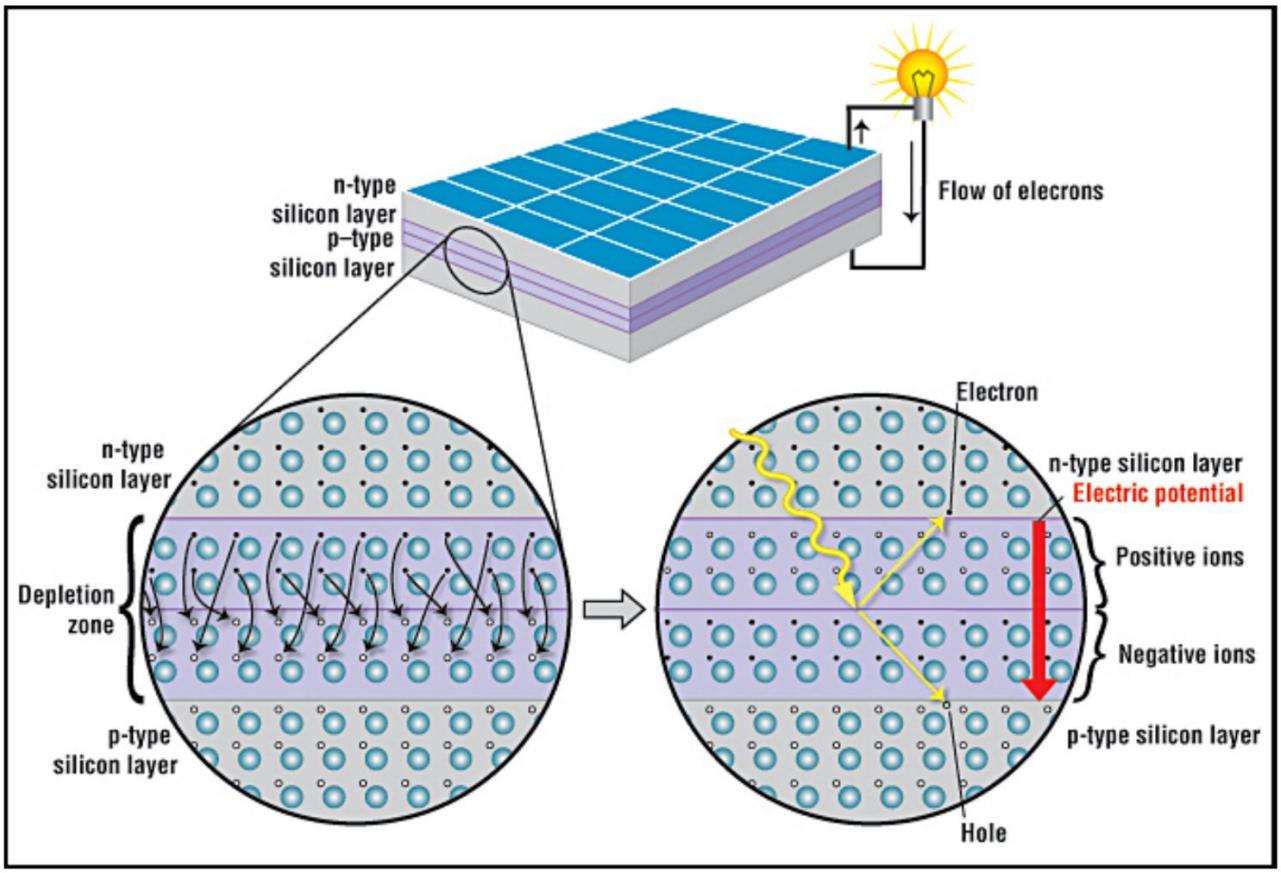

Figure 2. Schematic of solar cell [8].

2.4 Duck Curve

Before solar energy generation developed, utility corporations were efficient at predicting electricity demand. They provide the smallest amount of power overnight, scale up in the morning, and then offer the most energy around dusk when energy consumption peaks. Utility companies update their energy demand models periodically to operate as optimally as possible. However, introducing renewable energy, particularly solar energy, has begun to cause complications in these energy demand models.

In 2010, solar energy installations accelerated in California [9]. Researchers observed that midday is when the sun produces the greatest energy; hence, the demand curve falls when the new midday production is factored in, as demonstrated in the graph below. New solar capacity is added annually, causing midday curves to decrease. Researchers named this drop in energy demand "duck curve," causing two problems. First, when the sun sets, solar energy production ceases just as energy demand peaks, making it extremely challenging for utility providers to immediately increase energy production. Second, the power plants are most cost-effective when they are continuously operating, and if they must be shut down at midday, their economy will be severely harmed [9].

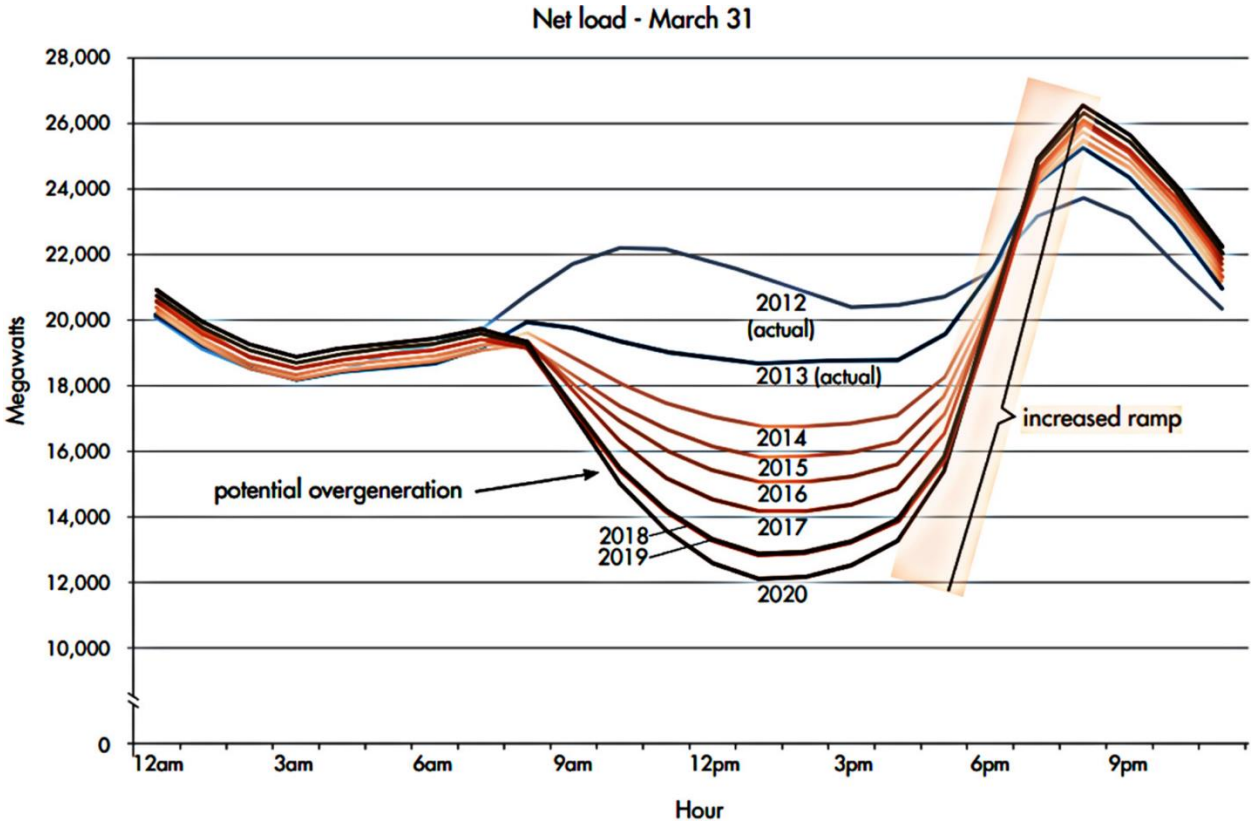

Figure 3. Duck curve showing steep ramping needs and overgeneration risk [9].

If solar power generation exceeds demand, grid operators must turn off some solar panels. They are wasting solar energy unless they risk overloading or causing damage to the electricity system. Consequently, improved models for forecasting energy demand and energy storage are required to overcome this problem.

2.5 Energy Storage

Energy storage is a technique of catching the energy, storing it as chemical, thermal, or mechanical energy, and then releasing it when necessary. Energy storage is not 100% effective since some energy is always wasted during conversion and retrieval. Nevertheless, it enables the flexible use of energy at other times than when it was originally generated. Because of the intermittent nature of solar energy, energy storage is necessary to maximize its utilization and ensure its continuity after sunset. Electrochemical storage, batteries, is most often paired with photovoltaic power plants, whereas thermal storage, fluids, is most often paired with CSP plants [10].

Lithium-ion batteries are the most prevalent because they last longer, require less maintenance, and occupy less space than alternative solar energy storage systems. On the other hand, batteries are utilized for energy storage in residential settings, and their cost is still relatively high [11].

Thermal energy storage is a technique in which a fluid, ECM, is used to store heat. This ECM is, after that, kept in an insulated tank until the energy is required. The ECM can be used directly for heating and cooling or indirectly to produce power. The ECM is employed to boil water, and the generated steam runs a turbine and generates electricity using the same equipment as traditional power plants. Thermal energy storage is advantageous and functional in large-scale CSP facilities [12].

2.6 Concentrated Solar Power

The main components of CSP plants are a sun concentrating system, a receiver, a thermal energy storage system, and a thermodynamic cycle coupled to generate power. Concentrating solar power systems utilize mirrors or lenses to focus the sun's direct beam radiation to generate valuable forms of energy such as heat, electricity, or fuels through various downstream technologies. The heat from the sun is collected, concentrated, and then used in a heat engine. If the heat engine is a traditional steam turbine, the heat will be used to produce steam to power the turbine. Nevertheless, the heat engine is also possible as a Sterling engine, a gas turbine, or a closed-cycle turbine system that uses an organic thermodynamic fluid. There are four primary methods of CSP currently in operation, each identified by the technology employed to concentrate the sun's heat energy.

- Parabolic trough
- Fresnel reflectors
- Solar dishes
- Solar towers

The ability to store the hot ECM in a thermal energy storage system and then use it after the sun has set is advantageous. Each technology offers unique benefits and, in some circumstances, distinct market niches. The following sections will elaborate on various aspects of these technologies.

2.6.1 Parabolic Trough

Parabolic trough-shaped mirrors provide a linear focus on a receiver tube aligned with the parabola's focal line, as shown in Figure 4. Mirrors and the receiver are positioned on a single axis of a structure that follows the sun's motion throughout the day. Seasonal changes in how the sun moves on the other axis cause the line focus to move sideways. The focus stays on the receiver,

but some spill can occur at the row ends. Consequently, the incident path will be slightly longer, resulting in a picture that is a little less focused [13].

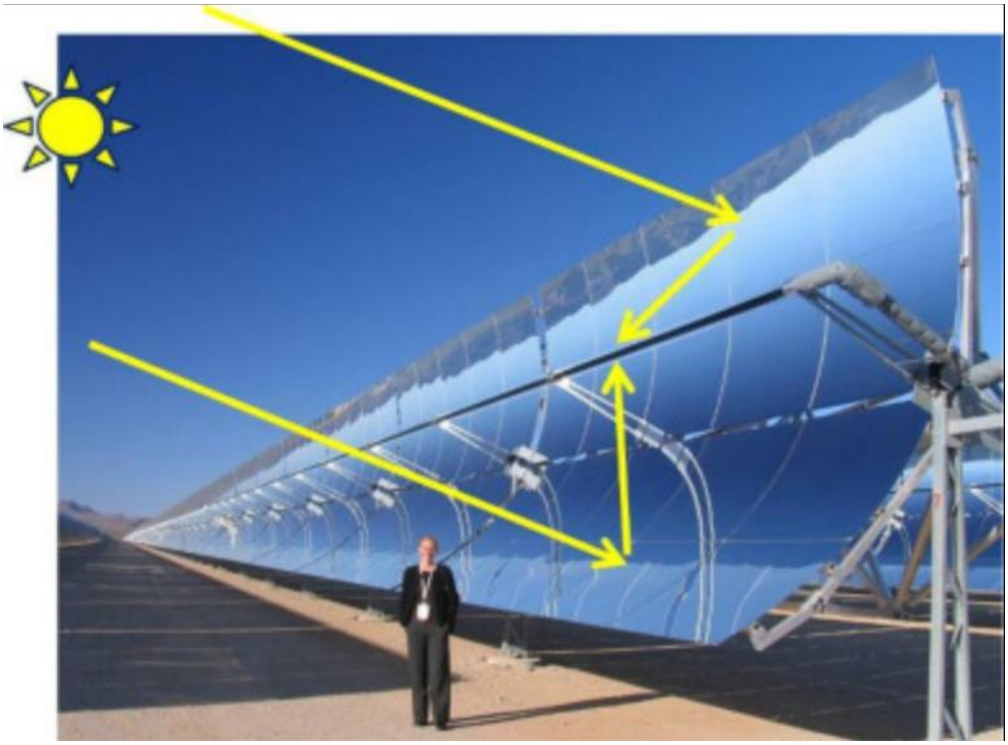

Figure 4. Parabolic trough solar collector [13].

Currently, the most used CSP technology is trough systems that collect thermal energy using evacuated tube receivers. In this setup, it is typical to use oil as the heat transfer fluid, which is subsequently circulated to a central power unit for use in power generation [13].

2.6.2 Fresnel Reflectors

The Fresnel lens addresses the costly and complex nature of mass-producing conventional lenses. In solar systems, the Fresnel lens is a less expensive alternative to the parabolic trough and

has been widely used in photovoltaic systems. The Fresnel system comprises a series of long, nearly flat reflectors that simulate the shape of a parabolic trough, as Figure 5 shows. Each individual reflector is positioned so it can track the sun, and the energy it receives is concentrated onto a fixed pipe that runs along the length of the trough, directly above the reflectors [6].

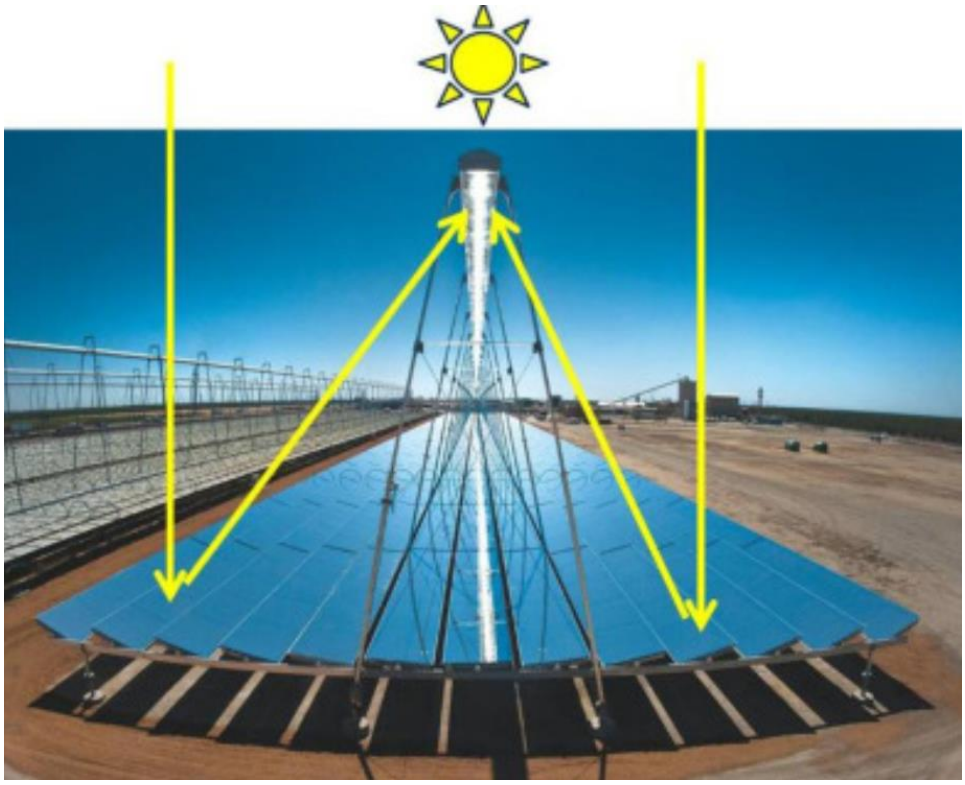

Figure 5. Fresnel reflectors field [6].

Direct steam generation is typically implemented at Fresnel power plants to increase operational efficiency and reduce operating costs. According to reports, they use substantially less space than conventional trough plants [13].

2.6.3 Solar Dishes

The solar dish is a parabolic reflector, comparable to a satellite antenna, but with a heat engine instead of a microwave receiver at its focal point. The parabolic shape concentrates sunlight on a specific location where a heat receiver is located. The dish and its engine are fixed to a framework that allows it to follow the sun throughout the day. The heat collected is proportional to the dish's diameter, with contemporary dishes having a diameter of fewer than 10 meters. The solar dish can be individually installed or deployed in more significant numbers to create more electricity. The schematic of a typical solar dish is depicted in Figure 6 [14].

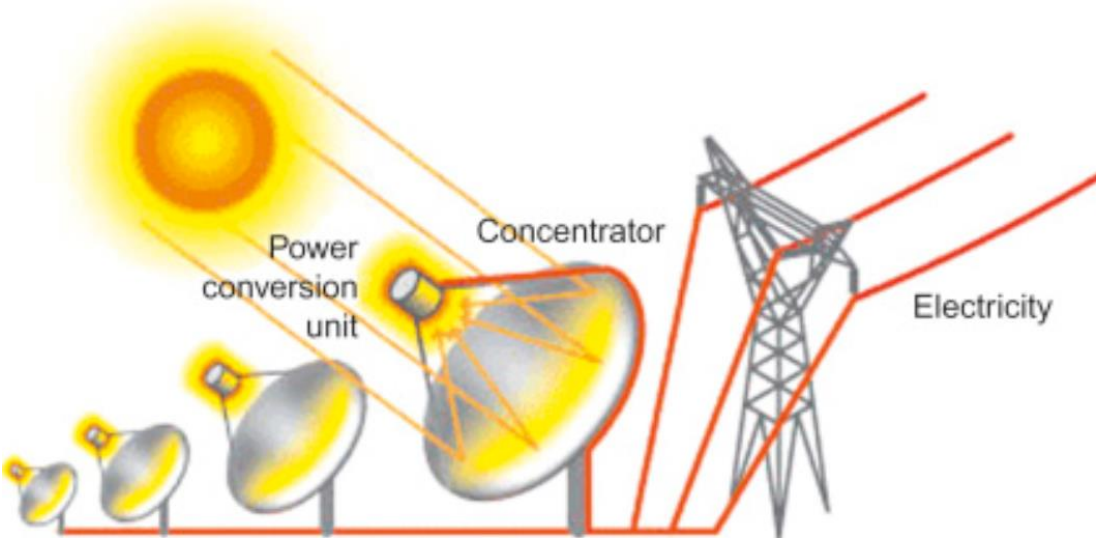

Figure 6. Solar dish plant [14].

Most solar dishes generate electricity through the utilization of small heat engines. However, solar dish systems might be built to generate steam to power steam turbines. The simplicity and effectiveness of solar dishes are their primary benefits. Single solar dishes can have >30% energy conversion efficiency, far higher than any other solar thermal technology; however, they suffer due to lack of any significant economy of scale [14].

2.6.4 Solar Towers

Solar towers, known as central receiver power tower (CRPT), use a unique collecting field and receiver layout to focus the sun's energy with high concentration ratios, resulting in high temperatures. The parabolic trough system employs a distributed heat collecting mechanism, whereas the solar tower concentrates heat onto a central unit. A large solar energy receiver and heat collector are mounted on top of the tower, which is centered in a field of heliostats. This heliostat field is operated to focus the sunlight that reaches it onto the receiver mounted atop the tower. The solar tower can utilize molten salt, water, air, or particulates as the ECM for its energy collection. Figure 7 is an illustration of a solar tower plant [15].

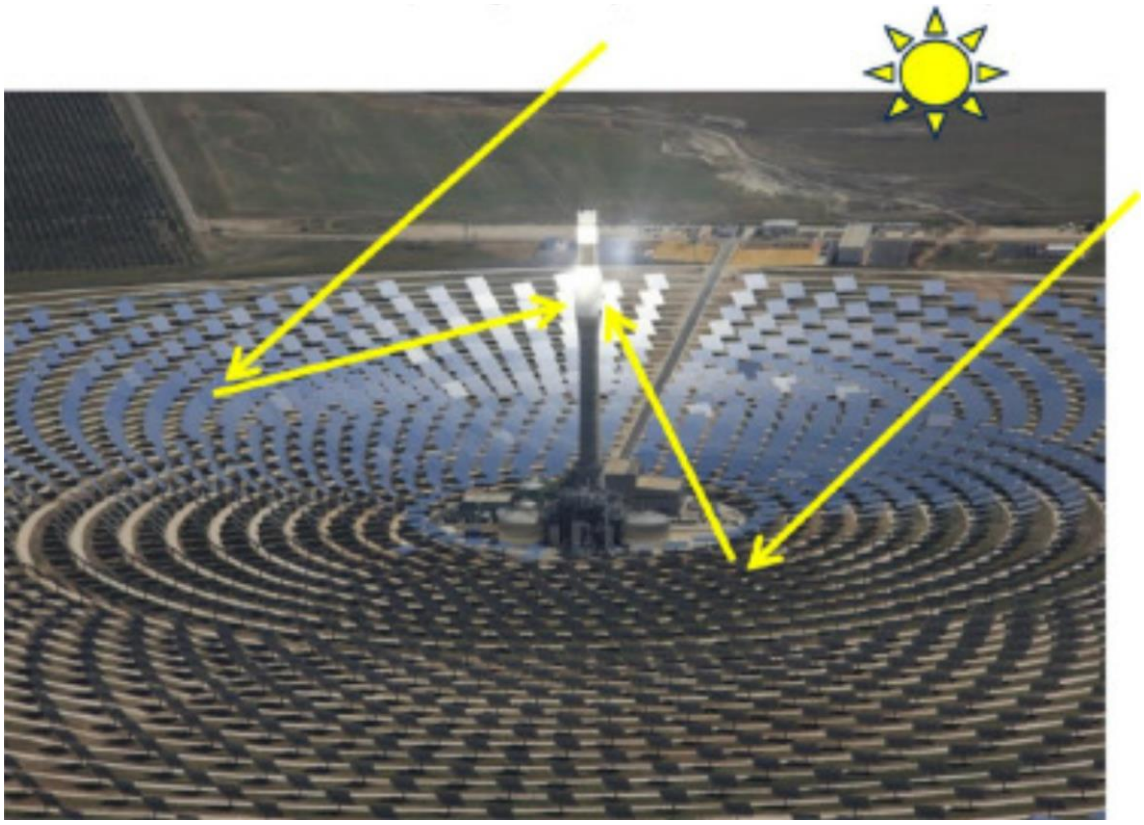

Figure 7. Solar tower plant [15].

Compared to CSP facilities, the combination of solar towers with high-temperature cycles improves the efficiency of solar radiation to electricity conversion.

The table below provides a comparison of these various CSP systems to gain a better grasp of their respective advantages [16].

Table 1. CSP technologies comparison [16].

Parameter	Parabolic trough	Fresnel reflectors	Solar dish	Solar tower
Capacity (MW)	10–200	10–200	0.01–0.40	10–200
Concentration ratio	25–100	70–80	1000–3000	300–1000
Land use (m^2/MWh/year)	6–8	4–6	8–12	8–12
Collector concentration	70-80 suns	>60 suns	>1300 suns	>1000 suns
Annual solar-to-electric efficiency (%)	12–16	8–10	20–35	20–35
Operating temperature of solar field (C)	290–550	250–560	120-1500	250-650
Technology maturity	Commercial	Pilot projects	Demonstration projects	Pilot commercial projects

These technologies provide significant benefits, but the solar tower stands out as the most appealing option. This thesis will focus more on solar towers and the technologies and components that go into making them.

2.7 Energy Carrier Medium for Central Receiver Power Tower

The CRPT, the solar tower, is currently the second-most commercialized CSP technology. The solar energy is focused on a central receiver atop a tower by a heliostat field so that the ECM can reach a remarkably high temperature. The ECM, heat transfer fluid, is a key component of solar tower systems serving as the receiver heat transfer medium and storage medium for the solar

tower. Once the ECM has reached a high temperature, it can be stored for use after sunset to spin a turbine for large-scale power production [17]. CRPT uses several ECM, including molten salts, water, air, and particles.

2.7.1 Molten Salts

Conventional molten salts are 60% sodium nitrate and 40% potassium nitrate [17]. Salts are solid at ambient temperature and air pressure, and they dissolve at about 220°C when thermal energy is imparted [18]. Throughout the energy storage process, the liquid state of the molten salt is maintained. In solar tower plants, the working and storage temperature for molten salts can reach up to 565°C, decreasing the cost of specific storage capacity and electricity output compared to parabolic troughs [18]. However, the corrosion behavior of molten salts increases as the temperature rises, necessitating the use of costly specific alloys in the receiver, storage tank, heat exchanger, and tubes to prevent corrosion. Furthermore, the highest working limit of 565°C limits the use of high-efficiency thermodynamic cycles, while the high solidification temperature of 220°C requires electric heating to prevent solidification. [18, 19].

2.7.2 Water

Water and steam have been employed for a long time in power cycles. It could be used as ECM because steam's specific heat capacity, thermal conductivity, and viscosity are exceptional. Additionally, the water use in CRPT application is cost-effective due to the absence of a heat exchanger between the receiver and the power cycle [20]. Hence, the steam turbine is operated by the steam directly extracted from the receiver. The surplus amount of steam could be stored in tanks for later use. Nevertheless, the use of water in solar towers presents several challenges. At elevated temperatures, steam becomes unstable, difficult to control, and corrosive, necessitating costly alloys to prevent corrosion. Also, the enormous amount of steam requires massive storage

tanks, rendering the concept impractical. Furthermore, the restricted water supply in arid places precludes its usage as an ECM [20].

2.7.3 Air

In solar tower plants where air serves as the ECM, the receiver is a volumetric external receiver. The air receiver can be either open atmospheric air or pressurized air with a closed loop. Air may be utilized in solar towers since it is non-hazardous, abundant, inexpensive, and stable [21]. Moreover, solar towers with air as ECM can readily combine with a Brayton cycle. The heated air is immediately used to drive a gas turbine that generates power, while the excess is stored in tanks for future use. In contrast, air's thermal characteristics and efficiency are inferior to molten salts and steam. Additionally, storing hot air is difficult due to its vast volume [21].

2.7.4 Particulates

In the 1980s, particulates or powders were proposed as heat transfer and heat storage mediums to overcome the shortcomings of molten salts, steam, and air [22]. Solid particles, such as sand, possess a high specific heat, superior thermal and chemical resilience and stability at elevated temperatures, and cheaper material costs. In addition, their operating temperatures can reach up to 1,000°C. This leads to an increase in the overall efficiency that can be attained from the thermodynamic cycle. In this design, cold particles from a cold particle storage tank are heated in a solar receiver before being stored in a hot particle storage tank for use at night. At night, the heated particles are utilized to heat air, which is then used to spin turbines and generate electricity. The higher the particle temperatures, the hotter the air may become and the greater the efficiency of power generation. In conclusion, the volume of particle research is expanding due to the particles' immense potential as ECM and energy storage [22, 23].

2.8 System Description of RTV Solar Tower

The Riyadh Techno Valley (RTV) solar tower, constructed in Saudi Arabia, mainly consists of a heliostat field, receiver, storage bins, heat exchangers, and ECM [24]. The solar tower is surrounded by a field of mirrors called the heliostat. On the highest point of the tower, there is a particle heating receiver (PHR). The tower structure contains cold and hot storage bins and heat exchangers, whereas the particle lift system will be external. This solar tower's ECM is particles of the material Accucast ID50. The figure below shows this solar tower.

Figure 8. RTV solar tower [24].

In the RTV solar tower system, the heliostats concentrate the solar irradiance on the top of the solar tower, where the PHR is positioned. A particle lift system will convey the particles from the cold storage bin to the PHR. Particles fall inside the PHR to capture the reflection of sunlight and get heated by an endothermic reaction [24]. After leaving the PHR, the heated particles are transferred to a hot storage bin, positioned above the heat exchanger, and kept for use in the evening. At night, the hot particles exit the hot storage bin and pass through a heat exchanger to

transfer the heat to the air. This heat exchanger is connected to a power cycle, so the heated air is used to drive a gas turbine and generate electricity. After the heat transfer process between the particles and air, the particles are deposited in a cold storage bin, located underneath the heat exchanger, and the entire process is repeated [24]. The figure below is a schematic of RTV solar tower with more details.

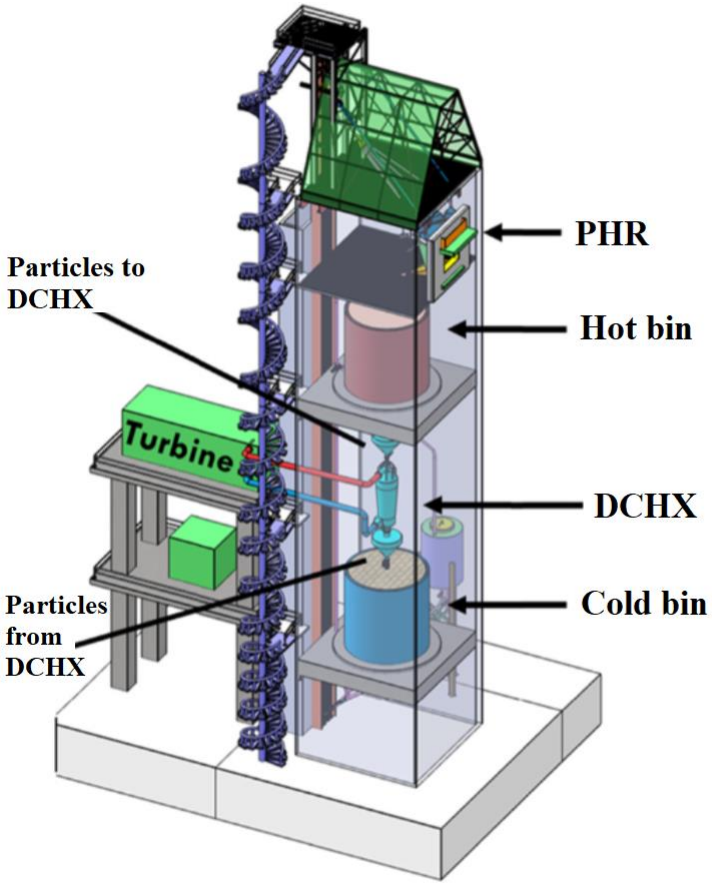

Figure 9. Schematic of RTV solar tower [24].

2.9 Heat Exchangers

In various applications, when two fluids have different temperatures, they undergo a heat exchange process. In addition to heating and air conditioning, power generation, waste heat recovery, and chemical processing, heat exchange takes place in many applications. The heat exchanger is the device that is utilized to conduct this exchange. There are various categories of heat exchangers based on construction, flow arrangement of working fluids, and contact between the working fluids. The simplest heat exchanger consists of concentric tubes in which hot and cold fluids flow in the same direction, called a parallel flow heat exchanger. However, when these two fluids flow in opposite directions, it is called a counter-flow heat exchanger. When a solid wall separates the working fluids, it is called an indirect contact heat exchanger. On the other hand, when the working fluids inside the heat exchanger's body are in immediate contact, it is called a direct contact heat exchanger [25].

Conventional heat exchangers with indirect contact maintain the separation of working fluids throughout the heat exchange process. Typically, these exchangers use metal tubes, plates, or walls to separate hot and cold fluids. Due to the designer's ability to accommodate various pressures and temperatures, tubular and plate heat exchangers, indirect contact heat exchangers, are extremely common. A Shell and Tube Exchanger is one of the most prevalent tubular exchangers, consisting of many tubes within a cylindrical shell. Shell and tube heat exchangers are applied in a variety of industries, such as power production, marine applications, and pharmaceuticals, among many others. Although the indirect contact heat exchanger is design-flexible, it would be more effective if the two working fluids were in direct contact.

This CSP project requires an efficient heat exchanger to transfer as much heat as possible from the particles to the air that drives the gas turbine. The higher the heat transfer efficiency

between particles and air, the more effective the thermodynamic cycle and the more energy is generated. Therefore, this thesis aims to develop an effective particle-based direct-contact heat exchanger for a particle-based central receiver tower. The literature review will investigate the characteristics and robust aspects of existing direct-contact heat exchangers and assess their applicability to this project.

CHAPTER 3. LITERATURE REVIEW

3.1 Direct Contact Heat Exchanger

The direct-contact heat exchanger consists of two immiscible fluids of different temperatures brought into direct contact within the body of the exchanger. Without a wall, direct contact heat exchangers could be utilized to transfer heat between two fluid types. One of the two streams in this thesis comprises hot particles, while the other is the air utilized to drive the power cycle. Direct contact heat exchangers offer more benefits than conventional heat exchangers. The design and construction of direct contact heat exchangers are less complicated and more cost-effective. In addition, direct-contact heat exchangers can perform at a low temperature and achieve a greater heat transfer efficiency. It might be described because of the two substances coming into close contact within the heat exchanger, resulting in increased heat transfer rates due to the increased surface area. The elimination of the fouling issue simplifies the maintenance process of the heat exchanger, which is a considerable advantage. The interior design of the heat exchanger prevents the accumulation of any substance within the heat exchanger. Direct contact heat exchangers have been utilized in a variety of applications, including seawater desalination, heat recovery, and ocean thermal energy conversion, and they could be used to harvest solar energy [26, 27].

3.1.1 Fluidized Bed Heat Exchanger

Fluidization is the transformation of solid particles into a fluid-like condition utilizing a fluid medium, such as a gas or liquid. Fluidized beds have existed as a form of a reactor for fluid catalytic cracking, combustion, and heat or mass transfer for more than a century [28]. In a fluidized bed heat exchanger, particles are supported by a grid that prevents them from falling downhill. The concept of a fluidized bed heat exchanger is described as follows: hot particles are supplied into the heat exchanger from the top, while gas enters from the bottom. Gas and particles come into direct contact because the grid that supports the particles allows air to pass through and elevates the particles. The movement of the particles makes them liquid-like, and their constant motion helps them mix with the gas in the bed and enhances heat transfer. Then, the hot air leaves from the top of the fluidized bed heat exchanger while the cold particles exit from the bottom. The fluidized bed heat exchanger may consist of a single bed or multiple stages [29].

Ma and his team [30] created a single fluidized bed heat exchanger to transfer thermal energy from particles to a gas that drives a turbine to generate power. This heat exchanger configuration is shown in the figure below and consists primarily of two concentric shells, annular space between those shells, an internal volume, and a pipe-in-pipe (PIP).

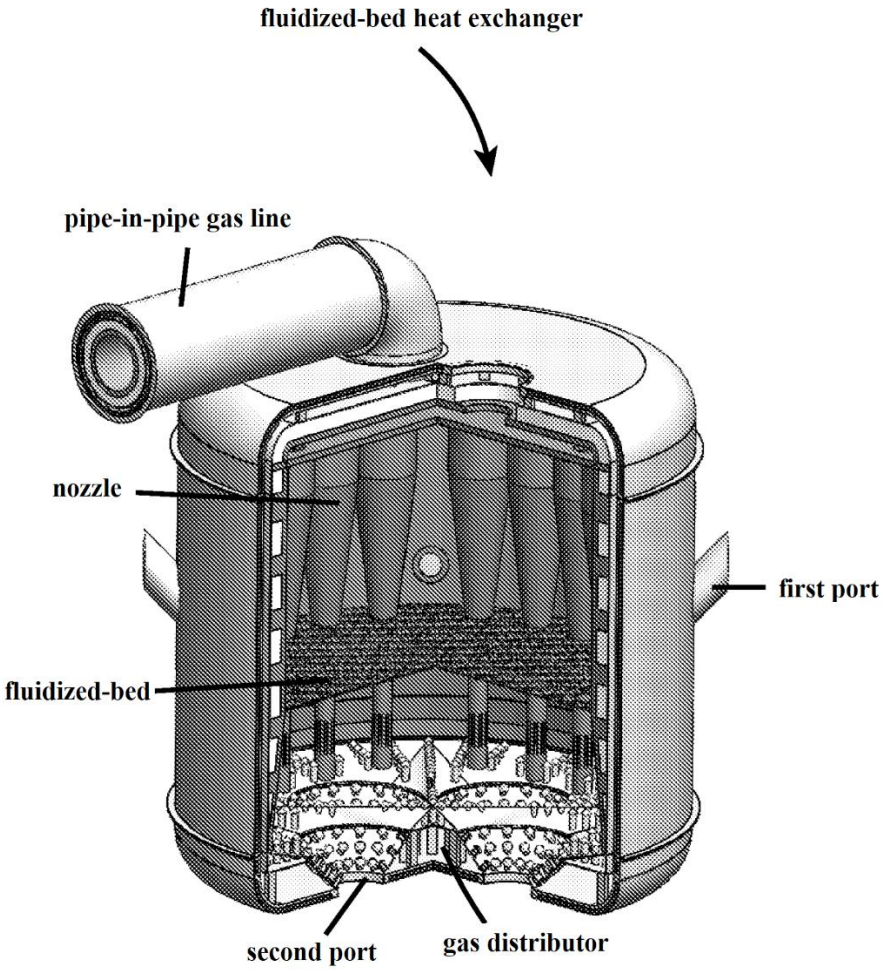

Figure 10. Fluidized bed heat exchanger design as proposed by Ma [30].

The PIP gas line is designed to route the gas stream into the annular space, through a distribution plate, and into the internal volume. Simultaneously, the solid particles enter the internal volume via a first port that penetrates the inner and outer shells. The gas and particles make direct contact in the fluidized bed within the heat exchanger's interior volume. The fluidizing gas velocity of the gas stream through the solids is tuned to maximize the heat transfer coefficient while simultaneously limiting the cross-sectional plan area and, consequently, the size of the inner

annular gap. After the heat transfer process, the cold solid particles are removed from the heat exchanger by flowing gravitationally through the internal volume to a second port on the distribution plate. In the opposite direction, the hot gas flows counter-current to the solid particles to penetrate a higher portion of the internal volume and exit the heat exchanger via the PIP gas line. The hot gas stream exits the heat exchanger at a temperature that may reach the initial 1200°C temperature of the incoming particles and is then used to power the turbine [30].

The Solar Energy Research Institute (SERI) [31] reports a conceptual design and economic feasibility of a direct-contact heat exchanger to heat pressurized air with hot solid particles from a solar thermal central receiver [31]. This design was a multistage fluidized bed heat exchanger with direct contact between the hot particles and the fluidizing gas. A schematic of this conceptual design of the heat exchanger is illustrated in the figure below.

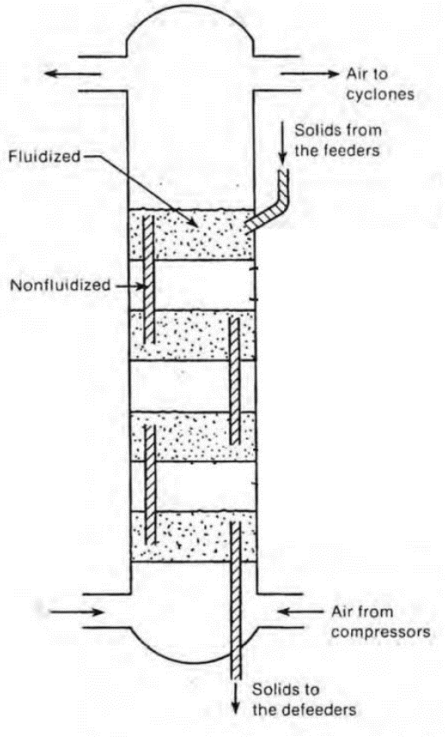

Figure 11. Multistage fluidized bed heat exchanger as proposed by SERI [31].

The system consists of a heat exchanger, feeders, and de-feeders to transport particles into and out of the high-pressure heat exchanger, a few fluidized beds, and a separator to remove any lingering particles from the heated air stream. In this configuration, the pressured air from the compressor enters the system from below and exits from above. Simultaneously, the particles are fed into the heat exchanger through the top feeders, flow in the opposite direction of the fluidizing air, and leave through the bottom de-feeders. In this heat exchanger, the pressurized air fluidizes the particles at every single bed, and because of the particles' constant motion, the heat transfer between them is enhanced. As the particles fluidize, they move from one bed to the next via standpipes connecting the beds. The SERI's report [31] demonstrates the technical viability of this heat exchanger through further research; nonetheless, this multistage design is costly and

challenging to maintain. Due to the irregularity of particle motion and airflow in fluidized beds, cyclone particle separators are required to guarantee that no particles are entrained into the airflow, leaving the heat exchanger. To prevent damage to the turbine, the hot air that enters the turbine must be clear of particulates. The danger of introducing particles into the turbine is significant; however, current experience is that carryover of particles can be eliminated [32]. In addition, suitable ceramic and metallic filters with low pressure-drop have been identified that can reliably protect the turbine from damage. In summary, the SERI influential investigation found DCHXs challenging because of high costs and low technology readiness. Ultimately, this thesis and ongoing research [24, 33] find DCHX technology very promising and deserving further development.

3.1.2 Moving Bed Heat Exchangers

Moving Bed Heat Exchangers are utilized in a multitude of applications involving heat recovery, energy, chemical industries, and filtration [34]. Working fluids of moving bed heat exchangers may be in direct or indirect contact. In the currently utilized indirect moving bed heat exchanger, the particles do not come into contact with the gas or liquid. In contrast, in a direct contact moving bed heat exchanger, the particles come into direct contact with the gas or liquid and then separate upon leaving.

In a direct contact moving bed heat exchanger, particles typically fall from the hot bin into the heat exchanger, move downwards at the same speed as the beds, and then leave the heat exchanger for the cold bin. To provide a uniform flow of particles across the heat exchanger, distribution mechanisms are crucial in the heat exchanger system [35]. In the opposite direction, the gas is pumped up from the bottom. It ascends via the heat exchanger, interacts with the particle beds, and eventually exits the heat exchanger at the top. The airflow might be parallel, moving in

the same direction as the particles, or counter-flow, moving in the opposite direction. The heat exchanger could be vertical or horizontal, depending on the industry. As the airflow interacts with the particle beds, heat transfer occurs; after the heat exchange process is complete, the particulates are removed from the bottom of the heat exchanger, and air is expelled from the top [36].

The particle flow must be managed both inside and outside the heat exchangers. In a vertical configuration, a set of valves is employed between the hot bin and heat exchanger to control the particles entering the heat exchanger. When particles exit the heat exchanger, the second set of valves between the heat exchanger and the cold bin regulates the particles leaving the heat exchanger. Different internal designs of the heat exchanger might be utilized, or the air velocity could be increased to control and delay the motion of the particles to increase their contact with the gas [37].

Over the past several decades, extensive experimental and theoretical research has been conducted on moving bed heat exchangers. Park [35] utilized the finite difference method to conduct a numerical analysis of a moving-bed heat exchanger containing solid particles inside vertical pipes. He employed many flow configurations, including countercurrent, parallel, and cross-flowing moving bed heat exchangers, as shown in the figure below. The most efficient of these heat exchanger arrangements was the counterflow heat exchanger, based on its thermal performance.

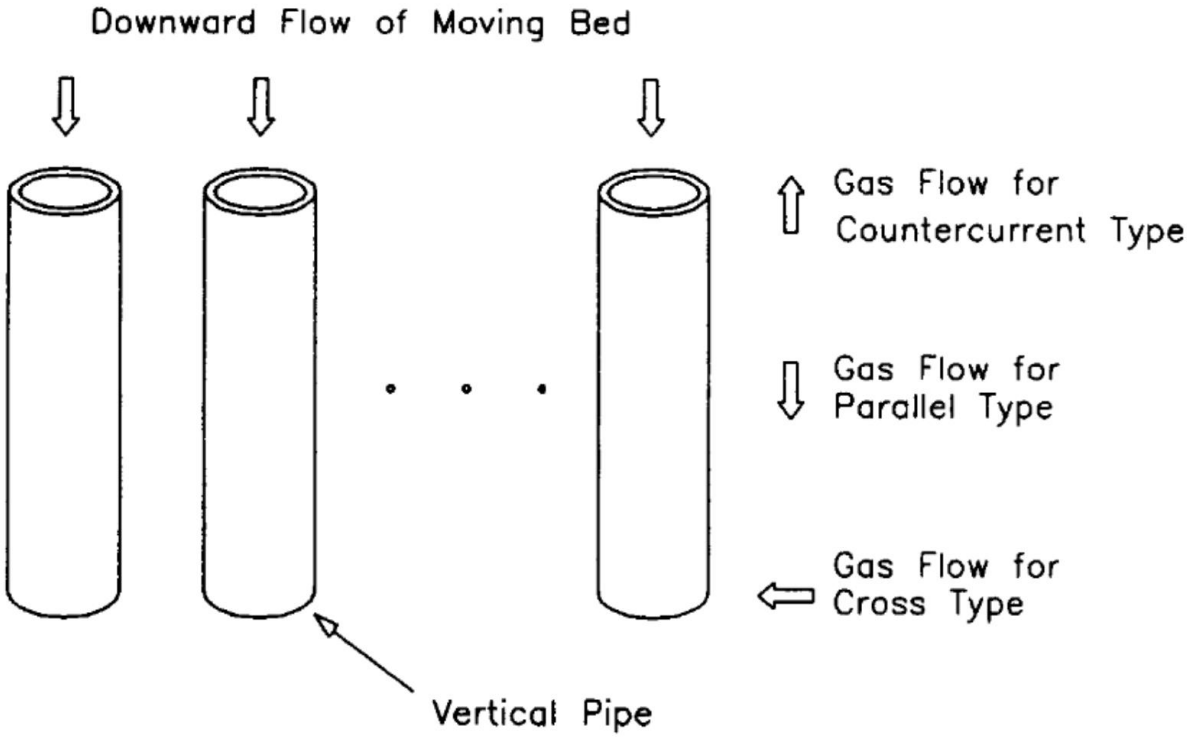

Figure 12. Park's schematic of moving bed DCHX [35].

Hertel and his team [38] investigated numerous models of direct contact heat exchangers to transfer thermal energy contained in particles into the air that can be used to provide heat for industrial processes. The moving bed heat exchanger was determined to be the most efficient for their application. A prototype with a thermal output of 10 kW and an intended air exit temperature of 750°C has been constructed and analyzed. This moving bed DCHX design comprises four counterflow segments. As illustrated in the image below, the particle bed in the DCHX moves vertically within a lamellar structure. In a crossflow process, the airflow flows through the moving particle bed and is heated in four passes. In order to create a homogeneous temperature distribution, mixing chambers are placed after each pass. The gas exits the heat exchanger after the fourth pass, at which point it has attained the desired air temperature.

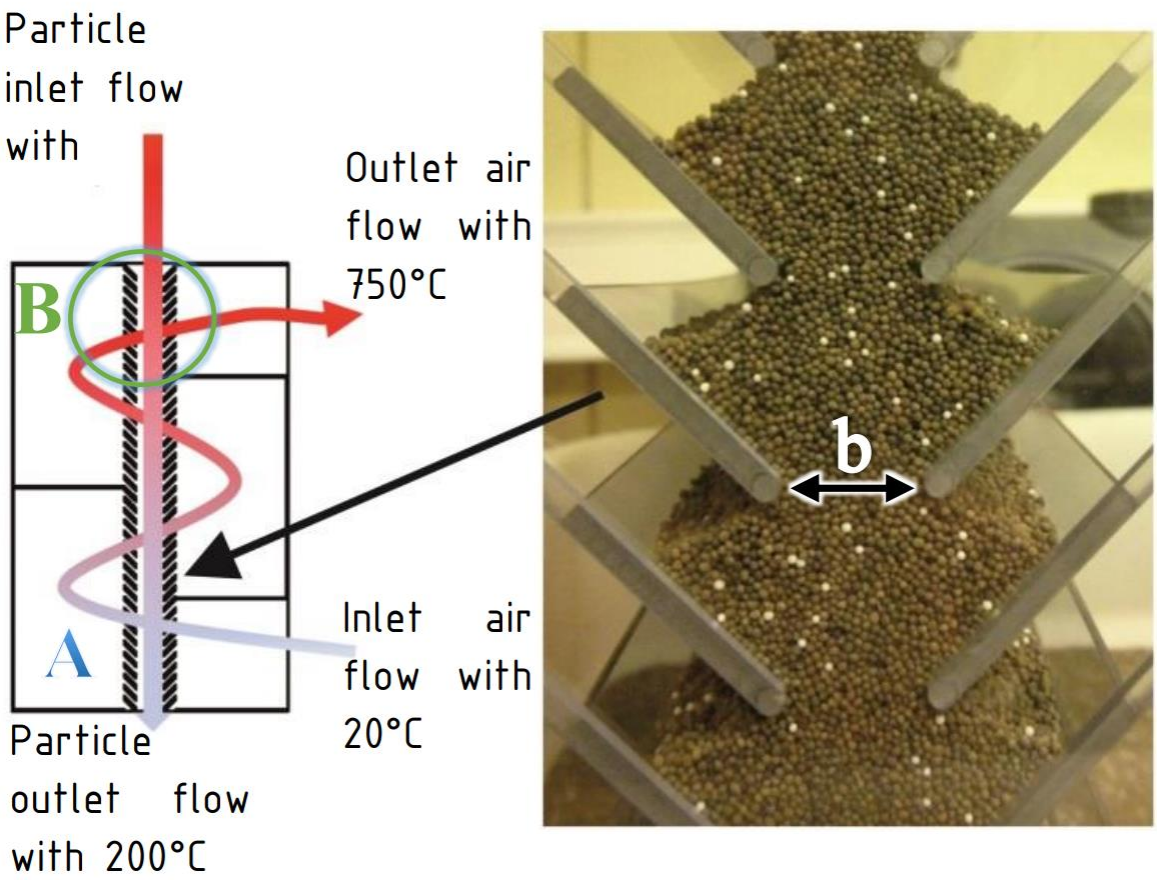

Figure 13. Schematic of the workflow of DCHX with crossflow-section and mixing chambers as proposed by Hertel [38].

Hadley and his team [39] developed a direct contact, countercurrent, moving bed heat exchanger. Using a heat transfer model, they experimentally and numerically examined the performance of the design linked with the solid particles process. As illustrated in the diagram below, the hot particles with a diameter of 1.3 mm enter the heat exchanger from the top, while the cold air is pumped in from the bottom. Due to the fact that the design corresponds with experimental findings, it was utilized to forecast the optimal heat exchanger performance. The effectiveness of a heat exchanger was determined by comparing the exit temperatures of both

mediums to the incoming circumstances. They found that the solid-to-air mass ratio should be higher than 0.9 to maximize the heat exchange efficiency and outlet air temperature. Also, 0.5 m bed height was adequate to achieve a moderate temperature of 650°C [39].

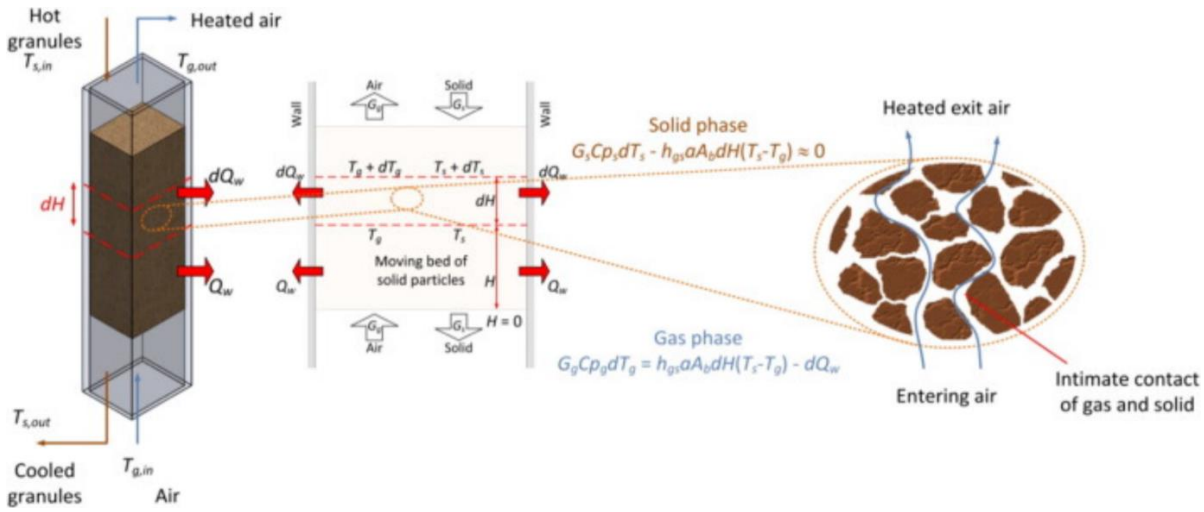

Figure 14. Illustration of heat transfer in a segment of a direct contact counter current moving bed heat exchanger as developed by Hadley [39].

3.1.3 Cyclone Heat Exchanger

In the chemical process sector, cyclones have been utilized for several decades as a device for separating gas-solid particle mixtures. Their employment as heat transmission equipment is, however, relatively recent as they can be used to heat solid particles by hot gases whenever direct contact is permitted. They show potential as a gas-solids heat exchanger in fertilizer, polymer powder, pharmaceutical, and food sectors. Jain [40] investigated a cyclone heat exchanger with a 100mm inner diameter for transferring heat between air and solids. He fed the cold sand into a

cyclone at a rate between 0.5 and 7.5 g/s in the same direction as the air with a velocity between 9 and 22 m/s. He examined the thermal effects of air inlet velocity, sand flow rate, and particle size on heat transfer rate, particle exit temperature, and heat transfer coefficient. Increasing sand flow rate and air inlet velocity enhanced the heat transfer rate, whereas increasing particle size decreased it. However, the effect of input velocity on the air-sand heat transfer coefficient was negligible. To estimate the heat transfer coefficient in such configurations, the authors devised a validated correlation within an error range of +10% to -15% for their data and +25% to -15% for other research data [40].

Shimizu and his team [41] developed an axial flow cyclone in order to conduct a computational and experimental investigation of an air-solid direct-contact heat exchanger. As shown in the illustration below, a quasi-counterflow of air at 35°C was introduced from the bottom. Simultaneously, hot glass bead particles with diameters ranging from 20 to 80 m and temperatures between 210 and 220°C were delivered from the top. The heat exchange performance was substantially improved by adding a small particle diffuser underneath the particle-feeding nozzle. Particle recovery efficiency, as measured by the weight proportion of captured particles to those released, increased as particle size increased. Due to the counter-flow, the outlet gas temperature was greater than the particle output temperature. This and similar other designs seem more suitable as coolers in chemical processing plants but not suitable as a particle to working fluid exchangers in power plants.

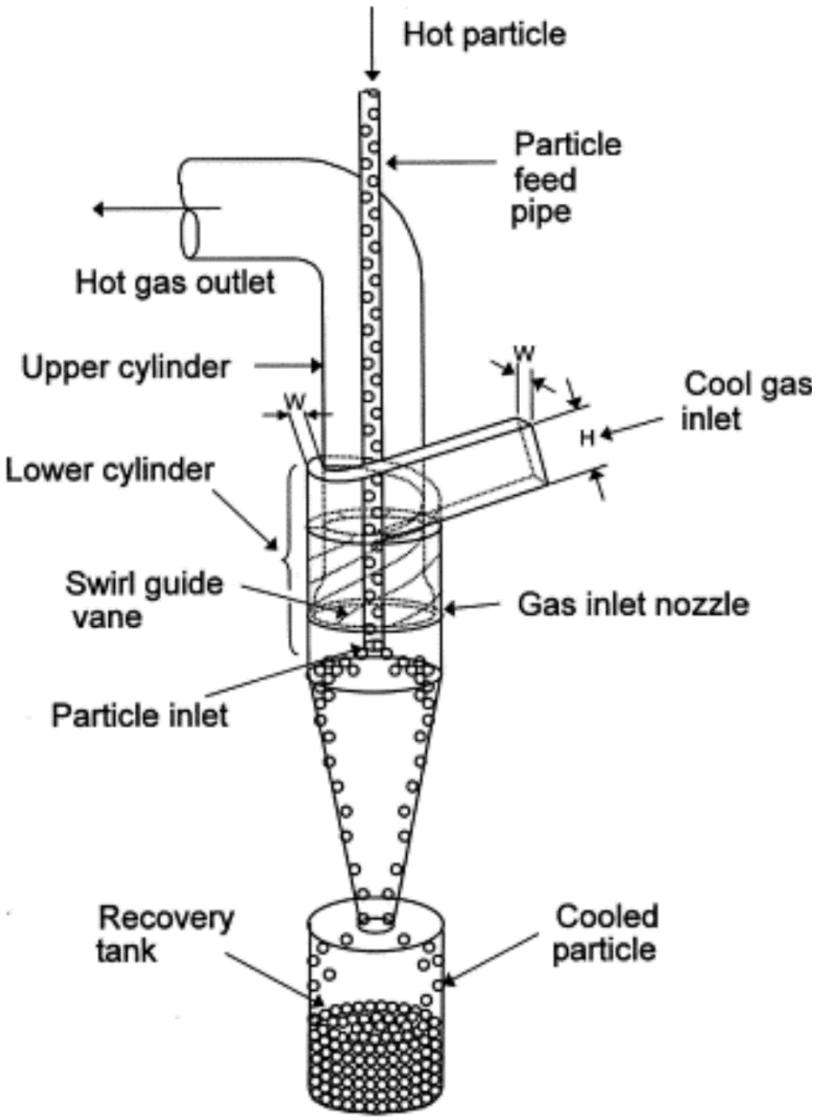

Figure 15. Illustration of cyclone heat exchanger as proposed by Shimizu and his team [41].

3.1.4 Falling Particle Heat Exchanger

Particles fall from the top of this direct-contact heat exchanger while air is pumped from the bottom. This arrangement is straightforward, has numerous benefits, and has been studied for decades. Sagoo [42] conducted one of the early research projects on particle-to-fluid direct contact heat exchangers, examining heat transfer between air and steel and alumina particles in falling

cloud heat exchangers. The device in his study consisted of a vertical tube into which solid particles were deposited. Simultaneously, hot air was supplied at the base to demonstrate that solid particles may recover heat from rising hot air. The figure below shows the apparatus of this study.

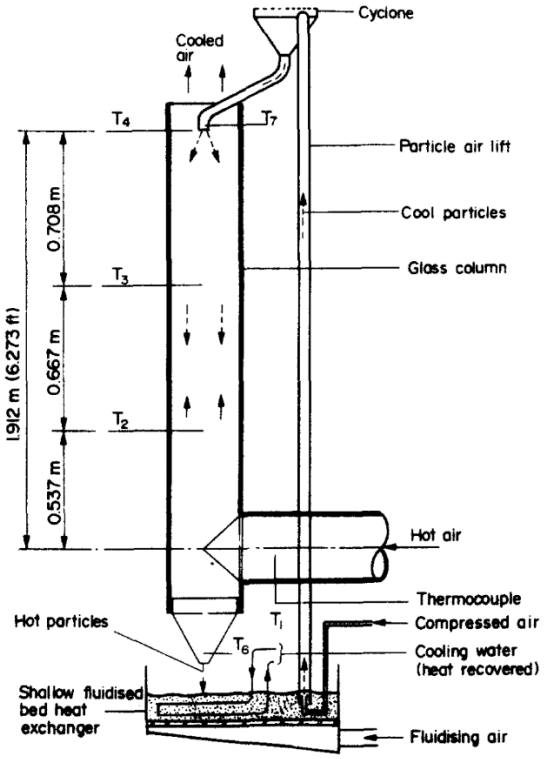

Figure 16. The falling cloud heat exchanger as proposed by Sagoo [42].

According to Sagoo [42], there are two flow zones: the high-velocity and current eddy zones. In the high-velocity region, the thoroughly turbulent flow is maintained. The eddy zone is the region around the air entrance where eddy currents form. As the velocity or temperature of the feeding gas increased, the eddy zone grew, resulting in a reduction in the effective heat exchange length. According to reports, the heat transmission coefficient reduced as the eddy region grew

larger. Additionally, it was discovered that the heat-transfer coefficient for steel particles was larger than that of alumina.

Frain and his team [43] conducted an experimental study to determine and comprehend the performance of a falling particle direct-contact heat exchanger. Particles of alumina and silica were carried to the top of the heat exchanger to fall against the ascending air. To prevent particle carryover, the air current flows at a velocity lower than the particles' terminal velocity. The heat exchanger consisted of an 8.9-meter-tall, 0.356-0.356-meter-diameter vertical galvanized steel tube. It was positioned between two cylinder-shaped hoppers, a feeder, and a de-feeder or discharge tank. They employed two distinct feeding configurations, the bare tube, and the basket distributor, to examine the effect of particle distribution on the performance of the falling-bed heat exchanger. It has been demonstrated that the improved mixing caused by the basket distributor significantly increased the heat exchanger's effectiveness. When the basket distributor was utilized, the evaluated mixing model aligned more with the experimental outcomes.

In recent research, Alaqel and his team [33] conducted an experimental and theoretical study for a falling particle-to-fluid direct contact heat exchanger used in a particle-based central tower system. The primary component of their design is a 2-meter-tall heat exchanger chamber with a variable-area duct with a circular cross-section that varies in diameter from 0.2 meters to 0.4 meters to prevent particle carryover. Another critical component is the particle handling unit, including the feeder, de-feeder, particle distribution module, particle valves, and particle lift. The figure below illustrates this heat exchanger system.

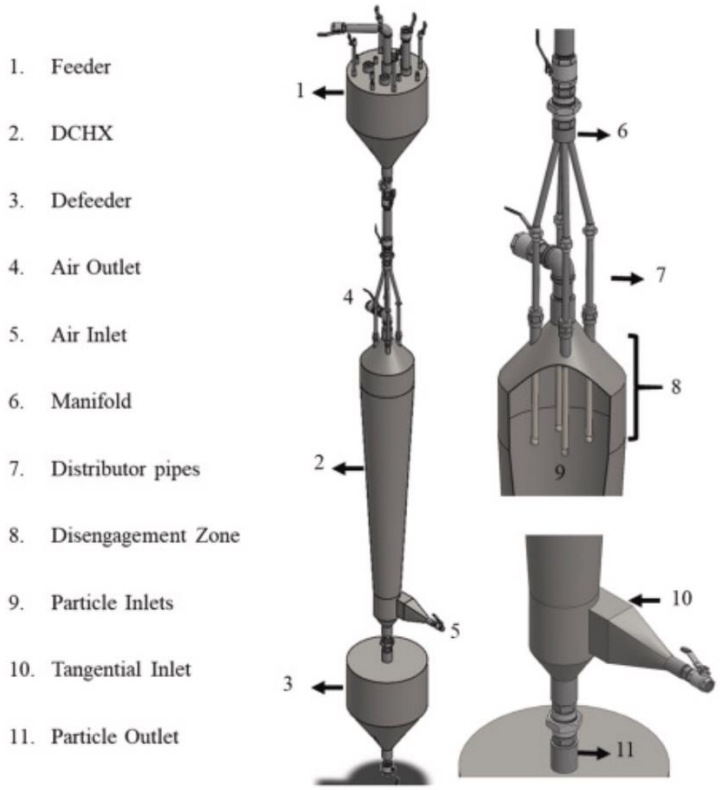

Figure 17. Falling particles direct-contact heat exchanger system as proposed by Alaqel [33].

They analyzed the system using two models and compared them with the experiment data. The mixing model considers particles as isolated when falling downward in unbounded-atmospheric air. This model was more accurate in predicting the particle outlet temperatures, and the heat rate was within ±5% of the experimental results [33]. The simple-equilibrium model indicates that thermal equilibrium was reached by air and particles in every segment along the exchanger. This model prediction is greatly enhanced by constraining the air outlet temperature's value to be less than 90% of the particle inlet temperature. The three designs discussed above are interesting; however, it was not considered feasible at this time to compare the current model with these since the model in this thesis assumes a simpler design. Comparison with experimental results and detailed CFD studies is deferred to future work.

3.2 Proposed Design

This project will investigate a free-falling particle-to-fluid direct contact counterflow heat exchanger for a variety of reasons. In general, direct-contact heat exchangers are superior to their indirect counterparts in terms of efficiency. Free-falling direct contact heat exchangers are cost-effective to construct and straightforward to maintain. This design employs counterflow to increase the air output temperature, reduce pressure loss, and make the separation of particles from the air more accessible.

This study will concentrate only on the heat exchanger chamber, where one-size particles and air come into direct contact to exchange heat. The thermal and dynamic performance of the heat exchanger is studied, including the heat transfer between the particles and air, heat exchanger's length and volume, operating pressure, particle's size, and other parameters.

In this heat exchanger design, monodisperse aluminum-based particles are used as ECM. These particles will fall freely from the top of the heat exchanger to the bottom, entering the heat exchanger chamber at an initial velocity of 1.0 m/s. While at the same time, pressured air will enter the chamber from the bottom and exit at the top of the heat exchanger. The particles will encounter the air within the heat exchanger and come to a direct contact resulting a higher heat transfer between them.

3.3 Main Forces Acting on the Falling Particle

The flow characteristics of both mediums have a substantial effect on the heat transmission between freely falling particles and ascending air. Because of the lack of resistance, when a particle is released from rest in a vacuum chamber, it will experience a steady falling acceleration. Gravity is the only cause of motion in this case. Since gravity is constant, the particle acceleration will be constant, too. However, many engineering applications involve fluid-moving objects in which extra forces affect both particle velocity and trajectory while falling.

As the gravitational force is the main force acting on a particle falling through a fluid at rest, the particle will initially undergo a rapid acceleration. However, the presence of air tends to reduce this acceleration due to the buoyancy force and drag force induced by air resistance. The buoyancy force is formed when the displaced air begins to ascend as particles fall through the air. Although the buoyancy force reduces particle acceleration, particle velocity continues to grow, and momentum is transferred to the surrounding fluid. As a result, the velocity gradient between the particle and the fluid in contact causes the particle's surface to experience frictional drag. Another force of resistance known as form drag is created by the asymmetrical pressure distribution on the particle surface. The pressure at the particle's leading edge is higher than the pressure at the particle's rear. This leads to boundary layer separation, and a wake forms in the downstream region. The overall drag force is equal to the sum of these two forces, the friction drag, and form drag. The figure below illustrates the main forces acting on the particle.

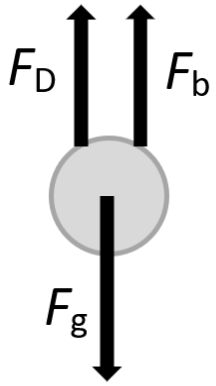

Figure 18. Free body diagram of falling particle

The total force on particle can be found in this equation:

$$\sum F_P = F_g - F_D - F_b \tag{1}$$

where the particle gravity force is:

$$F_g = m_p\, g = \rho_p V_p\, g \tag{2}$$

the buoyancy force is:

$$F_b = \rho_{air} V_p\, g \tag{3}$$

However, the buoyancy force is relatively weak compared to particle weight or drag force. Therefore, it will be negligible. Buckingham π theorem is used to find the frag force as

$$F_{\mathrm{D}} = 0.5 C_{\mathrm{D}} \rho_{\mathrm{air}} A_{\mathrm{CS}} V_{\mathrm{rel}}^2 \tag{4}$$

A_{CS} is the particle projected area normal to the direction of the movement, and V_{rel} is the relative velocity of air with respect to particle.

When the air resistance equals the gravitational force, the particle's terminal velocity is reached. The particle reaches terminal velocity when the net force acting on it is zero. Consequently, it does not accelerate or decelerate where the particle's velocity remains constant and can be found as:

$$V_{\mathrm{ter}} = \left(\frac{\rho_{\mathrm{p}} V_{\mathrm{p}} g - \rho_{\mathrm{air}} V_{\mathrm{p}} g}{0.5 C_{\mathrm{D}} \rho_{\mathrm{air}} A_{\mathrm{CS}}} \right)^{0.5} = \left(\frac{\left(\rho_{\mathrm{p}} - \rho_{\mathrm{air}} \right) V_{\mathrm{p}} g}{0.5 C_{\mathrm{D}} \rho_{\mathrm{air}} A_{\mathrm{CS}}} \right)^{0.5} \tag{5}$$

The drag coefficient C_{D} is the most difficult component in these equations to measure because of its dependence on numerous characteristics. The Reynold number, particle shape, orientation, temperature, and the action of neighboring particles all contribute to the drag coefficient and impact its value. However, reliable models are available for spherical particles.

3.4 Drag On Spherical Particles

A wind tunnel can be used to empirically determine the coefficient of drag. Using the wind tunnel, it is feasible to accurately describe physical properties like inertia, viscosity, and compressibility. Particle Reynolds number found using Equation (6) significantly influences the drag coefficient for a smooth sphere [44].

$$\mathrm{Re} = \frac{\rho_{\mathrm{air}} D_{\mathrm{p}} V_{\mathrm{rel}}}{\mu_{\mathrm{air}}} \tag{6}$$

The fluid flow around spherical particles is highly reliant on the Reynolds number of the particles. The diagram below depicts three distinct regimes based on Reynold's number: Stokes, intermediate, and Newton's [44]. When Reynold's number is considerably less than 1.0, this region is known as the Stokes regime. In this regime, the influence of flow inertia is small in comparison to viscous; hence, the effect of boundary layer separation is insignificant. As Reynold's number increases, the flow stays attached to the sphere without leaving a wake behind the particle until Reynold's number reaches 20, at which point the flow begins to separate. At Reynold's number between 20 and 130, some circular wakes begin to form in the intermediate zone; nonetheless, they remain connected to the particle. Vortex shedding happens as Reynold's number increases from 130 to 1000, and the wakes trailing the flow become less stable and detach from the spherical particle. In Newton's regimes, where Reynold's number is between 1000 and 3×10^5, the figure below illustrates that the boundary layer remains laminar in front of a spherical particle while the wakes behind it get increasingly turbulent. The region with Reynold's number greater than 3×10^5, known as the crucial Reynold's number, is more chaotic, and the boundary layer and downstream wakes become turbulent [45].

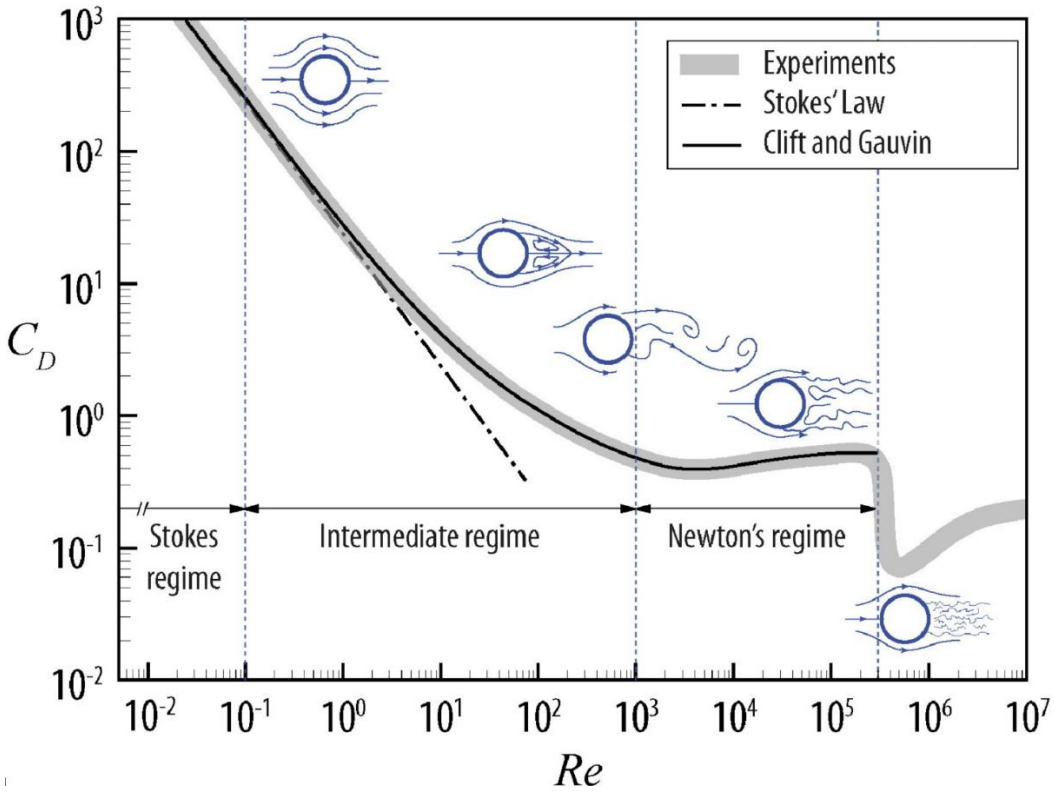

Figure 19. Dependency of C_D on Re for sphere. Streamlines around sphere at various Re are also shown in the plot [45].

In the literature, there is extensive research and various empirical or semi-empirical correlations for estimating the drag coefficient. The figure above demonstrates, for instance, that the correlation provided by Clift and Gauvin [46] may predict the C_D over a broad range of Reynold's number. Nonetheless, the table below contains some correlations that could be applied to these three regions.

Table 2. Reynolds number ranges for single particle drag coefficient correlations [47].

Region	Reynold's number range	Correlation
Stokes	$\mathrm{Re_p} < 0.3$	$C_\mathrm{D} = \frac{24}{\mathrm{Re_p}}$
Intermediate	$0.3 < \mathrm{Re_p} < 500$	$C_\mathrm{D} = \frac{24}{\mathrm{Re_p}}\left(1 + 0.15\,\mathrm{Re_p}^{0.687}\right)$
Newton's law	$500 < \mathrm{Re_p} < 2\times10^5$	$C_\mathrm{D} \sim 0.44$

3.5 Heat Transfer Between Fluid and Particle

The flow conditions surrounding a particle have a significant effect on convection heat transfer. The rate of convection heat transfer between a single particle and a fluid is determined by the following formula:

$$\dot{Q} = h\,A_{\mathrm{p,s}}\left(T_\mathrm{p} - T_\mathrm{air}\right) \tag{7}$$

Where h is the heat transfer coefficient, $A_{\mathrm{p,s}}$ is the particle surface area, T_p is the particle surface temperature, and T_air is the air temperature.

The Nusselt number (Nu) of falling spheres for different situations has been established by extensive research. Whitaker [48] developed correlations to estimate h for a variety of configurations, including flow around a cylinder, a sphere, and a packed bed. The h for the sphere can be found from Whitaker formula as following:

$$Nu = \frac{h D_p}{k} = 2 + \left(\mathrm{Re}^{0.5} + 0.06\,\mathrm{Re}^{\frac{2}{3}} \right) \mathrm{Pr}^{0.4} \left(\frac{\mu}{\mu_s} \right)^{0.25} \tag{8}$$

Where D_p is particle diameter, k is the gas thermal conductivity, Pr is the fluid Prandtl number and μ is the fluid dynamic viscosity. The fluid properties are evaluated at T_{air} except μ_s which is evaluated at the particle surface temperature. This correlation holds true for the ranges $0.71 \leq \mathrm{Pr} \leq 380$, $3.5 \leq \mathrm{Re} \leq 7.6\times 10^4$, and $1.0 \leq (\mu/\mu_s) \leq 3.2$, and was in good accordance with the experimental data throughout a broad range of Re. In this thesis, EES model was used to find *Nu* and C_D based on reliable data.

Ranz and Marshall [49] provided a more direct correlation to find Nusselt number based on experimental evidence on freely falling liquid droplets.

$$Nu = \frac{h D_p}{k} = 2 + 0.6\,\mathrm{Re}^{0.5}\,\mathrm{Pr}^{\frac{1}{3}} \tag{9}$$

This association holds true for $\mathrm{Re} \leq 200$, and the fluid characteristics are evaluated at a film temperature of $T_f = \frac{T_p + T_{air}}{2}$.

A computational study was conducted recently by Ellendt [50] to examine the effects of non-isothermal conditions on the drag and heat transfer between a heated stationary sphere and a gas flow. The hot particle was at a temperature of 1500 K, while the gas was at ambient temperature. They used COMSOL Multiphysics 5.2 to solve this system with two-dimensional, steady, laminar, and axially symmetric flow around the sphere. They discovered that the projected values of Nu are a great match with the values of Equations (8) and (9), indicating that these correlations can also be applied when there is a high-temperature difference between the particle and gas.

3.6 Particle Properties

To assure the efficacy and safety of particles functioning as an ECM and thermal energy storage, it is essential to study the particles' thermophysical properties, size, cost, and hazardous potential [51]. Particles should have advantageous thermophysical qualities, such as a high melting point so that they can operate at elevated temperatures without failure. In order to collect as much energy as possible from solar irradiation, particles should have a high energy density. Thermal stability is yet another essential property particles must possess. The durability and reliability of solid particles are other vital features that particles must have to work in CSP systems. Sintering and attrition are of significant concern as they are detrimental to the effectiveness of particles and should be avoided. Sintering and attrition change the form and size of the particles, impacting their thermostability and diminishing their lifetime. During particle sintering, two or more particles are fused to produce a bigger cluster, while attrition is the process of decreasing a particle's mass.

The temperature of a receiver is substantially impacted by particle size. Under the same operating conditions, a smaller particle size leads to a greater receiver temperature. However, producing small particles could be challenging, and a particle size that is too small may cause particles to escape through any gaps [52].

The particles must be ecologically friendly and provide minimal safety risks and must be reasonably priced. The table below summarizes some physical characteristics of alternative solid particles, including Silica Sand, Quartz, Bauxite, Silicon carbide, Alumina, and Olivine [53]. In this thesis, aluminum-based particles of one-size will be used as ECM. Appendix C shows some properties of Accucast ID50.

Table 3. Thermo-physical properties of some solid particles [53].

Material	Melting Point (°C)	Energy Density (kJ/m3)	Density (kg/m3)	Thermal conductivity (W/m.K)
Silica Sand	1320	2490	2550	1.2
Quartz	1610	2480	2600	0.4
Bauxite	2000	4095	3600	-
Silicon carbide	2210	3380	3200	100
Alumina	2054	4200	3970	23
Olivine	1870	4290	3300	0.56

Particle density may be obtained by dividing the mass of the particle by its hydrodynamic volume. As illustrated in the figure below, particles partially have some pores, so hydrodynamic volume is important.

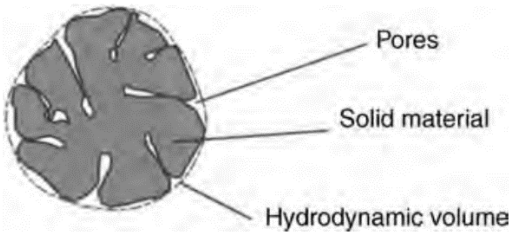

Figure 20. Schematic of hydrodynamic volume of a particle [47].

The particle hydrodynamic volume, which is the volume of the particle when it encounters a fluid, is utilized to calculate the particle's bulk density using the following equation.

$$\rho_{p,bulk} = \frac{m_p}{V_{p,hy}} \tag{10}$$

To determine the actual particle density, divide the bulk density by the fraction of particle solid volume as following:

$$\rho_p = \frac{\rho_{p,bulk}}{f_{SV}} \tag{11}$$

The fraction of particle solid volume f_{SV} is the percentage of the solid material volume making up the particle and can be found from the following equation.

$$f_{SV} = 1 - f_{VV} \tag{12}$$

Where f_{VV} is the fraction of particle void volume, the volume of particle occupied by pores.

In this project, aluminum-based particles will be used as energy carrier medium and thermal energy storage.

3.7 Particles Carryover

Particles exiting the heat exchanger with air destined for the turbine could have detrimental effects on the turbine. To prevent particles from causing harm to the turbine, it is necessary to minimize particle carryover [54]. As the rising air temperature increases owing to heat exchange with descending hot particles, its ascent velocity increases. To avoid particle carryover, it is vital to prevent the air velocity from reaching the particles' terminal velocity. Consequently, determining the terminal velocity at which the viscous drag on the particle equals its weight is critical for designing the DCHX and minimizing particle carryover.

Alaqel and his team [32] designed a particle–air disengagement zone at the top of the DCHX to prevent particle carryover. At the top of the heat exchanger chamber, where the air is intended to exit, the abrupt decrease in the flow area causes the air to accelerate. The area of the exit pipe, where air leaves, is considerably less than the top end of the DCHX. As the hot air accelerates, it may approach the terminal velocity of the particles, causing them to rise instead of fall. To prevent any sudden change in airflow conditions near the particle feed area, the heat exchanger is extended vertically above the particle distributor outputs. The diagram below illustrates the disengagement zone that assures stable flow conditions, enables smooth particle input, and minimizes the risk of particle carryover.

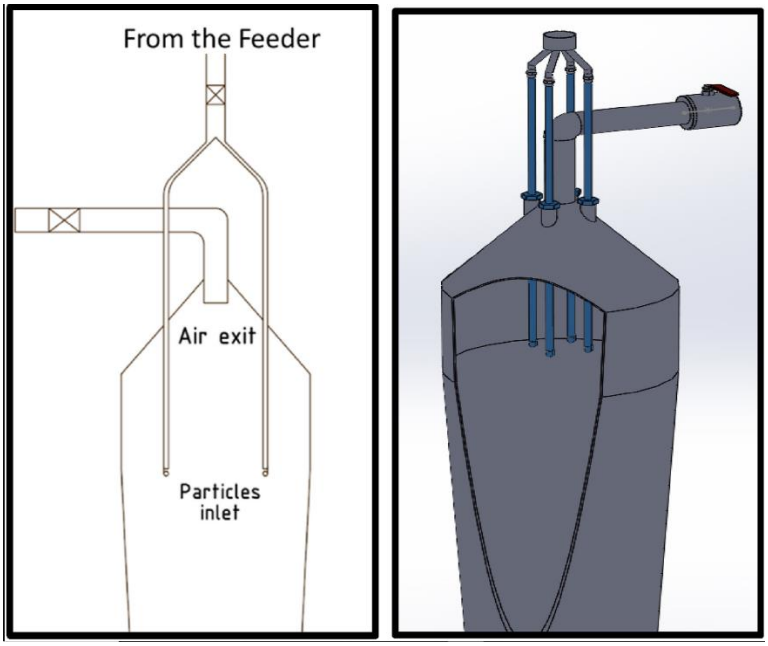

Figure 21. Schematic of disengagement zone showing the location of the air exit port relative to the particulate inlet ports as proposed by Alaqel [32].

Despite the fact that the particle carryover poses a significant threat to the turbine, investigating it further is beyond the scope of this research.

3.8 Particle Feeders, Distributors and De-Feeders

The particle handling unit as proposed by Alaqel [24] consist of feeders for introducing particles into the DCHX, particle distributors for obtaining uniform particle distribution over the heat exchanger, and de-feeders for removing particles from the DCHX. Feeders and de-feeders are typically cylindrical-shaped pressure tanks with some valves. As illustrated in the figure below, the valves on the feeders and de-feeders regulate the operation of loading and emptying the tank with solid particles and air.

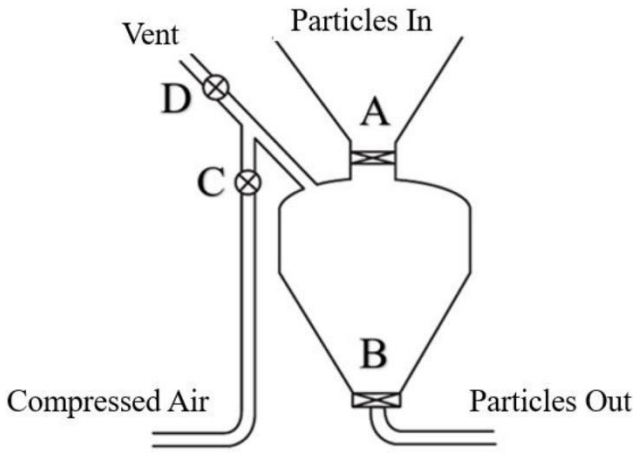

Figure 22. Typical cyclic operation of the pressure tank [55].

Numerous feeder methods have been designed to transport a sufficient quantity of hot solid particles into the pressurized DCHX. Rotary valves, screw valves, and blow tanks have all served as particle feeders; blow tanks are the most reliable system. Due to the moving components of the other feeder systems, metal undergoes abrasion and particle attrition [24].

As hot particles are in the feeders, they should be uniformly distributed over the heat exchanger, as the heat exchanger performance depends on the uniform distribution of falling particles. Thus, the particle distributor must uniformly deliver the hot particles leaving the feeders to the upper end of the heat exchanger. Frain conducted research to investigate the effect that adding a particle distributor to the DCHX's particle inlet pipe would have on the device's overall performance [56]. According to what they found; the effectiveness of heat exchangers can be significantly enhanced compared to having a bare tube input. However, a single distributor will not be able to effectively disperse the particles across the DCHX's area when the particle mass flow rate is larger [24].

Alaqel utilized multiple particle inlets to divide the particle mainstream into numerous distinct streams [32]. Each stream can be routed to a unique zone within the DCHX. As illustrated in the figure below, they developed the particle distributor to consist of the manifold assembly and a group of distributor pipes. The assembly, which is connected to the feeder outlet by using a two-inch receiving cup, splits the particle stream into multiple streams. The distributor pipes transport the particles to the top of the DCHX chamber.

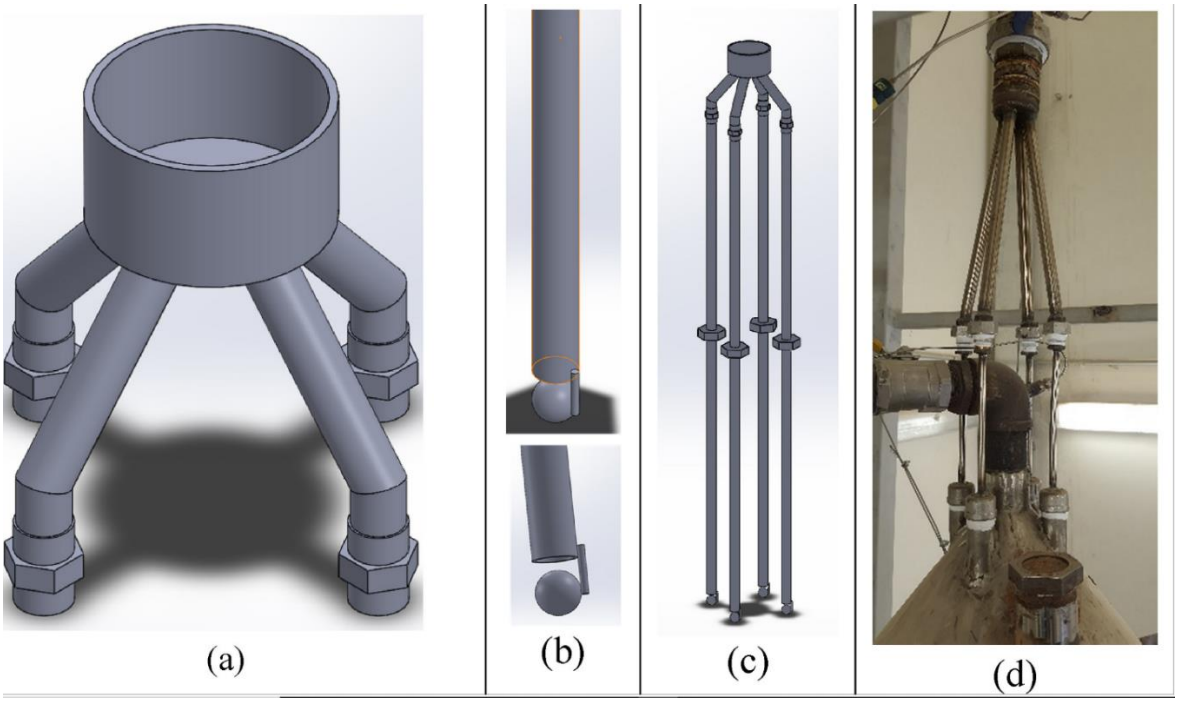

Figure 23. Particle distributor module (a) the manifold assembly, (b) distributor pipe, and (c) module assembly, (d) snapshot of the assembly as developed by Alaqel [32].

Despite their significance in this heat exchanger system, the feeders, particle distribution, and de-feeders are beyond the scope of this thesis. In fact, the team in King Saud University has been studying these systems.

CHAPTER 4. DIRECT CONTACT HEAT EXCHANGER ALLOYS

This chapter aims to study several materials that could be used in manufacturing the heat exchanger's body. This DCHX is a high-temperature and moderate pressure application as the temperature of the working materials ranges from 660°C to 1100°C, and the operating pressure is four and eight bars. Consequently, the operating characteristics of this heat exchanger must be taken into account when researching these materials. This investigation should find the high-temperature alloys to be of tremendous interest. Due to their extraordinary qualities, these substances can resist elevated temperatures and function in harsh conditions. In the subsequent sections of this chapter, many metals' suitability for use in this high-temperature application is evaluated.

Potential materials and alloys' thermal and mechanical properties will be evaluated to find the optimal material for the heat exchanger's body. It is essential to investigate these material qualities to prevent future failures and acquire the most effective results from the DCHX. The relevant materials must possess specified physical and thermal features, such as exceptional corrosion resistance, a low thermal expansion coefficient, a wide range of melting temperatures, and low thermal conductivity. In addition, the material must possess outstanding mechanical qualities at high temperatures, such as good creep properties, including great creep ductility for strains and high creep rupture, and acceptable strengths, such as tensile, yield, and allowed stresses.

4.1 Potential Materials to Build the DCHX Body

Numerous commercially available high-temperature alloys could be investigated to determine their suitability for this DCHX design. As some of the best high-temperature alloys for use in high-temperature applications, a few stainless-steel grades and nickel-based metals are under consideration for investigation in the present study. This chapter examines these materials' physical, thermal, and mechanical properties to make an informed selection regarding the optimal material for the DCHX body. During this procedure, ASME Boiler and Pressure Vessel Code (BPVC) and industry data were used to inspect the material's qualities. The sections that follow detail the candidates considered in this study, and they are as follows:

- Stainless-steel 316
- Stainless-steel 309
- Inconel 625
- Inconel 740
- Haynes 282

4.1.1 Stainless Steel 316

Stainless steel 316 is an enhanced version of stainless steel 304, which is widely employed in the automotive, manufacturing, nuclear, and petrochemical industries [57]. It is also resistant to oxidation, making it suitable for use in a variety of industries, including naval applications, refining gear, and pharmaceutical equipment. This alloy is highly desirable for usage in jet engines, exhaust manifolds, and heat exchangers because of the high molybdenum concentration of this stainless-steel grade in high-temperature applications. Table 4 provides the chemical composition of stainless steel 316 [58].

Table 4. The chemical composition of the stainless steel 316 [58].

Material	**Weight %**
Carbon C	< 0.08
Manganese Mn	< 2.00
Phosphorus P	< 0.045
Sulfur S	< 0.03
Silicon Si	< 0.75
Chromium Cr	16.00 - 18.00
Nickel Ni	10.00 – 14.00
Molybdenum Mo	2.00 – 3.00
Nitrogen N	< 0.10
Iron Fe	Balance

In almost all applications, stainless steel 316 performs better and has more corrosion resistance than alloy 304. Stainless steel 316 is perfectly adapted for use in freshwater and has excellent corrosion resistance in a seawater environment. The 316 grade is also resistant to pitting in acidic environments. It can be used to protect items from contamination in industries that require acetic fields, such as the food and pharmaceutical industries. It is also resistant to corrosion in sulfur-containing environments, such as the pulp and paper industry. The primary working substances in this DCHX are air and particulates, which are predominantly non-corrosive chemicals. Consequently, stainless steel 316 will be an appropriate material for the body of the heat exchanger without regard to corrosion. To further investigate the technical capabilities of this

alloy, the physical and mechanical properties of stainless steel 316 and the mean coefficient of thermal expansion are shown in the tables below [59].

Table 5. Physical properties of stainless steel 316 [59].

Property	**Value**
Density	7900 Kg/m^3
Specific Heat	450 J/kg-°K (0–100°C)
Modulus of Elasticity	200 GPa
Thermal Conductivity (100°C)	14.6 W/m-°K
Melting Range	1390–1440°C
Electrical Resistivity	74 μΩ-cm at 20°C

The excellent physical qualities of stainless steel 316 make this grade an ideal candidate for the design of this DCHX body. As indicated in the table, the melting temperature range is greater than the air and energy carrier medium temperatures within the heat exchanger. Therefore, alloy 316 is resistant to failure under these elevated temperature working conditions.

The mean coefficient of the thermal expansion of this grade is shown in Table 6 below [59]. As shown in the table, stainless steel 316 has an extensive range of temperatures with low thermal expansion.

Table 6. Mean coefficient of thermal expansion of stainless steel 316 [59].

Temperature range (°C)	**Value (cm/cm°C)**
20–100	16.6×10^{-6}
20–500	18.2×10^{-6}
20–1000	19.4×10^{-6}

The mechanical properties of the stainless steel 316, including the minimum tensile stress, minimum yield stress, and other properties, are shown in Table 7 [59]. The tensile stress is critical to the design of this heat exchanger, as the pressure within the heat exchanger should not exceed the allowable stress. In addition, yield stress plays a considerable influence in defining the creep qualities, which will be detailed in the following section.

Table 7. Mechanical properties of stainless steel 316 [59].

Property	**Value**
Min. tensile strength	515 MPa
Min. yield strength	205 MPa
Elongation in 50 mm	40 %
Max hardness, Rockwell B	95

The ability of the material to sustain the pressure imposed by the pressured air within the heat exchanger compartment without failing is one of the most important variables that must be considered when fabricating this heat exchanger. The allowable stress of stainless steel 316 is therefore investigated. The allowable stress is the maximum tensile, compressive, or bending stress that material may withstand without failing [60]. Calculated using Equation (13), it is a proportion of the material's ultimate stress based on a safety factor [60].

$$S = \frac{\sigma}{SF} \tag{13}$$

Data of the allowable stress at different elevated temperatures are obtained from the ASME BPVC and presented in Figure 24 [61]. Note that the recommended ASME strength data appear to be rather conservative and, therefore, reasonable to use in preliminary design studies.

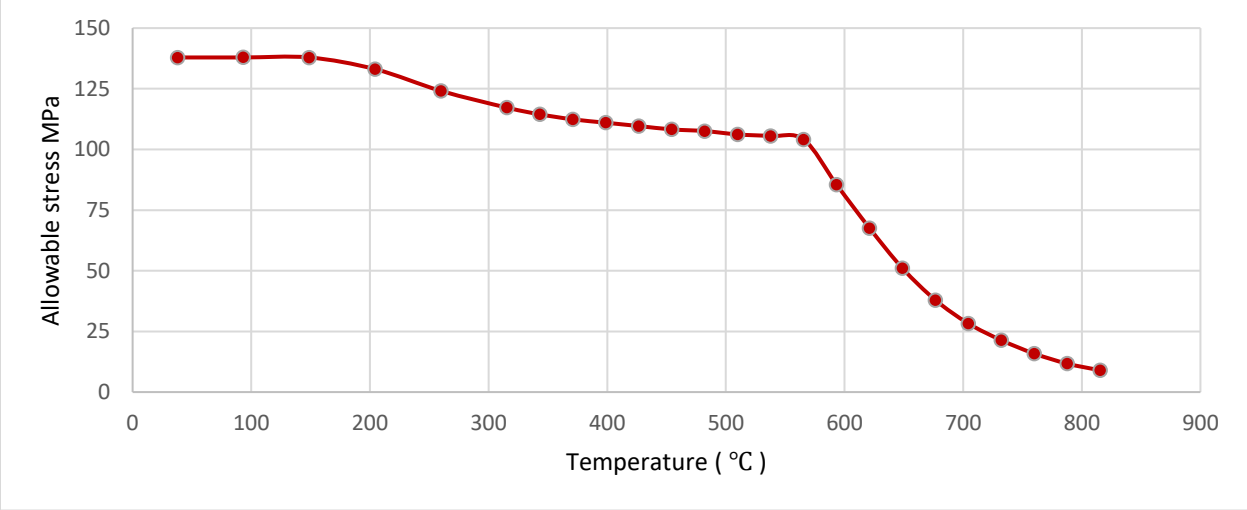

Figure 24. Stainless steel 316 allowable stress at elevated temperatures *[61]*.

The allowable stress of stainless steel 316 has been obtained from the ASME BPVC. This alloy has high allowable stress at elevated temperatures, as shown in the figure above. The allowable stress drops slightly with increasing temperatures up to a high critical temperature, where the curve falls dramatically. The allowed stress at 815°C is around 9 MPa, which is significantly greater than the operating pressure in this DCHX, which is approximately 4 and 8 bars. Consequently, stainless steel 316 can operate reliably under these circumstances.

Creep is another essential element that must be considered while selecting the appropriate material for this DCHX. At elevated temperatures, creep is the permanent plastic deformation of a material under steady tension below its yield stress. The stress responsible for material failure is known as rupture stress. The material that suffers creep rupture passes through three stages, as depicted in the diagram, and described below [62]:

Stage I:

Primary creep is the stage where elastic deformation begins, followed by plastic deformation; this stage occurs quickly with an extremely high rate of deformation. As illustrated in the graph below, the creep rate varies with strain ε or time; the creep rate, the slope dε/dt, decreases as the strain increases [62].

Stage II:

Secondary creep, also known as steady-state creep, occurs when the slope of the curve, which represents the rate of creep, is nearly linear and constant. This level's creep pace is significantly slower than the one in the previous stage, and its behavior is entirely foreseeable at this point [62].

Stage III:

Tertiary creep occurs when the rate of creep drastically increases, as depicted in the diagram below. This fast creep rate and microstructural deterioration result in material fracture and failure known as the creep rupture [62].

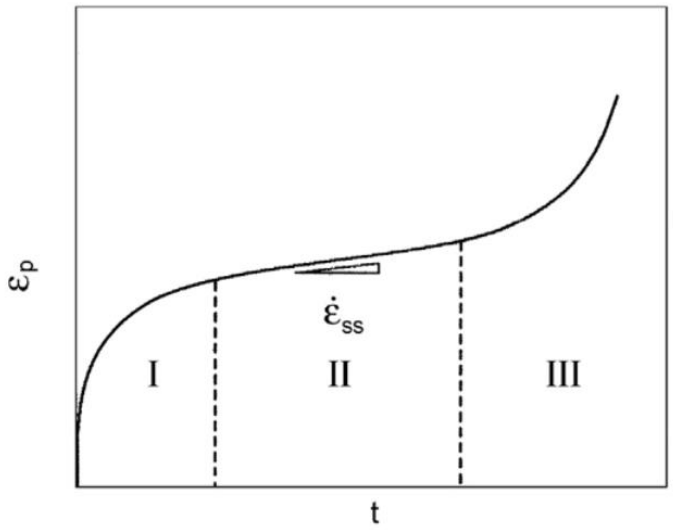

Figure 25. Creep rate over time at constant stress [62].

The creep properties of stainless steel 316 are presented in the tables below [63]. As indicated previously, the pressure within the heat exchanger is approximately four and eight bars, which is much lower than the yield stress of stainless steel 316 and all creep stresses, as shown in the tables below. Therefore, stainless steel 316 is an appropriate material for this heat exchanger construction due to its superior creep qualities.

Table 8. Creep stress to produce 1% strain [64].

Temperature (°C)	Stress (MPa) to have a 1% strain	
	10,000 hours	100,000 hours
550	225	125
600	145	80
650	95	55
700	65	35
750	40	20
800	30	15
850	20	10

Table 9. The creep rupture [64].

Temperature (°C)	Stress (MPa) to have a rupture	
	1000 hours	10,000 hours
550	320	270
600	220	170
650	160	110
700	110	70
750	75	45
800	55	30
850	35	20

Stainless steel 316 shows the ability to be used in the construction of this heat exchanger's body because of all the incredible characteristics.

4.1.2 Inconel 625

Inconel 625 is a nickel-based superalloy that possesses exceptional characteristics at both high and low temperatures. This superalloy is utilized for a variety of purposes due to its great corrosion and oxidation resistance, excellent fabricability, high strength, and good creep. Due to its superior mechanical, thermal, and physical properties, this alloy is utilized in a variety of fields. Inconel 625 is used not only in the aerospace, maritime, and chemical industries but also in the core of pressurized water reactors, gas turbines, and heat exchanger tubes. In this chapter, this alloy's potential for use in the design of this heat exchanger will be evaluated [65].

Due to its unique chemical composition, Inconel 625 has been able to achieve its excellent properties. The chemical composition of this alloy is mainly consists of nickel with a weight percentage of 58, chromium with weight percentage of 20 – 23, molybdenum with a weight percentage of 8 – 10, and other components with lower percentages as it can be seen in Table 10 below [66, 67].

Table 10. The chemical composition of the Inconel 625 [66, 67].

Material	**Weight %**
Carbon C	0.1
Manganese Mn	0.5
Phosphorus P	0.015
Sulfur S	0.015
Silicon Si	0.5
Chromium Cr	20.00 - 23.00
Nickel Ni	58
Molybdenum Mo	8 - 10
Niobium Nb (plus Tantalum Ta)	3.15 – 4.15
Iron Fe	5
Aluminum Al	0.4
Titanium Ti	0.4
Cobalt Co	1.0

The components in Inconel 625's composition result in high corrosion resistance, making Inconel 625 ideal for mild and severe corrosive environments. This alloy can be utilized easily in freshwater, saltwater, and alkaline environments. However, the nickel and chromium combination is resistant to oxidizing chemicals, and the nickel and molybdenum combination is resistant to nonoxidizing mediums, allowing Inconel 625 to function in abrasive conditions. As is the case with stainless steel 316, the high molybdenum content of this superalloy makes it resistant to

pitting and crevice corrosion. These characteristics of Inconel 625 make it appealing to numerous industries, including the heat exchangers sector. Consequently, Inconel 625 is a prominent material for producing the body of this heat exchanger without corrosion concerns [66].

To proceed in the process of analyzing the potentiality of Inconel 625 in manufacturing the heat exchanger's body, the physical and mechanical properties and the mean coefficient of thermal expansion are studied. Those essential characteristics are presented in the tables below to investigate this alloy's capability to be used in this DCHX [66, 68].

Table 11. Physical properties of Inconel 625 [66, 68].

Property	**Value**
Density	8440 Kg/m^3
Specific Heat	446 J/kg-°C (100°C)
Thermal Conductivity (100°C)	11.4 W/m-°C
Modulus of Elasticity	201 GPa
Melting Range	1290 – 1350°C
Electrical Resistivity	1.26 μΩ-m at 23°C

The physical qualities of Inconel 625 are comparable to those of the preceding alloys. These characteristics make this material an additional good alloy for use in the construction of this DCHX. This alloy's melting temperature range is higher than the air and energy carrier medium temperatures within the heat exchanger, making it a strong choice for the construction of the DCHX body.

The mean coefficient of the thermal expansion of this metal is shown in Table 12 below [66]. As shown in the table, Inconel 625 has a broad spectrum of temperatures with low thermal expansion. The values of the Inconel 625 are insignificantly different from both stainless steel 316 and 309.

Table 12. Mean coefficient of thermal expansion of Inconel 625 [66].

Temperature range (°C)	**Value (cm/cm°C)**
20 - 204	13.1×10^{-6}
20 - 538	14.4×10^{-6}
20 - 982	17.3×10^{-6}

The mechanical properties of this metal, including the minimum tensile stress, minimum yield stress, and other properties, are shown in Table 13 [68].

Table 13. Mechanical properties of Inconel 625 [68].

Property	**Value**
Min. tensile strength	910 MPa
Min. yield strength	468 MPa
Elongation in 50 mm	47 %
Max hardness, Rockwell B	94

As shown in the table above, the Inconel 625 has much higher tensile and yield strength than the stainless steel 316 and 309, which shows this metal's strength superiority. The allowable stress of this alloy is studied and obtained from ASME BPV codes and is presented in Figure 26 [61].

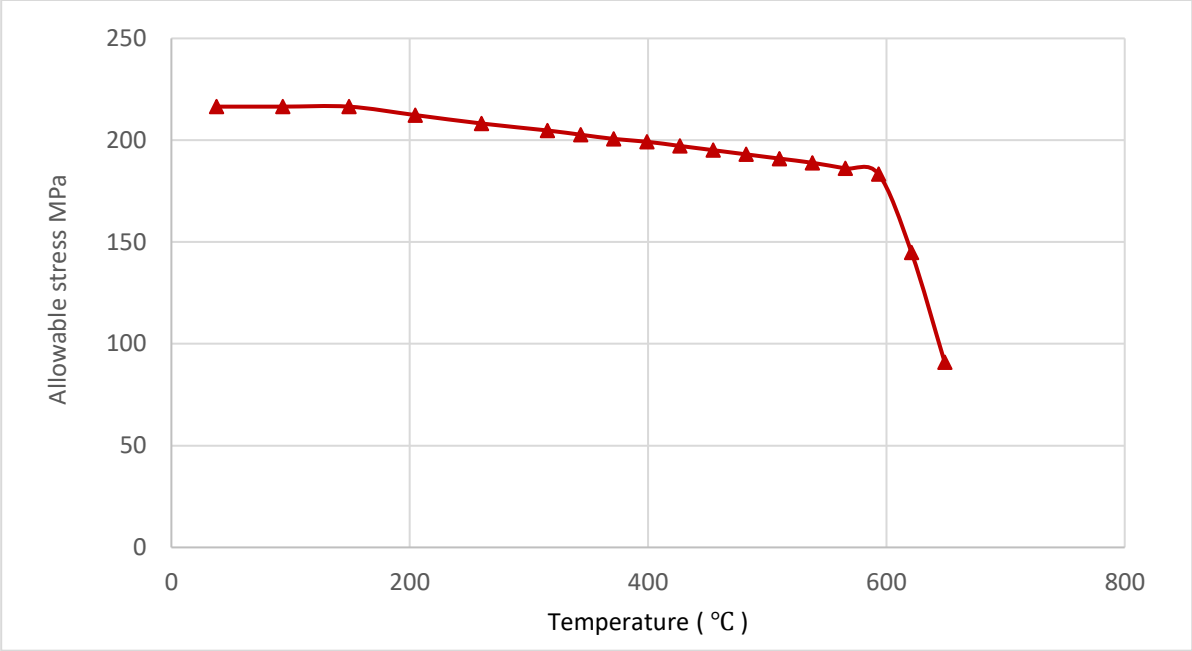

Figure 26. Allowable stress of Inconel 625 at elevated temperatures [61].

The allowable stress of Inconel 625 was obtained from the ASME BPVC. This material has higher allowable stress than stainless steels 316 and 309. At 510°C, the maximum allowable stress for grades 316 and 309 is roughly 106 and 93 MPa, whereas for Inconel 625 it is around 190 MPa. Though the stress curve exhibits the same behavior as in stainless steel 316 and 309, where allowable stress reduces somewhat as temperature increases up to a high critical temperature, where the stress curve falls dramatically. This allowable stress curve demonstrates that Inconel 625 is subject to greater strains than the operating pressure in this DCHX. Thus, Inconel 625 can withstand this pressure without breaking.

The creep rupture is studied to analyze the Inconel 625 and its capability to be used for this heat exchanger's body design. The creep and rupture are illustrated in the figures below [68]. As seen in the figures below, the heat exchanger pressure is significantly less than the yield stress of

Inconel 625 and substantially less than all creep stresses. The excellent creep qualities of this superalloy make it a suitable material for this heat exchanger construction.

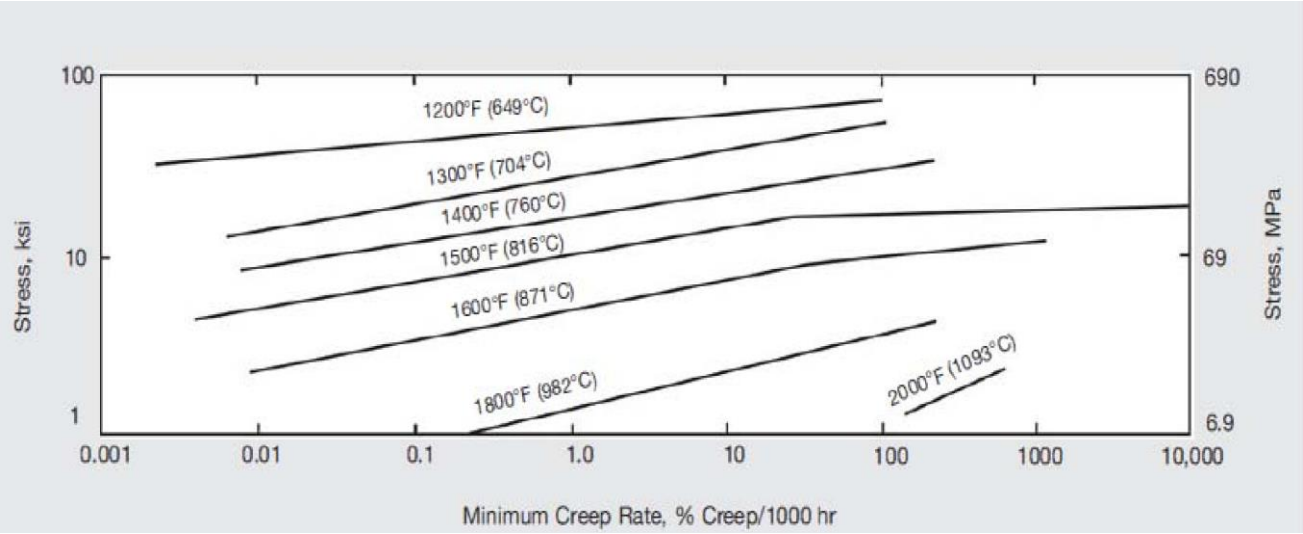

Figure 27. Creep strength of Inconel 625 [68].

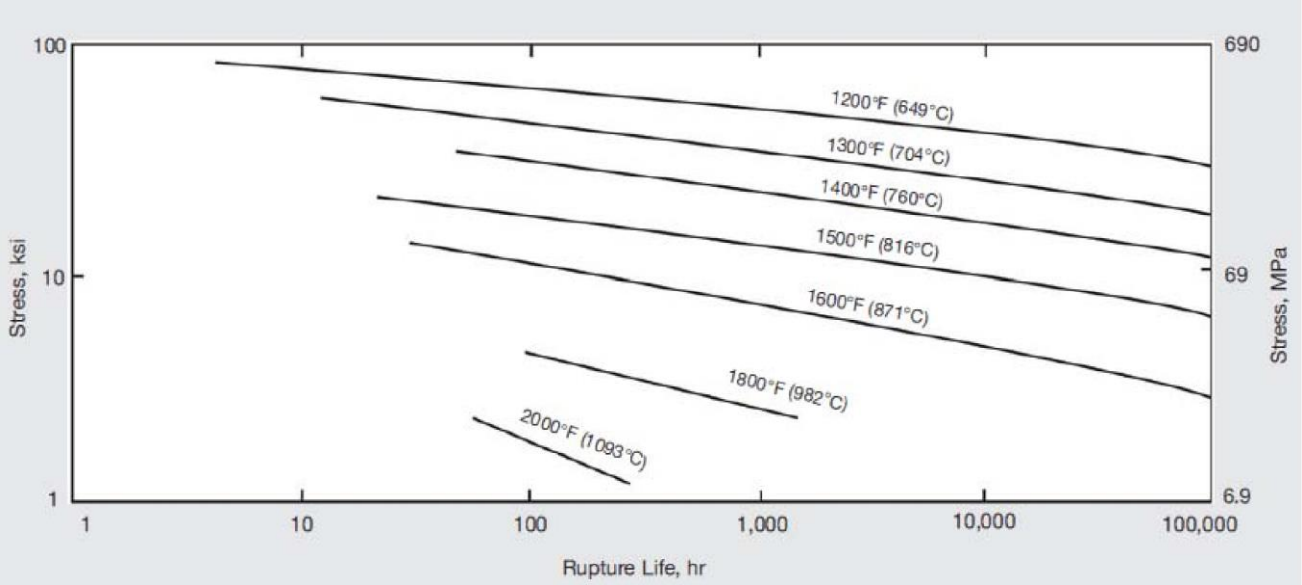

Figure 28. Rupture life of Inconel 625 [68].

In conclusion, this study shows that Inconel 625 is another suitable material that could be used to construct this heat exchanger's body. More alloys have been studied and documented in Appendix D.

4.1.3 Conclusion

All the aforementioned metals have excellent thermal, physical, and mechanical qualities, making them ideal choices for the construction of this heat exchanger. They all have a high melting point above the heat exchanger's operating temperatures. They demonstrate excellent creep characteristics and corrosion resistance. To conclude this investigation, the following figure illustrates the maximum allowable stresses of all metals at increased temperatures.

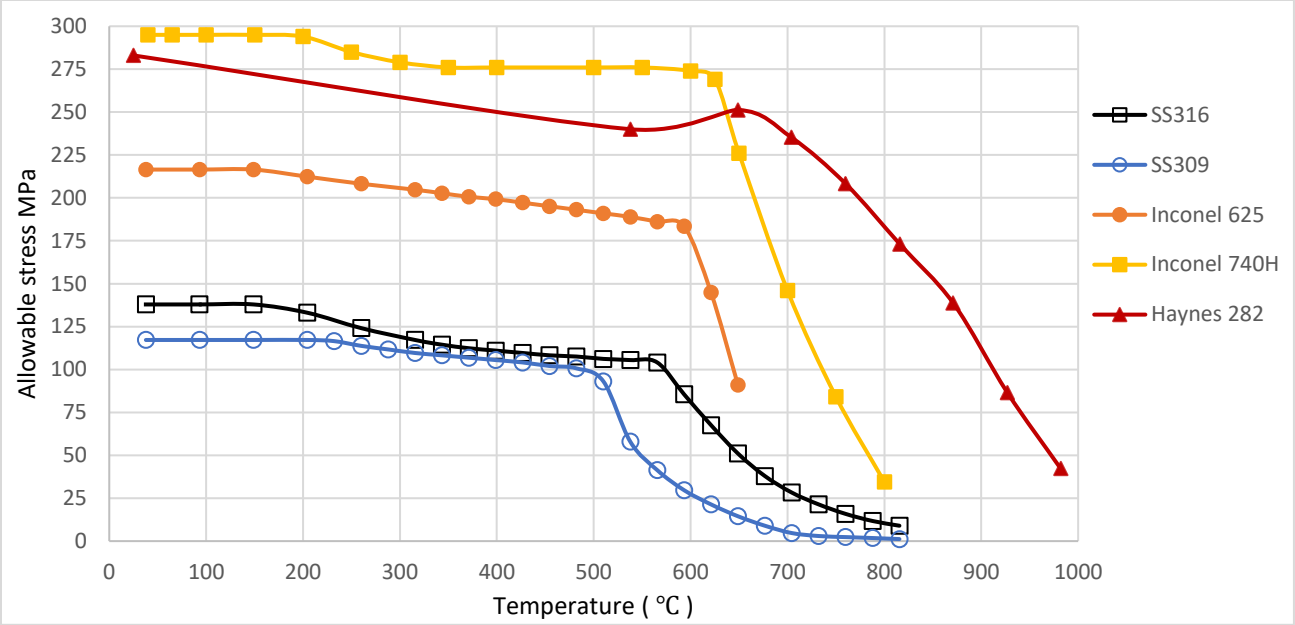

Figure 29. Allowable stresses of superalloys at elevated temperatures [61, 69]

Note that the ASME data appear to be conservative and address the allowable strength data assuming a given safety factor. To support future studies, it is recommended to report the underlying strength data instead. In addition, any new alloys and composites should also be considered. It is also recognized that many alloys suffer reduced strength above 600ºC; consequently, it is highly favorable that proposed DCHX designs allow for internal insulation to protect most of the shell from high temperatures. Internal insulation could prevent wall temperatures from exceeding 650°C. Furthermore, most components that must be exposed to high-temperature particles or fluids are only lightly stressed, allowing less expensive alloys to be still used or of a limited size compatible with the economical use of superalloys. Hence, stainless steel 316 should be suitable for shell of the heat exchanger, while superalloys may be best for a thin shield with internal and external insulations. Appendix E has a cost estimate based on Stainless-Steel 316, and a superalloy which proved to be an excellent material choice for this DCHX.

CHAPTER 5. ONE-DIMENSIONAL SIMULATION MODEL FOR DIRECT CONTACT HEAT EXCHANGER

5.1 Overview

This particle based DCHX consists of a cylinder positioned between the feeder and de-feeder tanks. This research focuses primarily on the heat exchange between the hot particles that descend and the compressed air that ascends in counter-flow direct-contact heat exchange. In the heat exchange chamber, hot particles are deposited at the top side via the feeders, while pressurized air is supplied from the lower side. The velocity of ascending air increases as a result of increasing its temperature. While particles will initially experience high deceleration once they enter the heat exchanger until they overcome the drag force and then accelerate due to gravity.

The flow characteristics of particles in free fall and air moving upwards influence the heat exchange process. Particles falling in a heat exchanger are subject to several forces, including gravity, buoyancy, and drag. Several characteristics, such as particle shape, beginning temperature, and particle flow rate, significantly impact the particles' resulting drag on the particles. Sabine [70] showed through his study that irregularly shaped particles encounter a more significant amount of drag than particles with regular shapes. This results in a more extended residence period because a greater drag causes a slower falling velocity. And Duan [71] demonstrated that particles of the same size and shape are likely to fall more slowly at higher temperatures than at ambient temperature. Consequently, irregular high-temperature particles encounter more drag. This result is essential in the DCHX design process, as particle carryover could exist if the drag exerted on the particle is larger than its weight.

The quality of the air leaving the DCHX is crucial for integrating the DCHX with the Brayton cycle, an air-breathing cycle. To protect the turbine blades from being damaged, the air should be clean of any particles. During the design phase, several elements could be considered in order to provide optimal heat exchange conditions and compatibility with an air-breathing power cycle. Alaqel and his colleagues [32] investigated many enhancements to improve the heat exchange performance, including the heat exchange chamber's design, the air inlet's layout, and a disengagement zone near the DCHX's upper air outlet. However, it is beyond the scope of this thesis to study the mechanisms of feeding the particles into the heat exchanger chamber, removing them from the chamber, supplying compressed air into the chamber, or expelling it from the chamber.

5.2 Background

Numerous assumptions were made while studying the properties of the falling curtain and analyzing the heat transfer to simplify the difficulty of the analysis. Researchers assume that the flow is steady and one-dimensional, that particles are distributed equally across the cross-sectional area of the heat exchanger, and that particle-to-particle interaction is ignored. In addition, they assume that the interaction between particles and walls is negligible, that particle size is uniformly spherical, that the radiative exchange between particles and walls is ignored, and that the mixture pressure is the pressure of the gas [33].

In a direct-contact heat exchanger containing a gas cooling segment and an air heating segment, Gat [72] studied the idea of recovering heat from a hot gas to heat an airstream by employing solid particles. The particles pass through a heated gas stream, absorbing the heat from the hot gas; thus, the gas is cooled. Then the heated particles fall through an airstream to heat the air before the cooled particles are transported to the original location where the process started, the

top of the heat exchanger. This heating and cooling cycle is then repeated. In his investigation, Gat used stainless steel and ceramic balls with diameters of 1, 1.6, and 2 mm and solid loadings of 0.8-2. It has been found that, under identical working conditions, small particles can recuperate heat more efficiently than large particles. However, smaller particles are more likely to be transported by the flowing gas and cause some particle carryover issues.

Park and his colleagues [73] developed a direct-contact heat exchange considering particulate as a heat transfer medium. They expanded the prior work by placing a greater emphasis on particle-to-particle and particle-to-gas radiative heat exchange. The radiative heat transfer equations were resolved using the finite difference method. In large-scale applications, the results demonstrated that gas radiation strongly impacts the temperatures of both media. The gas temperature in the particle heater rises as the gas absorption coefficient improves when the gas and particle mass flow rates are increased. This varies from the outcomes of the small-scale heat exchanger.

Saatdjian and Large [74] developed an analytical model to estimate the heat balance and thermal efficiency of a gas and particle heat exchanger with countercurrent flow. Effective packing porosity and the number of particles in contact with the gas are determined using the Ergun equation. Their research disregarded particle-to-particle conduction and heat losses from the column. The outcomes demonstrate that the model accurately predicts the efficiency versus gas velocity curve for various packing heights. Maximum exchanger efficiency is seen both theoretically and experimentally at identical velocity values.

Under the conditions of neglecting the radiant heat transfer, Achenbach [75] investigated the flow and temperature characteristics of packed beds. He provided correlations to estimate convective heat transfer, pressure drop, effective thermal conductivity, and wall-to-fluid heat

transfer for both still and moving gases. He revealed new experimental results on heat transmission and pressure loss that surpass the prior Reynolds number range by one order of magnitude. The research was performed on a heated particle immersed in a cooler-packed bed. Thus, point conduction, bypass, and natural convection were considered while calculating the heat transfer coefficient.

Liu [76] evaluated a crossflow moving packed bed heat exchanger in a steady state and two-dimensional model. The packing material was supposed to have a spherical form with a diameter of 2.224 mm. Using the approach of the steady-two-fluid model, a set of nonlinear differential equations was created and solved. It was presumed that the bed temperature was uniform in all directions to simplify the problem. In addition, particles were assumed to be isothermal during the study and were only permitted to travel in the horizontal plane. The numerical results agreed well with the experimental findings.

Jain and his colleagues [40] simulated the gas-solid counter-flow direct-contact heat exchanger by creating a steady-one-dimensional two-fluid model. Frain and his team's [43] experimental findings corresponded well with Jain's model predictions. The model was utilized to forecast the impact of solid loading ratio and particle size on the operation of the heat exchanger. According to their findings, larger solid loading and smaller particles improved the heat process of the recovery process. Jain [40] has utilized the same model to examine the effects of combining several gas inlets in a conveying duct during the heat recovery procedure. Except for tiny particles, the results indicated that dispersing the gas over the conveying duct increased heat recovery.

Alaqel and his colleagues used two theoretical models to analyze a particle-to-air direct contact heat exchanger in a counter-flow configuration [33]. The mixing model assumes particles falling through unbounded air to be isolated. This model predicted the particle discharge

temperatures for particles with a diameter of 0.5 mm with a higher degree of precision, and the experimental findings were within 5% of the predicted heat rate. The simple-equilibrium model demonstrates that air and particles attained thermal equilibrium in every heat exchanger section. The output temperature was overestimated by this model independent of particle size.

Since this model is one-dimensional and uses one size particle, the comparison with existing models is time-consuming. Available time has not allowed adequate comparison of this model in this thesis with the published applications; however, this comparison will be part of future work. Additionally, some published models may not be directly comparable with this model.

5.3 Analytical Model

In this particle-air counterflow direct contact heat exchanger, particles drop against pressured air that is moving upward, as shown in the schematic below. To simplify the difficulty of the model, some assumptions were made while designing this heat exchanger, such as:

- Steady-state one-dimensional flow.
- The heat exchanger is adiabatic.
- Particles are of one size, the so-called monodisperse distribution.
- In every cross-section of the heat exchanger, particles have the same temperature.
- Each particle is at the same temperature radially.
- The radiation between particles and air is negligible.
- The effect of radiation between the particles and walls could be minimal and ignored for the scope of this thesis.
- Constant specific heat of air and particles

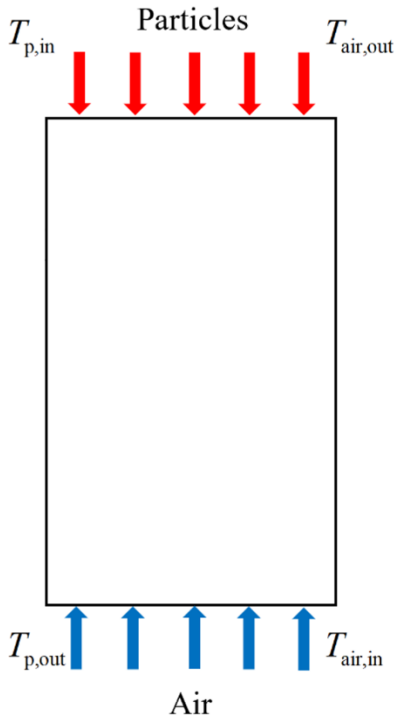

Figure 30. Schematic of the particle-air direct contact heat exchanger.

In this heat exchanger design, inlet air temperature is set to be 934.15 K with air temperature difference ΔT_{air} of 400 K to have outlet air temperature at 1334.15 K (*ca*. 1061 ºC). Those temperatures are compatible with the air breathing Brayton power cycle used for G3KSA project in Saudi Arabia. The high air temperature difference between the inlet and outlet is favorable for open cycle gas turbine and for thermal storage. The greater the difference in air temperature, the greater the energy storage per particle mass. The inlet and outlet particle temperatures are found using the following equations:

$$T_{p,in} = T_{air,out} + LMTD_{spec} \tag{14}$$

$$T_{\text{p,out}} = T_{\text{air,in}} + LMTD_{\text{spec}} \tag{15}$$

$LMTD_{\text{spec}}$ is the terminal temperature difference, which is the temperature difference at the top of the heat exchanger, and since the heat capacity rates of the particles and air are almost equal, the $LMTD_{\text{spec}}$ will be very close to the $LMTD$ for the entire heat exchanger. $LMTD_{\text{spec}}$ equals 50 K and is optimal for CSP application, so $T_{\text{p,in}}$ will equal 1384.15 K and $T_{\text{p,out}}$ will equal 984.15 K. Lower terminal temperature difference could be obtained for lower cost heat exchanger.

In this model, the height of the heat exchanger and the cross-sectional area that could achieve the designated air temperatures are investigated. EES model was built to iterate and solve the heat exchanger simulation to find the proper length of this DCHX that satisfies the air temperature constraint as in the following equations.

$$error = T_{\text{air,in,sim}} - T_{\text{air,in}} \tag{16}$$

$$error = 0 \tag{17}$$

The EES will iterate the heat exchanger model to find the proper length of the DCHX until the error equals zero. It was found necessary to do the simulation in a procedure to minimize the number of nonlinear equations.

In this model, the air pressure used to study this DCHX is 490 kPa and 800 kPa. These pressures are compatible with the power cycles considered for the project. 490 kPa pressure is considered for the Aurelia A1300 if it gets built, and 800 kPa is compatible with Frame 5 General Electric turbine with recuperator.

The mass flowrate of the working fluid (air) and ECM (particle) are assumed to be the same, and the specific heat of air and particles are almost the same. Hence, the heat capacity rates are almost identical, and the heat exchanger could be designed as a balanced flow. In this model, constant capacity rates are used to cut down some calculation, which should be modified in future work. The air specific heat is obtained knowing the air pressure and inlet and outlet temperatures using Equation (18). The particle specific heat is obtained at particle average temperature from the following formula based on the data from Sandia. And the then the heat capacity rate is found from Equation (20).

$$c_{p,\text{air}} = \frac{h_{\text{air,out}} - h_{\text{air,in}}}{\Delta T_{\text{air}}} \tag{18}$$

$$c_{p,\text{p}} = o.365\left(T_{\text{avg,p}} - 273.15\right)^{1.18} \tag{19}$$

$$C = \dot{m}\, c_p \tag{20}$$

The schematic below shows that the DCHX is divided into numerous infinitesimal slices (control volumes), in which energy and momentum balances are conducted across each slice. The temperature profile of particles and air and the net heat exchange rate between them are obtained using the following equations.

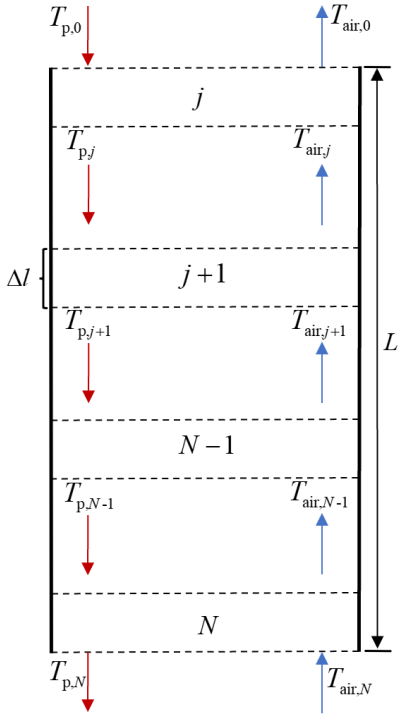

Figure 31. Schematic of heat exchanger infinitesimal slices.

$$\dot{Q}_j = UA_j \, LMTD_j \tag{21}$$

Where $\dot{Q}_j$ is the heat transfer between the particles and air (W), UA_j is the total thermal conductance (W/K), and $LMTD_j$ is the log mean temperature difference in each slice of the heat exchanger (K). Since the heat exchanger is balanced flow, the log mean temperature difference will be calculated as following:

$$LMTD_j = T_{p,j} - T_{air,j} \tag{22}$$

And the total thermal conductance is found through the following formula.

$$UA_j = h_{p,j}\left(\rho_{N,j}\, A_{s,p}\, \Delta V_{DCHX}\right) \tag{23}$$

Where $h_{p,j}$ is the heat transfer coefficient (W/m^{2}K) of spherical particle, $\rho_{N,j}$ is number density of particles in control volume per volume unit (1/m^3), $A_{s,p} = \pi D_p^2 = 4 A_{CS,p}$ is the particle surface area (m^2), $\Delta V_{DCHX} = \Delta l\, A_{CS,DCHX}$ is the elemental heat exchanger volume (m^3).

$$h_{p,j} = Nu_{p,j}\frac{k_j}{D_p} \tag{24}$$

Where $Nu_{p,j}$ is Nusselt number, k_j is air thermal conductivity found by EES built in function, and D_{par} is particle diameter (m). EES uses reliable data to find the value of $Nu_{p,j}$.

$$\rho_{N,j} = \frac{\dot{m}_{ECM}}{A_{CS,DCHX}\, m_p\, V_{p,j}} \tag{25}$$

Where $\dot{m}_{ECM}$ is mass flow rate of particles as energy carrier medium (kg/s), $A_{CS,DCHX}$ is the cross sectional area of the DCHX (m^2) and was set to be 1.0 m^2 to have calculations per unit area, $V_{p,j}$ is the velocity of the particle (m/s), it will be shown how it was found in the analysis below, $m_p = V_p\, \rho_p$ is the mass of a single particle (kg), $V_p = \frac{\pi D_p^3}{6}$ is the particle volume (m^3)

Once the heat rate is found, the following equations are used to determine the particle and air temperatures.

$$\Delta T_{air,j} = \dot{Q}_j \frac{0.001\frac{kW}{W}}{C_{air}} \tag{26}$$

$$T_{\text{air},j} = T_{\text{air},j-1} - \Delta T_{\text{air},j} \tag{27}$$

$$\Delta T_{\text{p},j} = \dot{Q}_j \frac{0.001\frac{\text{kW}}{\text{W}}}{C_{\text{ECM}}} \tag{28}$$

$$T_{\text{p},j} = T_{\text{p},j-1} - \Delta T_{\text{p},j} \tag{29}$$

The total heat transfer between the particles and air in this DCHX, which is the sum of heat transfers in all the slices, is then calculated by the following equation:

$$\dot{Q}_{\text{DCHX,sim}} = \sum_{j=1}^{N_{\text{slices}}} \dot{Q}_j \tag{30}$$

The cross-sectional area of the DCHX associated with 1MW heat transfer in the heat exchanger is investigated and found using the following formulas.

$$\dot{Q}_{Design} = 1\text{MW} \tag{31}$$

$$A_{\text{CS,DCHX,Design}} = \frac{\dot{Q}_{\text{Design}}\, A_{\text{CS,DCHX}}}{\dot{Q}_{\text{DCHX,sim}}} \tag{32}$$

The designed heat exchanger volume then will be found using the following equation:

$$V_{\text{DCHX,Design}} = A_{\text{CS,DCHX,Design}}\, L_{\text{DCHX}} \tag{33}$$

The dynamics of this heat exchanger simulation is important and began by finding the air velocity at the bottom of any slice using the following equation:

$$V_{\text{air},j} = \frac{\dot{m}_{\text{air}}}{\rho_{\text{air},j} A_{\text{CS,DCHX}}} \tag{34}$$

Where $\dot{m}_{\text{air}}$ is air mass flow rate (kg/s), $\rho_{\text{air},j}$ is air density (kg/m^3), EES is used to find its value at every slice knowing the air temperature at that slice.

The initial velocity of the particle $V_{\text{p},0}$ when it enters the top of the heat exchanger and before it interacts with air is given to be 1.0 m/s. This initial velocity of particle can easily be achieved by dropping the particles in the still air before it encounters the pressured air. The particle velocity is crucial since it influences the particle number density. As particle velocity rises, particle number density drops. When the particle velocity decreases, the particle number density increases, threatening to halt the particles; hence, no steady-state solution is available. Thus, too low particle velocity must be avoided to maintain a steady-state solution.

The following equation is then used to find the particle velocity in all the slices through the heat exchanger. The derivation of this formula can be found in the Appendix A.

$$V_{\text{p},j} = \frac{2\left(F_{\text{g}} - F_{\text{D},j}\right) dl}{m_{\text{p}}\left(V_{\text{p},j} + V_{\text{p},j-1}\right)} + V_{\text{p},j-1} \tag{35}$$

Where $F_{\text{g}} = m_{\text{par}}\, g$ is the gravity force acting on the particle (N), and $F_{\text{D},j}$ is the drag force exerted by the air on the particle (N) and can be found by the following formula:

$$F_{D,j} = \frac{C_{D,p}\, A_{CS,p}\, \rho_{air,j}\, V_{rel,j}^2}{2} \tag{36}$$

Where $C_{D,p}$ is the drag coefficient and EES uses reliable data to find its value, $A_{CS,p} = \frac{\pi D_p^2}{4}$ is the cross section area of the particle (projected area normal to the movement direction), and $V_{rel,j} = V_{air,j-1} + V_{p,j-1}$ is the relative velocity of air with respect to particle (m/s).

The momentum balance was performed, and the linear momentum equation was derived using Newton's 2nd Law, the derivation can be found in Appendix B. The pressure-drop in this direct contact heat exchanger can be found with neglecting the weight of the air within the control volume from the following equation:

$$\left(P_{Bot} - P_{Top}\right) = \Delta P_{DCHX} = \frac{\dot{m}_{air}\left(V_{Top} - V_{Bot}\right)_{air} + \dot{m}_p\left(V_{Bot} - V_{Top}\right)_p + F_{g,ECM}}{A_{DCHX,CS}} \tag{37}$$

The weight is only the weight of the particles inside the control volume which can be found as the following:

$$F_{g,ECM} = g\, m_{ECM} \tag{38}$$

Since the heat exchanger in the model was divided into small slices, the mass of the particles in the control volume is going to be sum of the mass of all slices and can be found as shown below:

$$m_{\mathrm{ECM}} = \sum_{j=1}^{\mathrm{N\_steps}} \rho_{\mathrm{N},j}\, m_{\mathrm{p}}\, \Delta V_{\mathrm{DCHX}} \tag{39}$$

Another approach to find the total pressure drop in the heat exchanger is by finding the pressure drop due to the drag on the particles and pressure drop due to momentum in all slices through the heat exchanger. Then the total pressure drop of this DCHX is obtained by finding the pressure difference at the top and bottom of the heat exchanger using the following equations.

$$\Delta P_{DCHX} = P_{\mathrm{air,N}} - P_{\mathrm{air},0} \tag{40}$$

$$P_{\mathrm{air},j} = P_{\mathrm{air},j-1} + \left(\Delta P_{\mathrm{drag},j} + \Delta P_{\mathrm{mom},j}\right)\left(0.001\frac{\mathrm{kPa}}{\mathrm{Pa}}\right) \tag{41}$$

Where the pressure drop at every slice is due to the change of the linear momentum and drag force on air.

$$\Delta P_{\mathrm{mom},j} = \frac{\dot{m}_{\mathrm{air}}}{A_{\mathrm{CS,DCHX}}}\left(V_{\mathrm{air},j-1} - V_{\mathrm{air},j}\right) \tag{42}$$

$$\Delta P_{\mathrm{drag},j} = \rho_{\mathrm{N},j}\, F_{\mathrm{D},j}\, \Delta l \tag{43}$$

Where Δl is the length of each slice and the change in overall length of fall.

To check the accuracy of the model dynamics, the particle velocity was simulated at free fall acceleration, which is much more than the acceleration in this DCHX model, and then

compared to the calculated values. As it will be shown in the results, the dynamics of this model shows an adequate resolution even with very high acceleration.

The following equations are used to check the fractional volume of air and particles. It is important to know the volume of the heat exchanger that is occupied by air and the particles.

$$V_{\text{air},\%,j} = 1 - V_{\text{p},\%,j} \tag{44}$$

$$V_{\text{p},\%,j} = \rho_{\text{N},j} - V_{\text{p}} \tag{45}$$

5.4 Conclusion

This analytical model was successfully simulated using EES, and the outcomes will be presented in the following chapter. To investigate the performance of this DCHX, a model comprised of many simultaneous equations was initially developed. Nonetheless, the model got complex due to the multiple equations. Consequently, as described previously, a new technique was used to simulate this DCHX by employing sequential equations. The EES model was iterated in order to simulate the heat exchanger and evaluate its characteristics, such as the optimal length of the DCHX, cross-sectional area, volume, temperature and velocity profiles, and many others. This heat exchanger's simulation was conducted using a procedure that minimized the number of nonlinear equations. This successful approach showed good accuracy in modeling this DCHX and investigating the thermal and dynamic performance.

CHAPTER 6. RESULTS AND DISCUSSION

This thesis explored many aspects and characteristics of DCHX; the results are given in the following sections. As mentioned in the last chapter, this DCHX was simulated using EES. As stated in the table below, some educated input data was utilized to construct the DCHX and run the model based on the G3KSA project's power cycle, particle type, and literature review.

Table 14. Input data used to simulate the DCHX.

Parameter	Value	Description
Inlet air temperature $T_{air,in}$	934.15 K	These temperatures are compatible with the air-breathing Brayton cycle for G3KSA.
Outlet air temperature $T_{air,out}$	1334.15 K	
Air temperature difference ΔT_{air}	400 K	
Inlet particles temperature $T_{p,in}$	1384.15 K	This difference is the terminal temperature difference, and 50K is considered to be near optimal for CSP applications.
Outlet particles temperature $T_{p,out}$	984.15 K	
Designed log mean temperature difference $LMTD_{spec}$	50 K	

Table 14 continued

Particles mass flowrate $\dot{m}_{ECM}$	4.0 kg/s	Energy carrier medium mass flow rate.
Particle diameter D_p	0.6 mm	The diameter will be varied in the study.
Particle bulk density $\rho_{ECM,bulk}$	1810 kg/m^3	The density of the bulk of energy carrier medium bulk and, it is used to find the particle density.
Initial particle velocity $V_{p,0}$	1.0 m/s	The velocity that particles enter the DCHX.
Air pressure P_{air}	490 & 800 kPa	Operating air pressures used for Aurelia A1300 and Fram 5 General Electric turbines.

Several cases are conducted to investigate the dynamics and thermal performance of the heat exchanger based on the particle diameter and operating pressure and will be presented in the following sections.

6.1 Operating Pressure of 490 kPa

The air pressure of 490 kPa is suitable with the Aurelia A1300 and the power cycle with approximately optimal 4:1 pressure ratio. The effect of varying particle diameters on the dynamics and thermal performance of DCHX is investigated at the same initial particle velocity of 1.0 m/s and terminal temperature difference of 50 K.

6.1.1 Particle Diameter of 0.6 mm

Using a mass flow rate of 4.0 kg/s, Figure 32 shows the velocity profiles of the air and particles, particle number density, and fractional air volume. As predicted, the air velocity increased as it got heated through the heat exchanger, the highest air velocity was achieved at the top of the DCHX (the top is at 0.0 m in the figure). Increasing the temperature of the air reduces its density, and to maintain constant air flow rate, the air velocity will increase. In contrast, the particles' velocity decreased after entering the DCHX. Shortly after overcoming the force of drag, the velocity of the particles accelerated and increased. The average air velocity in the DCHX was 2.63 m/s, whereas the average particle velocity was 0.70 m/s. The particle number density is inversely proportional to the particle velocity. The particle number density rises when the particle velocity decreases, as shown in the figure. The highest particle number density was achieved when the particle velocity was at the lowest. The average particle number density throughout the DCHX was 18×10^6 $1/m^3$. The figure also shows that the heat exchanger volume is mainly occupied by the air, which indicates no particle agglomeration and a reasonable steady-state solution.

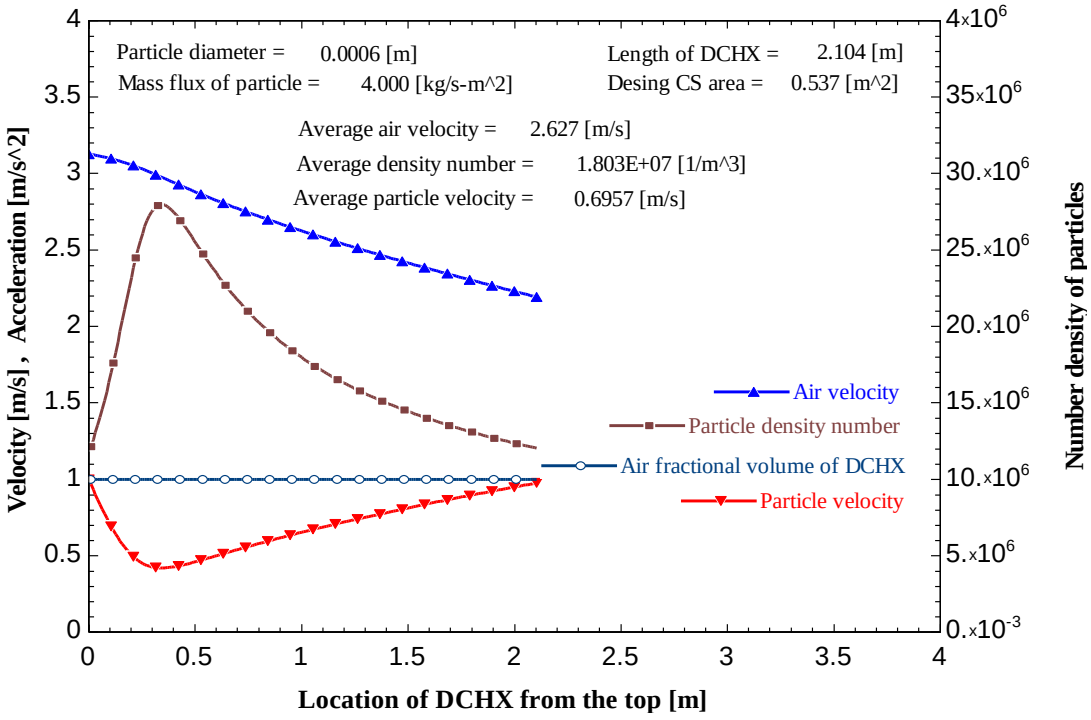

Figure 32. Dynamics of DCHX with 0.6 mm particle diameter.

In this instance, the DCHX was discovered to have a length of 2.10 m, a cross-sectional area of 0.54 m^2, and a volume of 1.13 m^3. The air pressure drop in this case was insignificant with a value of 131 Pa.

Figure 33 shows the temperature profiles of the air and particles throughout the heat exchanger. The temperature profiles are nearly straight lines with almost the same *LMTD* over the DCHX. As expected, the air temperature increased as it ascended through the heat exchanger, reaching its maximum at the top. While the particles cooled down and reached the lowest temperature at the bottom of the DCHX. The total heat transfer between the particles and air in the heat exchanger was 1.86 MW.

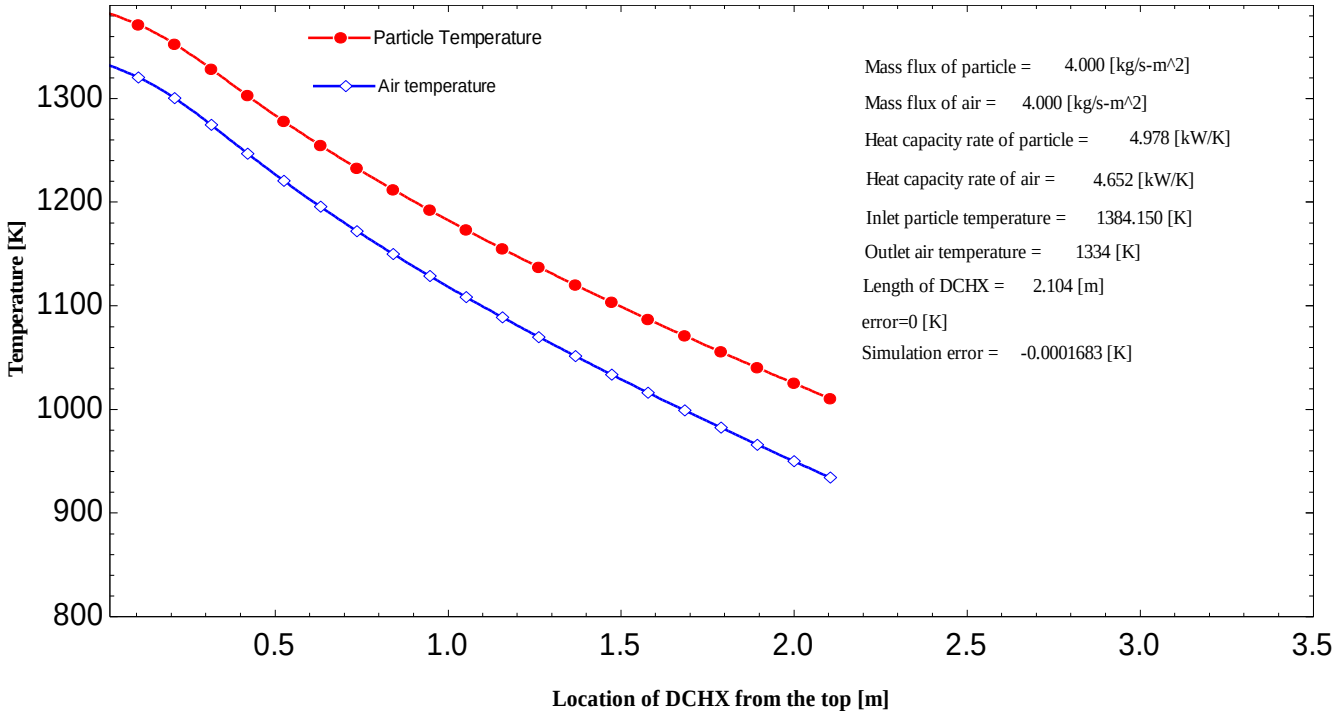

Figure 33. Temperature profiles of air and particles of DCHX with 0.6 mm particle diameter.

6.1.2 Particle Diameter of 0.3 mm

In this case, when the particle diameter was smaller than in the previous scenario, the mass flow rate was reduced to 0.5 kg/s. Otherwise, the air velocity would be excessive for this small particle size.

Figure 34 shows the velocity profiles of the air and particles, particle number density, and fractional air volume. As in the prior investigation, a similar trend was seen for velocity profiles and particle number density. The average air velocity in the DCHX was 0.33 m/s which was less than in the previous situation due to the air mass flow rate reduction. The average particle velocity was 1.30 m/s, which is more than in the preceding scenario because the particles faced less drag. The average particle number density across the DCHX was 9.57×10^{6} particles per cubic meter,

which is lower than the preceding case due to the increased particle velocities. The graphic also demonstrates that air primarily occupies the heat exchanger volume.

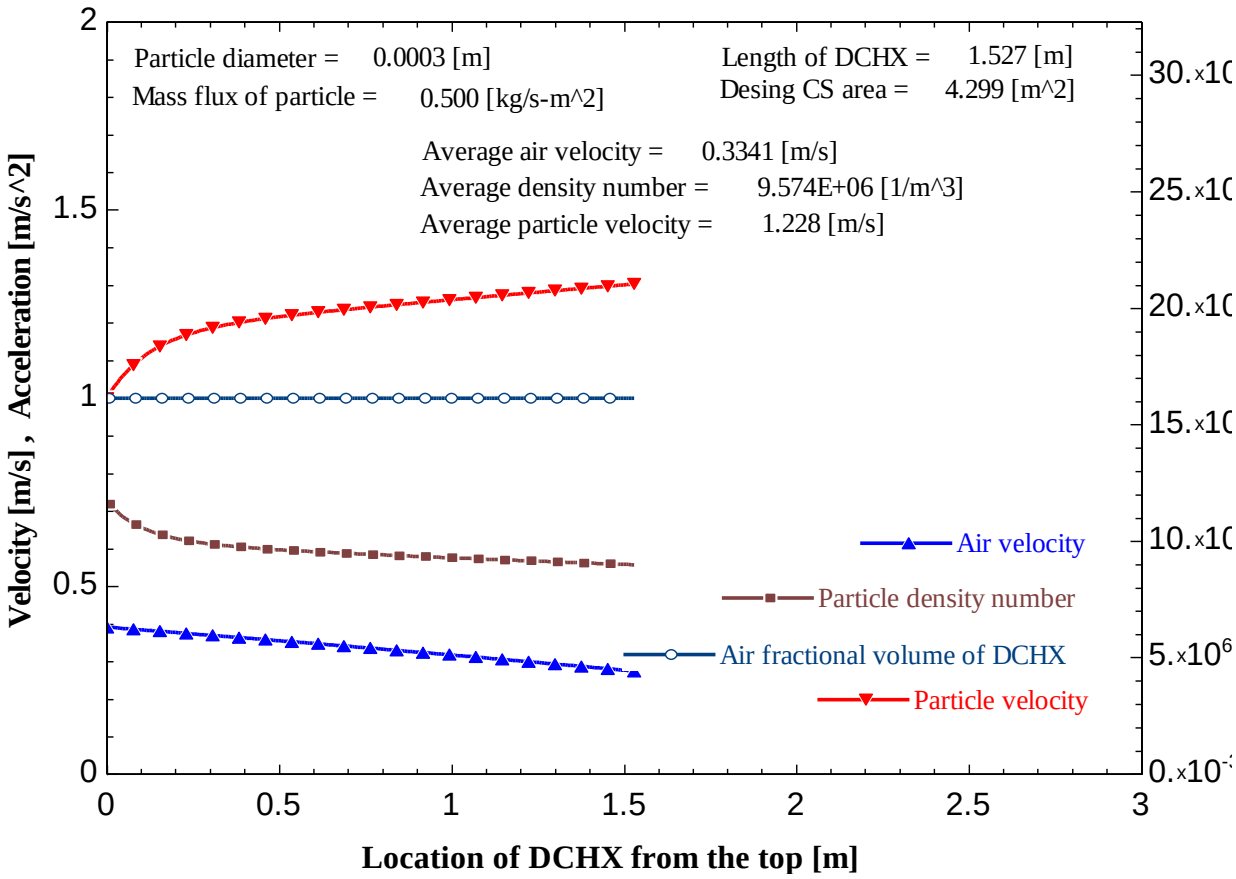

Figure 34. Dynamics of DCHX with 0.3 mm particle diameter.

In this instance, the DCHX was discovered to have a length of 1.53 m, a cross-sectional area of 4.30 m^2, and a volume of 6.57 m^3, which is much larger than the previous case because of the much lower mass flux density. The air pressure drop in this case was almost zero.

Figure 35 shows the temperature profiles of the air and particles throughout the heat exchanger in these conditions. The temperature profiles are nearly straight lines with almost the same LMTD over the DCHX. The total heat transfer between the particles and air in the heat exchanger was 233 kW.

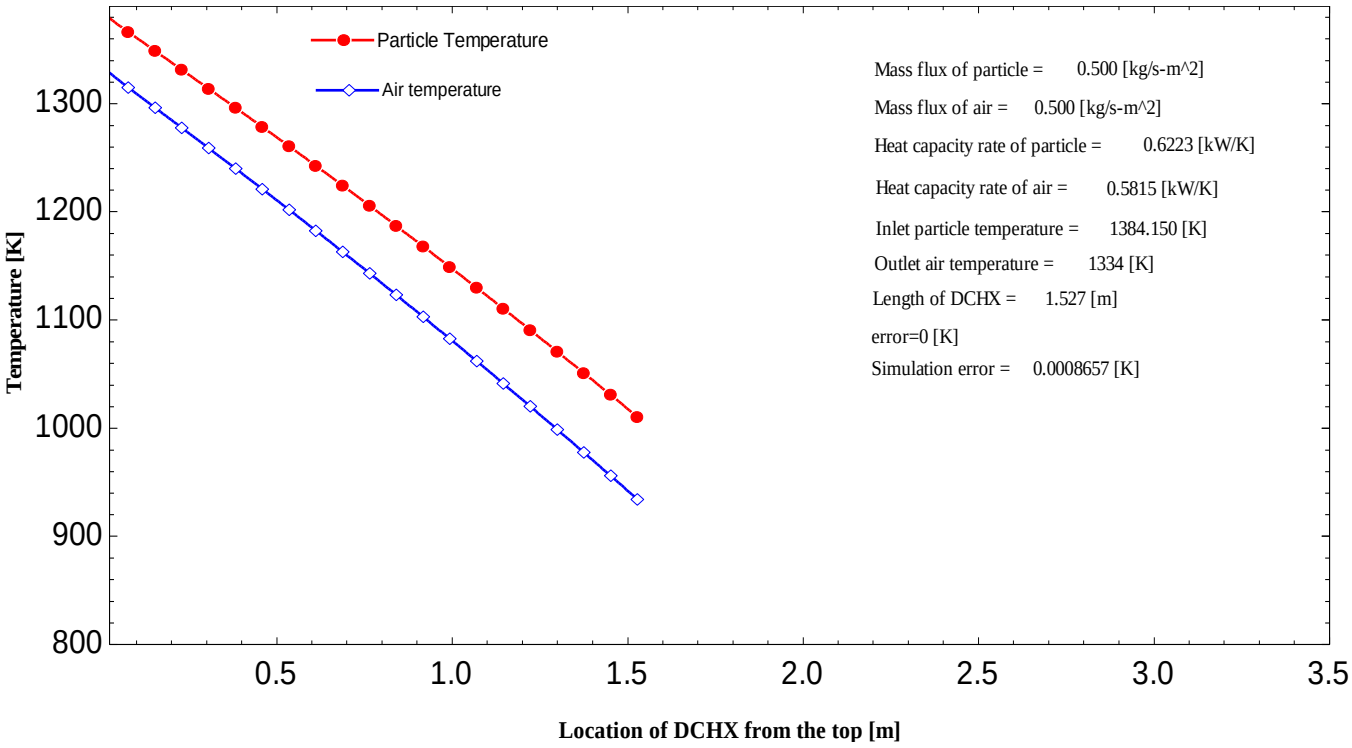

Figure 35. Temperature profiles of air and particles of DCHX with 0.3 mm particle diameter.

6.1.3 Particle Diameter of 0.9 mm

The mass flow rate was raised to 6.0 kg/s when the particle diameter was greater than in the initial investigation. Figure 36 depicts the velocity profiles of air and particles, particle number density, and fractional air volume. The velocity profiles and particle number density exhibited the

same pattern as in previous studies. Due to the increase in air mass flow rate, the average air velocity in the DCHX was 4.0 m/s, which was greater than in the initial condition. The average particle velocity was 0.83 m/s, which is marginally more than in the first case due to the greater distance particles traversed. The DCHX had an average particle number density of 7×10^6 particles per cubic meter. Additionally, the diagram illustrates that air mainly covers the heat exchanger volume.

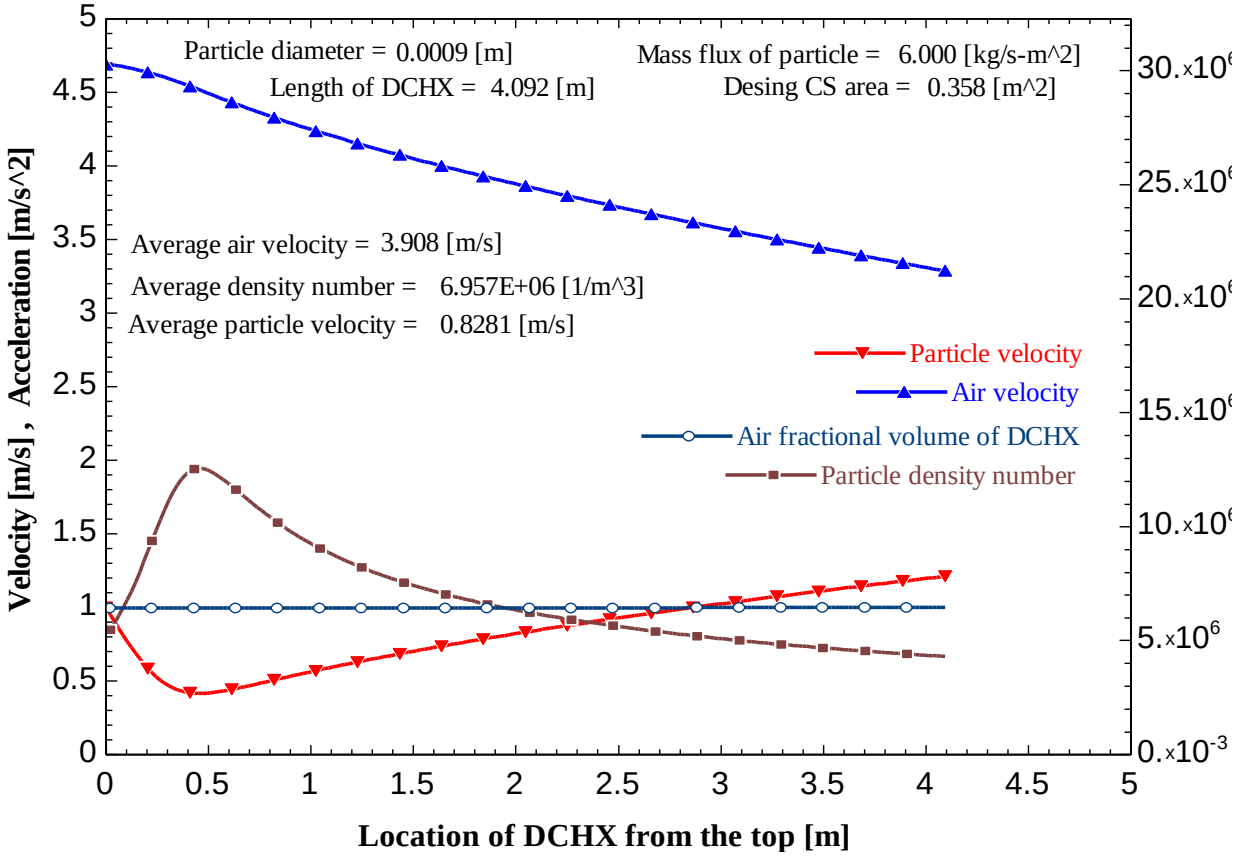

Figure 36. Dynamics of DCHX with 0.9 mm particle diameter.

In this instance, the DCHX was discovered to have a length of 4.0 m, , which is much longer and less desirable than in the preferred case, a cross-sectional area of 0.36 m^2, and a volume of 1.47 m^3. The air pressure drop in this case was also insignificant with a value of 330 Pa.

Figure 37 shows the temperature profiles of the air and particles throughout the heat exchanger in these conditions. The temperature profiles are nearly straight lines with almost the same *LMTD* over the DCHX. The total heat transfer between the particles and air in the heat exchanger was 2.79 MW.

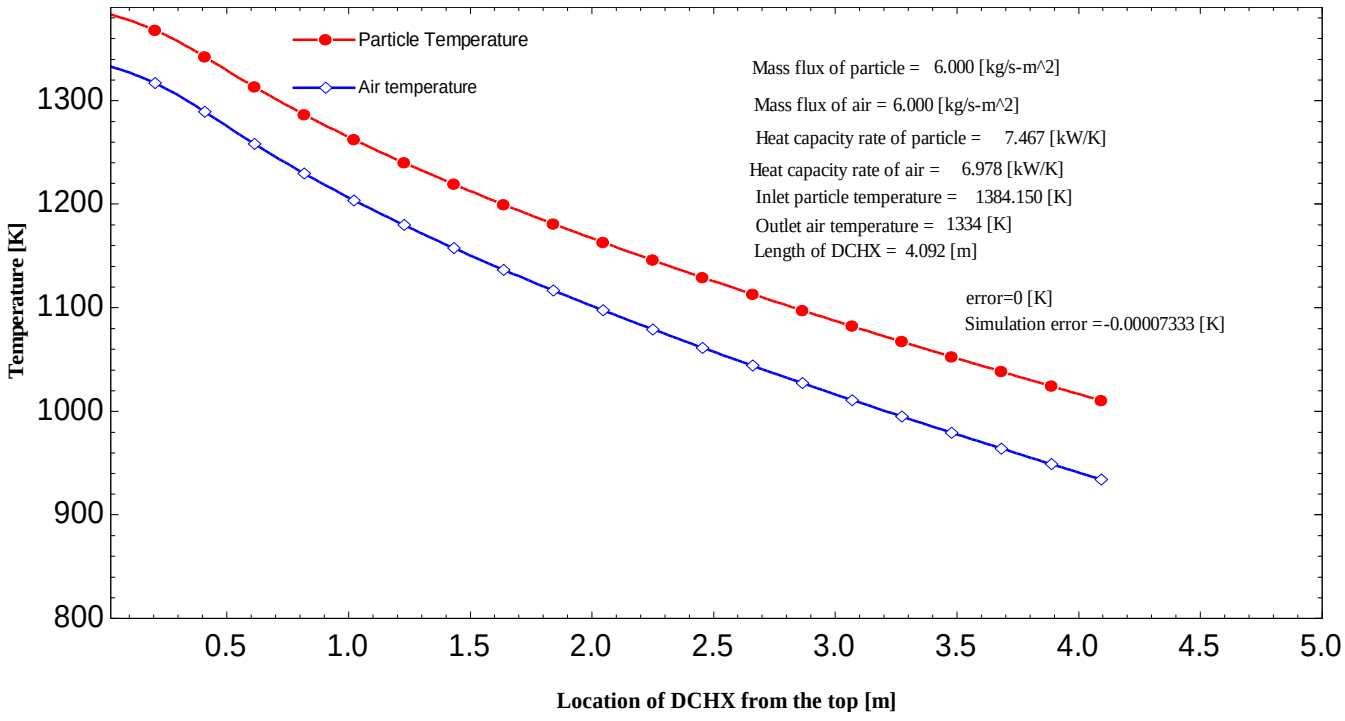

Figure 37. Temperature profiles of air and particles of DCHX with 0.9 mm particle diameter.

The table below summarizes the significant outcomes of the previous three cases of different particle diameters to compare their performance and practicality.

Table 15. Results summary of the different particle diameter cases.

D_p (m)	$\dot{m}_{ECM}$ (kg/s)	$\dot{m}_{air}$ (kg/s)	$\dot{Q}$ (W)	L_{DCHX} (m)	$A_{CS,DCHX,Design}$ (m^2)	$V_{DCHX,Design}$ (m^3)
0.0003	0.5	0.5	233000	1.527	4.299	6.567
0.0006	4.0	4.0	1860000	2.104	0.537	1.131
0.0009	6.0	6.0	2791000	4.092	0.358	1.466

D_p (m), particle diameter; $\dot{m}$ (kg/s), mass flowrate; $\dot{Q}$ (W), heat transfer rate; L_{DCHX} (m), DCHX length; $A_{CS,DCHX,Design}$ (m^2), DCHX cross-sectional area; $V_{DCHX,Design}$ (m^3), DCHX volume.

The results of the 0.3 mm particle diameter show that this particle size is impractical for designing this DCHX. The large cross-sectional area, and consequently the high volume, is unsuitable for the solar tower project. The 0.9mm particle diameter case has a good DCHX cross-sectional area and volume. However, the length of this heat exchanger may restrict its applicability if the design of the solar tower cannot allow a tall heat exchanger. The particle diameter of 0.6 mm yields better outcomes. In this scenario, the cross-sectional area, volume, and length of the DCHX are viable for the design of this heat exchanger. The particle diameter of 0.6 mm appears to be the most practical among the three scenarios for the design of this DCHX.

6.2 Operating Pressure Of 800 kPa

The air pressure of 800 kPa is compatible with the Frame 5 General Electric turbine with recuperator and the power cycle with 8:1 pressure ratio. The effect of varying particle diameters on the dynamics and thermal performance of DCHX is investigated at the same initial particle velocity of 1.0 m/s, and terminal temperature difference of 50 K. Under this operating pressure, only particles diameter of 0.6 mm and 0.9 mm are considered to investigate.

6.2.1 Particle Diameter of 0.6 mm at 800 kPa

Figure 38 illustrates the velocity profiles of the air and particles, particle number density, and fractional air volume using a mass flow rate of 4.0 kg/s. The velocity profiles and particle number density displayed the same pattern as previous research conducted at 490 kPa. The average air velocity in the DCHX was 1.63 meters per second, whereas the average particle velocity was 1.14 meters per second. The average particle number density in the DCHX was 10×10^6 $1/m^3$. The figure also demonstrates that air primarily occupies the heat exchanger volume.

In this instance, the DCHX was discovered to have a length of 3.28 m, a cross-sectional area of 0.54 m^2, and a volume of 1.77 m^3. The pressure drop in this case was insignificant with a value of 115 Pa.

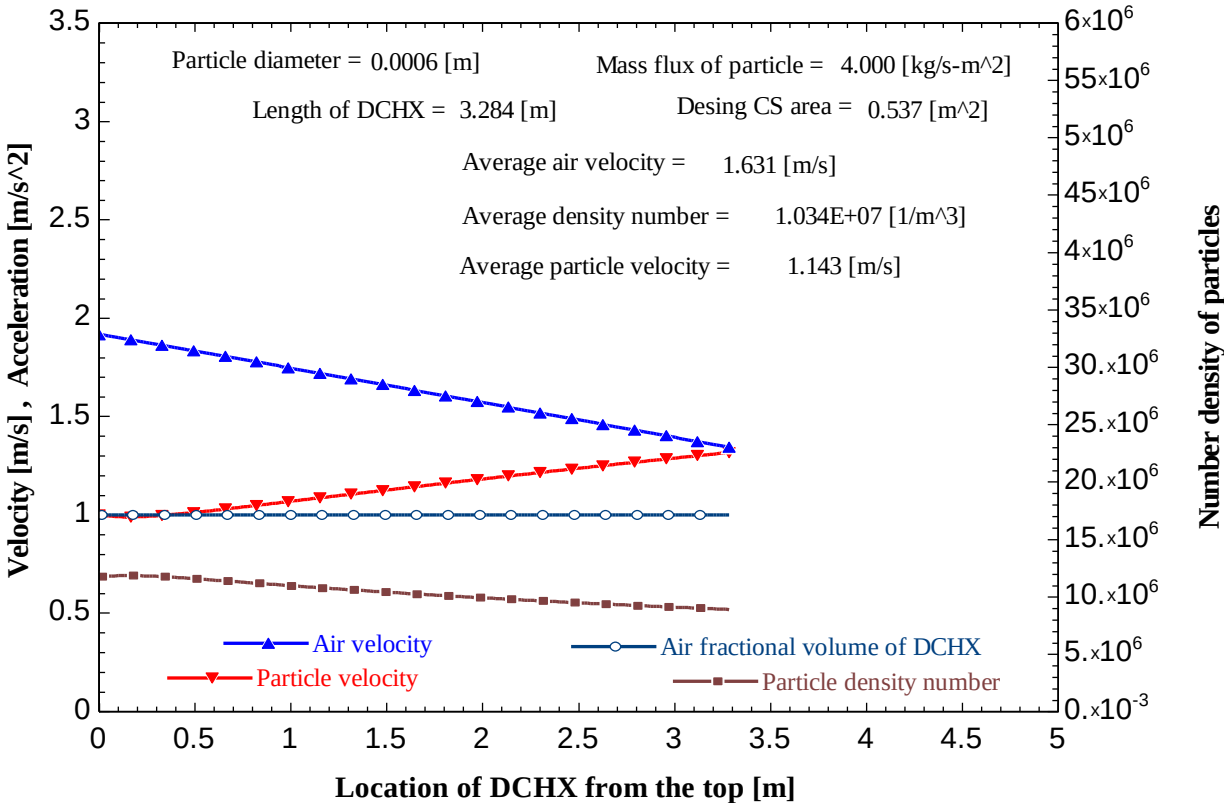

Figure 38. Dynamics of DCHX with 0.6 mm particle diameter 800 kPa case.

Figure 39 illustrates the air and particle temperature profiles across the heat exchanger. Over the DCHX, the temperature profiles are almost straight lines with approximately the same LMTD. 1.86 MW of heat was transferred between particles and air in the heat exchanger.

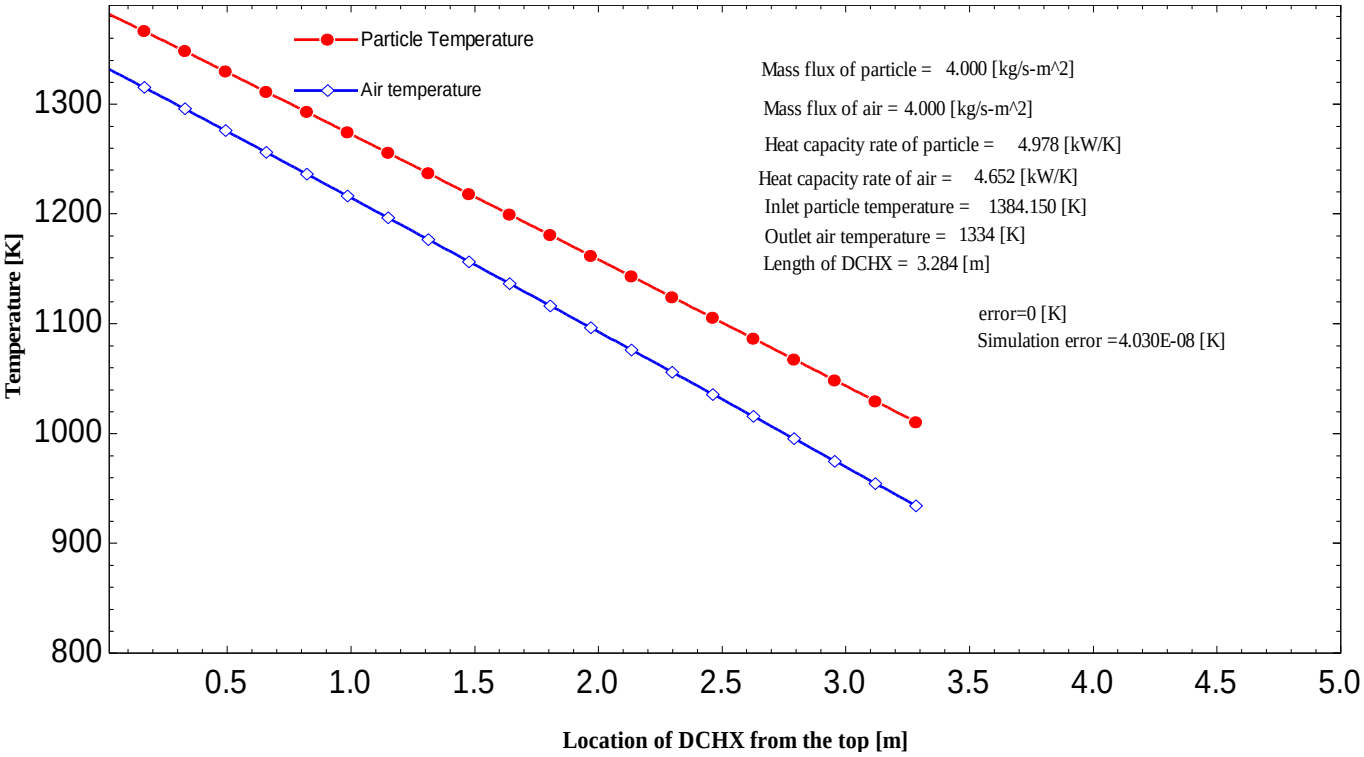

Figure 39. Temperature profiles of air and particles of DCHX with 0.6 mm particle diameter at 800 kPa.

6.2.2 Particle Diameter of 0.9 mm at 800 kPa

In this investigation, the mass flow rate was increased to 6.0 kg/s, like in the 490 kPa case. The velocity profiles of air and particles, particle number density, and fractional air volume are shown in Figure 40. The velocity profiles and particle number density displayed the same pattern as in the previous studies. In the DCHX, the average air velocity was 2.44 m/s, and the average particle velocity was 1.47 m/s. The average particle number density of the DCHX was 3.6×10^{6} particles per cubic meter. Moreover, the figure demonstrates that air predominantly filled the heat exchanger volume.

In this instance, the DCHX was discovered to have a length of 7.0 m, a cross-sectional area of 0.36 m^2, and a volume of 2.52 m^3. The pressure drop in this case was insignificant with a value of 290 Pa.

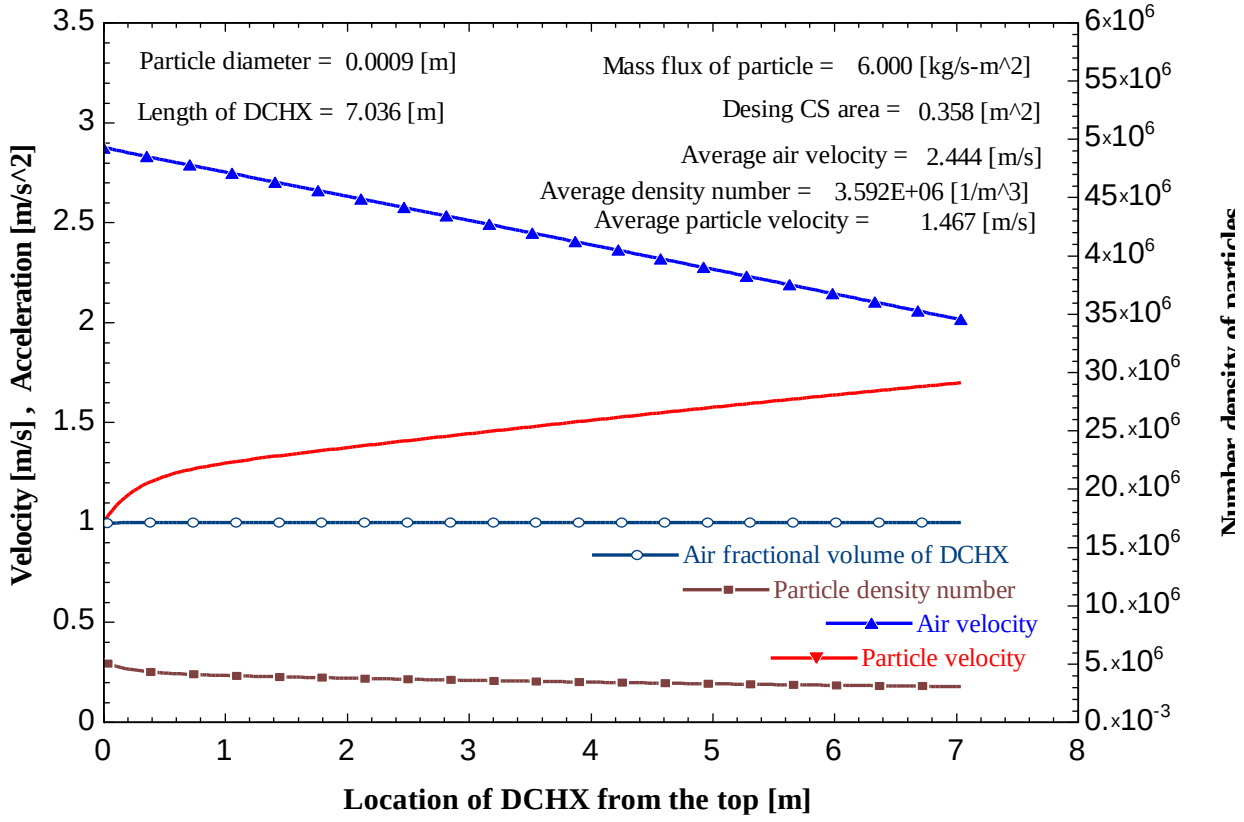

Figure 40. Dynamics of DCHX with 0.9 mm particle diameter 800 kPa case.

Figure 41 displays the temperature profiles of the air and particles over the heat exchanger. The temperature profiles over the DCHX are almost straight lines with almost the same LMTD. In the heat exchanger, 2.8 MW of heat was transported between particles and air.

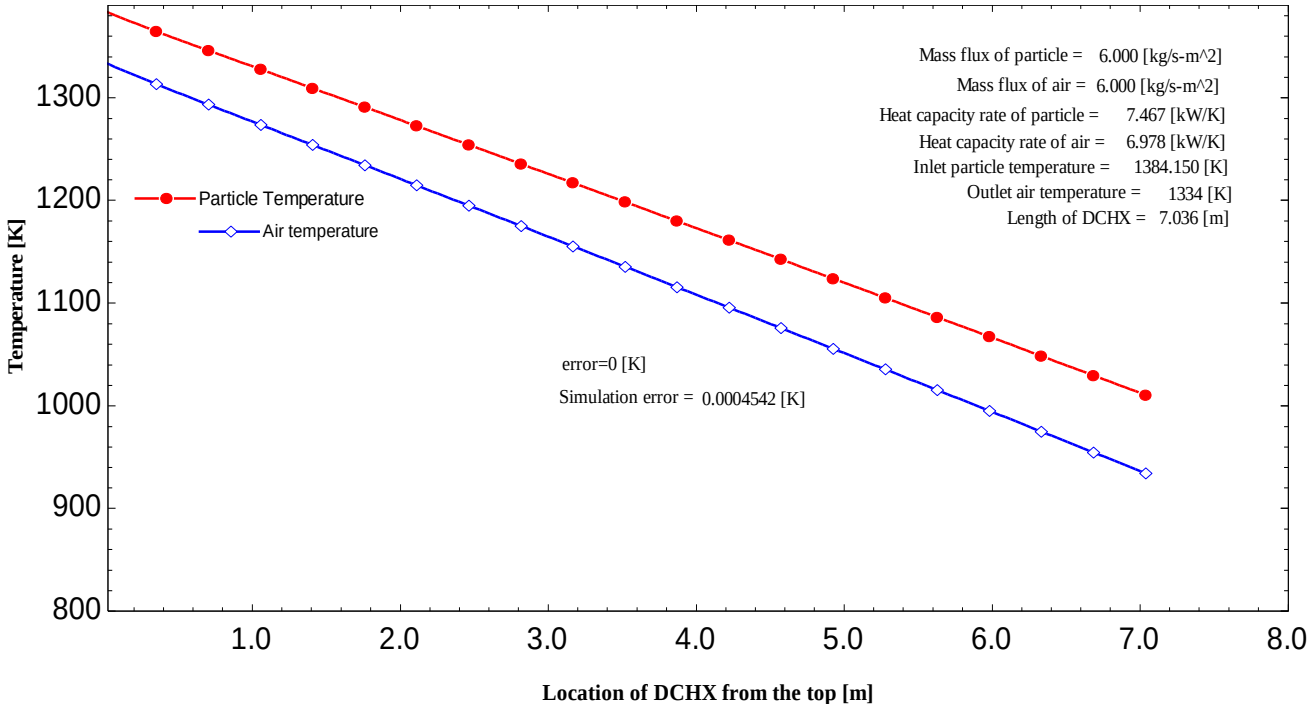

Figure 41. Temperature profiles of air and particles of DCHX with 0.9 mm particle diameter 800 kPa case.

The table below summarizes and compares the performance of the preceding two scenarios involving particles with different diameters.

Table 16. Results summary of the different particle diameter at 800 kPa cases.

D_p (m)	$\dot{m}_{ECM}$ (kg/s)	$\dot{m}_{air}$ (kg/s)	$\dot{Q}$ (W)	L_{DCHX} (m)	$A_{CS,DCHX,Design}$ (m^2)	$V_{DCHX,Design}$ (m^3)
0.0006	4.0	4.0	1861000	3.284	0.537	1.765
0.0009	6.0	6.0	2791000	7.036	0.358	2.521

D_p (m), particle diameter; $\dot{m}$ (kg/s), mass flowrate; $\dot{Q}$ (W), heat transfer rate; L_{DCHX} (m), DCHX length; $A_{CS,DCHX,Design}$ (m^2), DCHX cross-sectional area; $V_{DCHX,Design}$ (m^3), DCHX volume.

Again, the 0.6 mm particle diameter produced superior outcomes to the 0.9 mm particle diameter. Therefore, the 0.6 mm particle diameter is practical for the design of this DCHX with 800 kPa operating pressure.

6.3 Dynamics Simulation Check

The free fall condition was solved to assess the simulation's correctness in the model and evaluate the findings of the dynamic. The velocity of particles in free fall was simulated, calculated, and compared. The calculated velocity of a particle was 6.503 m/s, while the simulated velocity was 6.518 m/s. As can be seen, the calculated value and the simulated value are in excellent agreement even though only a small number (only 200) of simulation steps are used. Consequently, if it was feasible to properly simulate the free fall velocity of particles at a far greater acceleration than the actual acceleration in this DCHX model, it demonstrates that the dynamics model is highly accurate.

6.4 Parametric Studies

In this section, several parametric studies are carried out to investigate the effects of some parameters on the performance and design of the DCHX. In the following studies, the particle diameter of 0.6 mm is used as it showed better results in the previous cases.

6.4.1 Mass flow rate parametric study

In this section, the mass flow rate of the particles and air changes while all other parameters remain constant to evaluate the influence of the mass flow rate on the DCHX design. The initial air velocity was set at 1.0 m/s, and the terminal temperature difference was 50 K. The two tables below show the results of the parametric study at 490 kPa and 800 kPa operating pressures.

As seen in the data below, increasing the air and particle mass flow rates considerably improves the DCHX's performance. As the mass flow rate increased, the required length of the heat exchanger to obtain the temperatures necessary for the power cycle reduced. The cross-sectional area of the DCHX exhibited a similar tendency, as it shrunk as the mass flow rate increased. Consequently, the total volume of this DCHX followed the same pattern and was smallest with values of 1.13 m^3 and 1.77 m^3 at 490 kPa and 800 kPa, respectively, when the mass flow rate was greatest with a value of 4.0 kg/s.

Table 17. Parametric study of mas flowrate for 0.6 mm particle diameter at 490 kPa and 1.0 m/s.

$\dot{m}_{ECM}$ (kg/s)	$\dot{m}_{air}$ (kg/s)	$\dot{Q}$ (W)	L_{DCHX} (m)	$A_{CS,DCHX,Design}$ (m^2)	$V_{DCHX,Design}$ (m^3)
2.00	2.00	930000	6.26	1.075	6.731
2.22	2.22	1034000	5.80	0.967	5.607
2.44	2.44	1137000	5.33	0.879	4.689
2.67	2.67	1240000	4.87	0.806	3.924
2.89	2.89	1344000	4.41	0.744	3.278
3.11	3.11	1447000	3.94	0.691	2.724
3.33	3.33	1551000	3.48	0.645	2.245
3.56	3.56	1654000	3.02	0.605	1.827
3.78	3.78	1757000	2.56	0.569	1.458
4.00	4.00	1861000	2.10	0.537	1.131

$\dot{m}$ (kg/s), mass flowrate; $\dot{Q}$ (W), heat transfer rate; L_{DCHX} (m), DCHX length; $A_{CS,DCHX,Design}$ (m^2), DCHX cross-sectional area; $V_{DCHX,Design}$ (m^3), DCHX volume.

Table 18. Parametric study of mas flowrate for 0.6 mm particle diameter at 800 kPa and 1.0 m/s.

$\dot{m}_{ECM}$ (kg/s)	$\dot{m}_{air}$ (kg/s)	$\dot{Q}$ (W)	L_{DCHX} (m)	$A_{CS,DCHX,Design}$ (m^2)	$V_{DCHX,Design}$ (m^3)
2.00	2.00	930000	5.58	1.075	6.000
2.22	2.22	1034000	5.33	0.967	5.151
2.44	2.44	1137000	5.07	0.879	4.457
2.67	2.67	1241000	4.81	0.806	3.879
2.89	2.89	1344000	4.56	0.744	3.391
3.11	3.11	1447000	4.30	0.691	2.972
3.33	3.33	1551000	4.05	0.645	2.610
3.56	3.56	1654000	3.79	0.605	2.293
3.78	3.78	1757000	3.54	0.569	2.013
4.00	4.00	1861000	3.28	0.537	1.765

$\dot{m}$ (kg/s), mass flowrate; $\dot{Q}$ (W), heat transfer rate; L_{DCHX} (m), DCHX length; $A_{CS,DCHX,Design}$ (m^2), DCHX cross-sectional area; $V_{DCHX,Design}$ (m^3), DCHX volume.

6.4.2 Operating pressure parametric study

In this part, the operating pressure is varied while all other parameters are held constant in order to analyze the pressure's effect on the DCHX design. The initial air velocity was set to 1.0 m/s, terminal temperature differential at 50 K, and mass flow rate to 4.0 kg/s. The outcomes of this parametric study are shown in the table below.

As seen by the data below, raising the operating pressure has a negative impact on the performance of DCHX. As the air pressure rises, the air density rises, resulting in a reduction in air velocity. As the working pressure increased in this investigation, the needed length of the heat exchanger to achieve the temperatures required for the power cycle increased. Changing the pressure did not affect the cross-sectional area of the DCHX because it did not affect the heat transfer rate. Therefore, the total volume of this DCHX grew with increasing pressure, reaching a maximum of 1.79 m^3 at a pressure of 850 kPa.

Table 19. Parametric study of air pressure for 0.6 mm particle diameter at 1.0 m/s.

P_{air} (kPa)	$\dot{m}_{ECM}$ (kg/s)	$\dot{Q}$ (W)	L_{DCHX} (m)	$A_{CS,DCHX,Design}$ (m^2)	$V_{DCHX,Design}$ (m^3)
400	4.0	1861000	1.21	0.537	0.648
450	4.0	1861000	1.71	0.537	0.919
490	4.0	1861000	2.10	0.537	1.131
550	4.0	1861000	2.53	0.537	1.361
600	4.0	1861000	2.79	0.537	1.497
650	4.0	1861000	2.97	0.537	1.597
700	4.0	1861000	3.11	0.537	1.671
750	4.0	1861000	3.21	0.537	1.726
800	4.0	1861000	3.28	0.537	1.765
850	4.0	1861000	3.34	0.537	1.793

P_{air} (kPa), operating pressure; $\dot{m}_{ECM}$ (kg/s), mass flowrate; $\dot{Q}$ (W), heat transfer rate; L_{DCHX} (m), DCHX length; $A_{CS,DCHX,Design}$ (m^2), DCHX cross-sectional area; $V_{DCHX,Design}$ (m^3), DCHX volume.

6.4.3 Particle initial velocity parametric study

In this part, the particle's initial velocity was varied while all other parameters remained constant in order to assess the effect of particle velocity on the DCHX design. The mass flow rate was set at 4.0 kg/s, and the terminal temperature difference was 50 K. The two tables below display the findings of the parametric research at operating pressures of 490 kPa and 800 kPa.

As seen in the data below, raising the particle's initial velocity had a negligible impact on the DCHX's performance. As the velocity of the particles increased, the heat exchanger length required to achieve the temperatures essential for the power cycle rose slightly. Changing the particle velocity did not affect the DCHX's cross-sectional area since it did not affect the heat transfer rate. By raising the initial velocity of the particle, the overall volume of this DCHX rose insignificantly, resulting in greater flexibility in the design options for this DCHX concept.

Table 20. Parametric study of initial particle velocity of 0.6 mm diameter at 490kPa air pressure.

$V_{p,0}$ (m/s)	$\dot{m}_{ECM}$ (kg/s)	$\dot{m}_{air}$ (kg/s)	$\dot{Q}$ (W)	L_{DCHX} (m)	$A_{CS,DCHX,Design}$ (m^2)	$V_{DCHX,Design}$ (m^3)
1.0	4.0	4.0	1861000	2.10	0.537	1.131
2.0	4.0	4.0	1861000	2.30	0.537	1.237
3.0	4.0	4.0	1861000	2.49	0.537	1.336
4.0	4.0	4.0	1861000	2.66	0.537	1.429
5.0	4.0	4.0	1861000	2.82	0.537	1.517

$V_{p,0}$ (m/s), initial particle velocity; $\dot{m}_{ECM}$ (kg/s), mass flowrate; $\dot{Q}$ (W), heat rate; L_{DCHX} (m), DCHX length; $A_{CS,DCHX,Design}$ (m^2), DCHX cross-sectional area; $V_{DCHX,Design}$ (m^3), DCHX volume.

Table 21. Parametric study of initial particle velocity of 0.6 mm diameter at 800 kPa air pressure.

$V_{p,0}$ (m/s)	$\dot{m}_{ECM}$ (kg/s)	$\dot{m}_{air}$ (kg/s)	$\dot{Q}$ (W)	L_{DCHX} (m)	$A_{CS,DCHX,Design}$ (m^2)	$V_{DCHX,Design}$ (m^3)
1.0	4.0	4.0	1861000	3.28	0.537	1.765
2.0	4.0	4.0	1861000	3.43	0.537	1.844
3.0	4.0	4.0	1861000	3.57	0.537	1.919
4.0	4.0	4.0	1861000	3.70	0.537	1.988
5.0	4.0	4.0	1861000	3.82	0.537	2.053

$V_{p,0}$ (m/s), initial particle velocity; $\dot{m}_{ECM}$ (kg/s), mass flowrate; $\dot{Q}$ (W), heat rate; L_{DCHX} (m), DCHX length; $A_{CS,DCHX,Design}$ (m^2), DCHX cross-sectional area; $V_{DCHX,Design}$ (m^3), DCHX volume.

6.4.4 Terminal temperature difference parametric study

To determine the influence of terminal temperature difference on the DCHX design, the terminal temperature difference was adjusted while all other parameters remained constant. The mass flow rate was set to 4.0 kg/s, and the particle's starting velocity was 1.0 m/s. The two tables below present the parametric study's results at operating pressures of 490 kPa and 800 kPa.

The results below demonstrate that increasing the terminal temperature difference enhances the performance of the DCHX. As the terminal temperature difference rose, the length of the heat exchanger required to reach the temperatures necessary for the power cycle decreased. Changing the terminal temperature difference did not change the DCHX's cross-sectional area since it did not affect the heat transfer rate. Increasing the terminal temperature difference lowered the total volume of this DCHX considerably.

Table 22. Parametric study of $LMTD_{spec}$ for 0.6 mm particle diameter at 1.0 m/s initial velocity and 490 kPa air pressure.

$LMTD_{spec}$ (K)	$\dot{m}_{ECM}$ (kg/s)	$\dot{m}_{air}$ (kg/s)	$\dot{Q}$ (W)	L_{DCHX} (m)	$A_{CS,DCHX,Design}$ (m^2)	$V_{DCHX,Design}$ (m^3)
20.0	4.0	4.0	1861000	4.14	0.537	2.222
30.0	4.0	4.0	1861000	3.12	0.537	1.676
40.0	4.0	4.0	1861000	2.51	0.537	1.349
50.0	4.0	4.0	1861000	2.10	0.537	1.131
60.0	4.0	4.0	1861000	1.81	0.537	0.975
70.0	4.0	4.0	1861000	1.60	0.537	0.857
80.0	4.0	4.0	1861000	1.42	0.537	0.765

$LMTD_{spec}$ (K), terminal temperature difference; $\dot{m}_{ECM}$ (kg/s), mass flowrate; $\dot{Q}$ (W), heat transfer rate; L_{DCHX} (m), DCHX length; $A_{CS,DCHX,Design}$ (m^2), DCHX cross-sectional area; $V_{DCHX,Design}$ (m^3), DCHX volume.

Table 23. Parametric study of $LMTD_{spec}$ for 0.6 mm particle diameter at 1.0 m/s initial velocity and 800 kPa air pressure.

$LMTD_{spec}$ (K)	$\dot{m}_{ECM}$ (kg/s)	$\dot{m}_{air}$ (kg/s)	$\dot{Q}$ (W)	L_{DCHX} (m)	$A_{CS,DCHX,Design}$ (m^2)	$V_{DCHX,Design}$ (m^3)
20.0	4.0	4.0	1861000	6.69	0.537	3.596
30.0	4.0	4.0	1861000	4.96	0.537	2.667
40.0	4.0	4.0	1861000	3.95	0.537	2.124
50.0	4.0	4.0	1861000	3.28	0.537	1.765
60.0	4.0	4.0	1861000	2.81	0.537	1.510
70.0	4.0	4.0	1861000	2.45	0.537	1.319
80.0	4.0	4.0	1861000	2.18	0.537	1.170

$LMTD_{spec}$ (K), terminal temperature difference; $\dot{m}_{ECM}$ (kg/s), mass flowrate; $\dot{Q}$ (W), heat transfer rate; L_{DCHX} (m), DCHX length; $A_{CS,DCHX,Design}$ (m^2), DCHX cross-sectional area; $V_{DCHX,Design}$ (m^3), DCHX volume.

6.5 Conclusion

This chapter discussed the importance of particle size in the DCHX design and found that a 0.6 mm particle diameter was practical. Also, some parametric experiments were conducted to determine the impact of the mass flow rate, initial particle velocity, operating pressure, and terminal temperature difference on the DCHX. These characteristics affected the performance of this direct-contact heat exchanger, as stated previously.

CHAPTER 7. CONCLUSION AND RECOMMENDATIONS

7.1 Conclusions

A summary of solar thermal energy, solar energy potential, and solar energy technology was provided. Then, the concentrated solar power methods including parabolic troughs, Fresnel reflectors, solar dishes, and solar towers were discussed. Several fluids utilized in solar tower applications for heat transmission were evaluated. It has become obvious that particle technology is gaining popularity in concentrated solar power research applications. Comprehensive literature research was conducted regarding the types of direct contact heat exchangers that can be employed in a solar tower, including fluidized bed heat exchangers, moving bed heat exchangers, cyclone heat exchanger, and falling particles heat exchangers. In addition, the falling particle direct contact heat exchanger was investigated in this thesis, and more study is still required.

Multiple materials and alloys were examined, including Stainless Steel 316, Stainless Steel 309, Inconel 625, Inconel 740H, and Haynes 282. Their thermal and mechanical characteristics were analyzed to determine their suitability to produce this DCHX. The most important considerations in selecting Stainless Steel 316 for the heat exchanger's body were allowable stress at elevated temperatures, creep rupture, melting points, and cost. Stainless steel should be suitable for the low-temperature components at the bottom, while superalloys may be best for high-temperature components that cannot be protected with internal insulation.

This thesis investigated the dynamical and thermal properties of falling particle heat exchangers that would be utilized in the RTV project's solar tower. This study examined the primary forces acting on falling particles in the heat exchanger body, the drag on spherical particles, and the heat transfer between particles and air. On the basis of this analysis and the power

cycles employed in the G3KSA project, a one-dimensional EES-based analytical model was constructed to simulate the thermal and dynamic performance of the heat exchanger. This DCHX was designed to operate at 490 kPa, which is compatible with the Aurelia A1300 turbine. In addition, the design simulated a working pressure of 800 kPa suitable with the General Electric Frame 5 turbine.

In this thesis, a simple steady-state simulation was implemented. In the future, a transient model should be considered, something more adaptable to Matlab rather than EES. In addition, some consideration must be given to polydisperse mixtures of particles. Possibly considering first the addition of some smaller and some larger particles. Certainly, a CFD model should then be considered before proceeding to even a small prototype for testing. Since the pressure in the DCHX is found to be almost constant, a simple finite element thermal and structural model should be adequate to investigate the pressure vessel and thermal insulation designs.

This thesis investigated the impact of particle size on the performance of a heat exchanger using particles with diameters of 0.3 mm, 0.6 mm, and 0.9 mm. The 0.6 mm particle diameter was determined to be the most practical of the three sizes. Using 0.6 mm particle diameter resulted in the smallest designed cross-sectional area of the DCHX and the smallest heat exchanger volume in order to fulfill the temperature design restriction.

At the two operating pressures, a parametric evaluation of the mass flow rate of air and particles was done. The mass flow rate was shown to have a substantial impact on the heat exchanger's performance. Increasing the mass flow rate enhances the dynamics and thermal performance of the heat exchanger, resulting in a reduced cross-sectional area and volume.

In order to examine what effect increasing the pressure would have, another parametric analysis was carried out on the operating pressure. The performance of the heat exchanger was found to be impacted by the operating pressure. When the air pressure was increased, air density increased, and its velocity decreased. As a result, the length of the heat exchanger also increased, which resulted in the volume of the heat exchanger growing as well.

An additional parametric analysis was conducted on initial particle velocity to evaluate the effect of increasing the velocity of the particles. The performance of the heat exchanger was found not to be affected by the initial particle velocity in any way. Because increasing the initial particle velocity had almost no impact on the length and volume of the heat exchanger, resulting in more flexibility in the allowable DCHX design.

In the end, a further parametric analysis was conducted on the terminal temperature velocity in order to explore the effect of raising the terminal temperature at the two different operating pressures. It was discovered that increasing the terminal temperature difference of the heat exchanger improved its overall performance. Increasing the terminal temperature difference improves the dynamics and thermal performance of the heat exchanger, leading to a shorter length for the heat exchanger and, consequently, a smaller volume for the heat exchanger.

7.2 Future Work and Recommendations

This research lays the groundwork for further investigations of falling particles direct contact heat exchangers utilized in solar towers. Nonetheless, some work was outside the scope of what was covered in this thesis. For example, the feeders, de-feeders, distribution systems, valves, and other parts should be explored and investigated.

In future research, it will be desirable to examine particles and substances that can be found locally in Saudi Arabia and are less costly and more effective. Therefore, more research is required to identify better materials than aluminum-based particles, such as olivine.

Insulation on the heat exchanger's interior and outside needs more investigation. To create a heat exchanger that is both efficient and cost-effective, additional materials for the body of the heat exchanger should be researched.

The EES model can also be slightly improved in the future by utilizing actual specific heats of particles and air rather than the average specific heat used in this model. This was done so that the model could be developed more easily.

A simple steady-state simulation was built in this thesis. Future research should examine a transient model that is more compatible with Matlab than EES. In addition, it is necessary to take polydisperse particle mixtures into account. Consider first the possibility of including both smaller and bigger particles. Before testing even a modest prototype, a CFD model should be considered. Since the particle volume is small compared to the fluid volume, the commonly accessible and moderately efficient dispersed particle tracking models in commercial CFD software should suffice for this investigation. Moreover, structural, and thermal considerations should be factored into the design process. A basic finite element thermal and structural model should be appropriate for investigating the pressure vessel and thermal insulation designs, given that the pressure in the DCHX is nearly constant.

In summary, a DCHX handling particles of reasonable size, around 0.6 mm, is projected to be very cost-effective in CSP applications, and further research on this technology is recommended.

APPENDIX A: DERIVATION OF PARTICLE VELOCITY

The particle velocity can be obtained using the Newton's 2nd Law. The main forces acting on the particle are the particle weight and the drag force

$$\sum F = m_p a \tag{46}$$

The net acceleration on the particle then found from the following equation, and particle velocity can be found using the acceleration.

$$a = \frac{F_g - F_D}{m_p} = \frac{d^2 y}{dt^2} = \frac{V_p \, dV_p}{dl} \tag{47}$$

$$\frac{V_p \, dV_p}{dl} = \frac{F_g - F_D}{m_p} \tag{48}$$

Reordering the equation and it became:

$$V_p \, dV_p = \frac{F_g - F_D}{m_p} dl \tag{49}$$

Taking the integral for both sides:

$$\int V_{\mathrm{p}}\, dV_{\mathrm{p}} = \int \frac{F_{\mathrm{g}} - F_{\mathrm{D}}}{m_{\mathrm{p}}}\, dl \tag{50}$$

Assume $\frac{F_{\mathrm{g}} - F_{\mathrm{D}}}{m_{\mathrm{p}}}$ is constant in each slice of the heat exchanger

$$\int V_{\mathrm{p}}\, dV_{\mathrm{p}} = \frac{F_{\mathrm{g}} - F_{\mathrm{D}}}{m_{\mathrm{p}}} \int dl \tag{51}$$

After the integration, the equation became as following:

$$\left[\frac{V_{\mathrm{p}}^2}{2}\right]_{l}^{l+dl} = \frac{F_{\mathrm{g}} - F_{\mathrm{D}}}{m_{\mathrm{p}}} \left[l\right]_{l}^{l+dl} \tag{52}$$

Substituting the values:

$$V_{\mathrm{p},l+dl}^2 - V_{\mathrm{p},l}^2 = 2\left(\frac{F_{\mathrm{g}} - F_{\mathrm{D}}}{m_{\mathrm{p}}}\right) dl \tag{53}$$

$$\left(V_{\mathrm{p},l+dl} - V_{\mathrm{p},l}\right)\left(V_{\mathrm{p},l+dl} + V_{\mathrm{p},l}\right) = 2\left(\frac{F_{\mathrm{g}} - F_{\mathrm{D}}}{m_{\mathrm{p}}}\right) dl \tag{54}$$

$$V_{\mathrm{p},l+dl} = \frac{2\left(\frac{F_{\mathrm{g}} - F_{\mathrm{D}}}{m_{\mathrm{p}}}\right)dl}{\left(V_{\mathrm{p},l+dl} + V_{\mathrm{p},l}\right)} + V_{\mathrm{p},l} \tag{55}$$

Reorganizing the equation

$$V_{\mathrm{p},l+dl} = \frac{2\left(F_{\mathrm{g}} - F_{\mathrm{D}}\right)dl}{m_{\mathrm{p}}\left(V_{\mathrm{p},l+dl} + V_{\mathrm{p},l}\right)} + V_{\mathrm{p},l} \tag{56}$$

The particles velocity at a certain slice will be calculated as the following

$$V_{\mathrm{p},j} = \frac{2\left(F_{\mathrm{g}} - F_{\mathrm{D},j}\right)dl}{m_{\mathrm{p}}\left(V_{\mathrm{p},j} + V_{\mathrm{p},j-1}\right)} + V_{\mathrm{p},j-1} \tag{57}$$

APPENDIX B: MOMENTUM BALANCE DERIVATION

Some assumptions were made perform momentum balance in the heat exchanger to simplify the analysis, such as:

- The flow is steady
- Inviscid flow
- Uniform flow

To derive the linear momentum equation, Newton's 2nd Law is used. The heat exchanger control volume is shown in Figure 42 [77].

$$\vec{F} = m\vec{a} = m\frac{d\vec{V}}{dt} = \frac{d\left(m\vec{V}\right)}{dt} \tag{58}$$

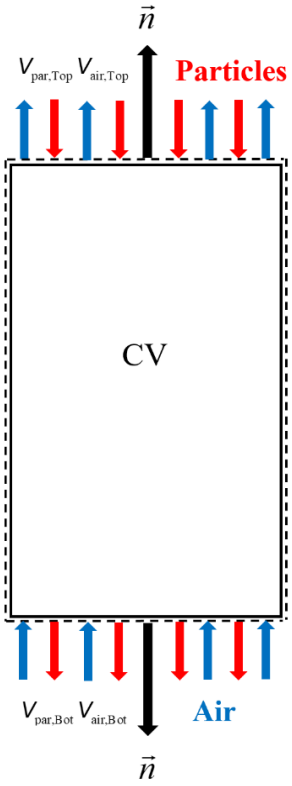

Figure 42: Schematic of the heat exchanger control volume.

To fully study the change of the flow momentum, both momentum inside the control volume, and momentum passing through the surface must be taken into consideration. The general form of the linear momentum equation for control volume is

$$\Sigma\vec{F} = \frac{d}{dt}\int_{CV}\rho\vec{V}\,dV + \int_{CS}\rho\vec{V}\left(\vec{V}\cdot\vec{n}\right)dA \tag{59}$$

The equation of the linear momentum shows that the summation of all the forces on the control volume is equal to the summation of momentum change inside the control volume, and flux of the momentum passing through the surface.

The flow is steady, hence; $\frac{d}{dt}\int_{CV} \rho\vec{V}\,dV$ is Zero. The remaining integral will be applied on the control surface and the momentum equation will be as follows:

$$\Sigma\vec{F} = \int_{CS} \rho\vec{V}\left(\vec{V}\cdot\vec{n}\right)dA \tag{60}$$

$\vec{n}$ is the unit normal vector, and it is positive outward and perpendicular to the control surface with a magnitude of 1. The dot product of the velocity and unit normal vectors are given as follows:

$$\vec{V}\cdot\vec{n} = \left|\vec{V}\right|\left|\vec{n}\right|\cos\theta \tag{61}$$

Where θ is the angle between the two vectors.

To apply the momentum balance on this direct contact heat exchanger, the forces on the control volume should be specified. Figure 43 illustrates the forces applied on the heat exchanger control volume.

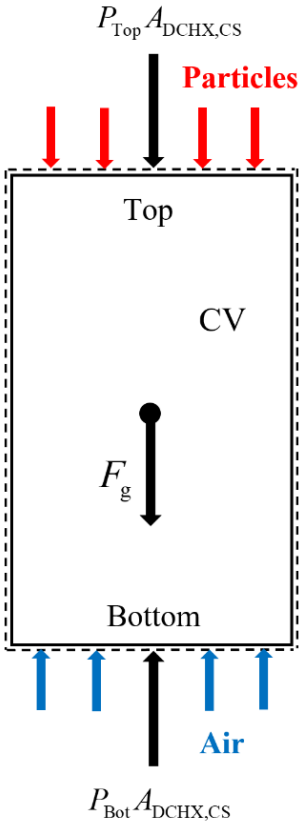

Figure 43: Schematic of the forces on heat exchanger control volume.

The integrals in the linear momentum equation will be applied only on the top and bottom surfaces. The integrals will not be applied on the heat exchanger walls due to the no-slip condition where the velocity is equal to zero. The momentum balance will be applied for both air and particles, and because it is a one-dimensional flow, only the vertical components are going to be used in the momentum balance. The vertical positive direction is pointing upward, hence; the equation will be derived as follows:

$$\Sigma F = \int_{CS} \rho V(V)\, dA_{DCHX,CS} = \int_{CS,air} \rho V(V)\, dA_{DCHX,CS} + \int_{CS,p} \rho V(V)\, dA_{DCHX,CS} \tag{62}$$

$$\Sigma F = \int_{\text{air,Bot}} \rho V\left(-V\right) dA_{\text{DCHX,CS}} + \int_{\text{air,Top}} \rho V\left(V\right) dA_{\text{DCHX,CS}} + \int_{\text{p,Top}} \rho V\left(-V\right) dA_{\text{DCHX,CS}} + \int_{\text{p,Bot}} \rho V\left(V\right) dA_{\text{DCHX,CS}} \tag{63}$$

$$\Sigma F = V_{\text{air,Bot}}\left(-\rho V A_{\text{DCHX,CS}}\right)_{\text{air,Bot}} + V_{\text{air,Top}}\left(\rho V A_{\text{DCHX,CS}}\right)_{\text{air,Top}} + V_{\text{p,Top}}\left(-\rho V A_{\text{DCHX,CS}}\right)_{\text{p,Top}} + V_{\text{p,Bot}}\left(\rho V A_{\text{DCHX,CS}}\right)_{\text{p,Bot}} \tag{64}$$

$$\Sigma F = -V_{\text{air,Bot}}\ \dot{m}_{\text{air,Bot}} + V_{\text{air,Top}}\ \dot{m}_{\text{air,Top}} - V_{\text{p,Top}}\ \dot{m}_{\text{p,Top}} + V_{\text{p,Bot}}\ \dot{m}_{\text{p,Bot}} \tag{65}$$

The mass flow rate for both the air and particles is constant

$$\dot{m}_{\text{air,Bot}} = \dot{m}_{\text{air,Top}} = \dot{m}_{\text{air}} \tag{66}$$

$$\dot{m}_{\text{p,Bot}} = \dot{m}_{\text{p,Top}} = \dot{m}_{\text{p}} \tag{67}$$

$$\Sigma F = \dot{m}_{\text{air}}\left(V_{\text{Top}} - V_{\text{Bot}}\right)_{\text{air}} + \dot{m}_{\text{p}}\left(V_{\text{Bot}} - V_{\text{Top}}\right)_{\text{p}} \tag{68}$$

The forces acting on the control volume are only the pressure and the weight and could be shown as following:

$$\Sigma F = P_{\text{Bot}} A_{\text{DCHX,CS}} - P_{\text{Top}} A_{\text{DCHX,CS}} - F_{\text{g}} \tag{69}$$

The momentum balance on the heat exchanger control volume will become:

$$P_{\text{Bot}} A_{\text{DCHX,CS}} - P_{\text{Top}} A_{\text{DCHX,CS}} - F_{\text{g}} = \dot{m}_{\text{air}}\left(V_{\text{Top}} - V_{\text{Bot}}\right)_{\text{air}} + \dot{m}_{\text{p}}\left(V_{\text{Bot}} - V_{\text{Top}}\right)_{\text{p}} \tag{70}$$

The pressure drop in this direct contact heat exchanger can be found with neglecting the weight of the air within the control volume from the following equation:

$$\left(P_{\text{Bot}} - P_{\text{Top}}\right) = \Delta P_{\text{DCHX}} = \frac{\dot{m}_{\text{air}}\left(V_{\text{Top}} - V_{\text{Bot}}\right)_{\text{air}} + \dot{m}_{\text{p}}\left(V_{\text{Bot}} - V_{\text{Top}}\right)_{\text{p}} + F_{\text{g,ECM}}}{A_{\text{DCHX,CS}}} \tag{71}$$

The weight is only the weight of the particles inside the control volume which can be found as the following:

$$F_{\text{g,ECM}} = g\, m_{\text{ECM}} \tag{72}$$

Since the heat exchanger in the model was divided into small slices, the mass of the particles in the control volume is going to be sum of the mass of all slices and can be found as shown below:

$$m_{\text{ECM}} = \sum_{j=1}^{\text{N\_steps}} \rho_{\text{N},j}\, m_{\text{p}}\, \Delta V_{\text{DCHX}} \tag{73}$$

APPENDIX C: PARTICLES PROPERTIES

Chemical composition of ACCUCAST ID50 particles, Aluminum-based particles, and the thermophysical properties are given in the tables below.

Table 24. Chemical composition of the particle *[78]*.

Compound	Weight %
Al_2O_3	75
SiO_2	11
Fe_2O_3	9
TiO_2	3

Table 25. Thermophysical properties of the particle *[78]*.

Property	Value	Unit
Loose Bed Density	113	lbs/ft^3
Packed Bed Density	125	lbs/ft^3
Thermal Expansion	0.708	%LC
Coefficient of Expansion	6.62	$1e^{-6}$ in/in-°C
Thermal Conductivity	0.70	W/m-°C
Heat Capacity	0.291	Cal/g-°C
Thermal Diffusivity	0.0029	cm^2/s
Heat Diffusivity	1.708	$10^6(W^2s)/(m^4\text{-}°C^2)$

APPENDIX D: DIRECT CONTACT HEAT EXCHANGER ALLOYS

There are more materials have been studied in this research and will be documented in this appendix.

1. **Stainless Steel 309:**

Another alloy designed for use in high-temperature applications is stainless steel 309. Stainless steel 309 has excellent oxidation resistance and can function in sulfuric mediums at high temperatures due to its high chromium and low nickel content. This steel type is exceptionally capable of welding and fabricating processes. Consequently, this alloy is appropriate for a wide range of industries, including petroleum refineries, power generation, heat exchangers, thermal processing, furnaces, aircraft and jet engine components, and paper mill equipment [79, 80].

Stainless steel 309 has significantly lower molybdenum content and higher chromium and nickel contents than 316 grade. The chemical composition of stainless steel 309 is given in Table 26 below [81].

Table 26. The chemical composition of the stainless steel 309 [81].

Material	**Weight %**
Carbon C	0.2
Manganese Mn	2.00
Phosphorus P	0.045
Sulfur S	0.03
Silicon Si	0.75
Chromium Cr	22.00 - 24.00
Nickel Ni	12.00 – 15.00
Molybdenum Mo	0.21
Nitrogen N	0.12
Iron Fe	Balance

Due to its increased chromium concentration, stainless steel 309 is more resistant to corrosion than most of the heat-resistant alloys. Consequently, stainless steel 309 can function at elevated temperatures without corroding. This metal can also function in sulfuric environments at extremely high temperatures. It has high resilience to the marine environment; hence, it could function in oxidizing mediums [81]. Therefore, stainless steel 309 is an excellent candidate for the corrosion-resistant construction of the heat exchanger's body.

The physical and mechanical properties of stainless steel 309 and the mean coefficient of thermal expansion were studied and are presented in the tables below to explore further this alloy's capability to be used in this DCHX [79].

Table 27. Physical properties of stainless steel 309 [79].

Property	**Value**
Density	7890 Kg/m^3
Specific Heat	502 J/kg-°K (0–100°C)
Modulus of Elasticity	196 GPa
Thermal Conductivity (100°C)	15.6 W/m-°K
Melting Range	1480–1530°C
Electrical Resistivity	78 μΩ-cm at 20°C

Stainless steel 309 has nearly identical physical qualities as stainless steel 316, making it a potential alternative alloy for use in the production of this DCHX. Stainless steel 309 has a higher range of melting temperatures than grade 316, which is higher than the air and energy carrier medium temperatures inside the heat exchanger, making it an excellent contender for the construction of this DCHX body.

The mean coefficient of the thermal expansion of this grade is shown in

Table 28 below [81]. As shown in the table, stainless steel 309 has an extensive range of temperatures with low thermal expansion. The stainless steel 309 has the same mean coefficient

of thermal expansion in the temperature range of 20 – 1000°C as the stainless steel 316. There is no significant difference between those two alloys.

Table 28. Mean coefficient of thermal expansion of stainless steel 309 [81].

Temperature range (°C)	**Value (mm/m °K)**
20–100	15.6
20–500	17.6
20–1000	19.4

The mechanical properties of the stainless steel 309, including the minimum tensile stress and minimum yield stress, and other properties, are shown in Table 29 [79].

Table 29. Mechanical properties of stainless steel 309 [81].

Property	**Value**
Min. tensile strength	515 MPa
Min. yield strength	205 MPa
Elongation in 50 mm	40 %
Max hardness, Rockwell B	95

As shown in the table above, the mechanical properties of stainless steel 309 at 20°C are the exact values for grade 316. The allowable stress of this alloy is studied and obtained from ASME BPVC and is presented in Figure 44 [61].

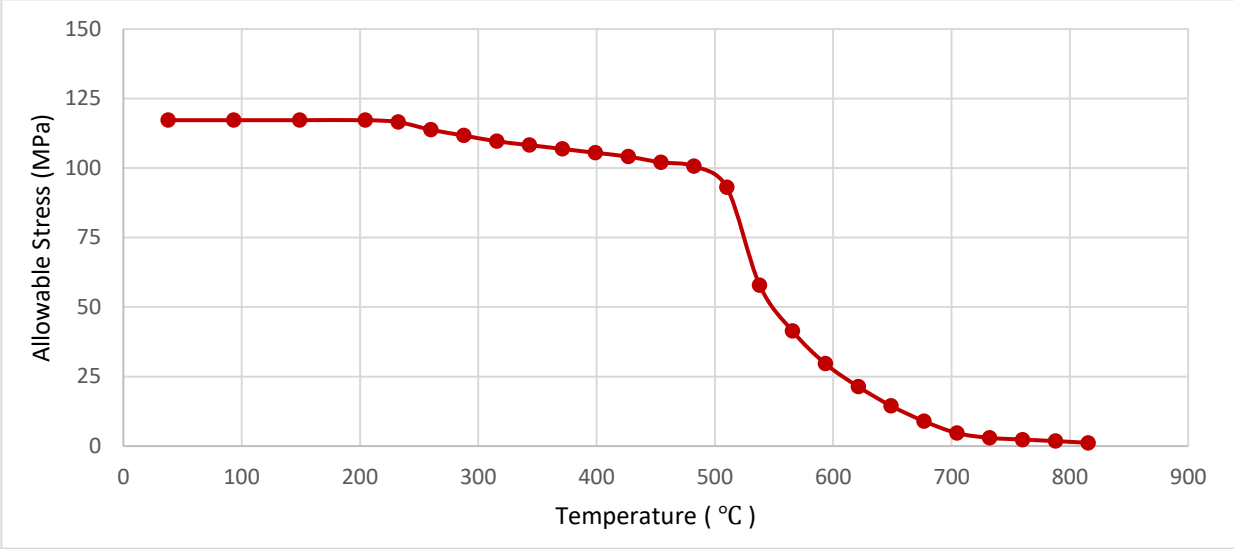

Figure 44. Stainless steel 309 allowable stress at elevated temperatures *[61]*.

According to the ASME BPVC, the allowable stress of stainless steel 309 has been determined and presented in the figure above. This alloy's allowable stress is less than that of stainless steel 316. However, the difference is not substantial. At 510°C, the allowable stresses for grades 316 and 309 are 106 MPa and 93 MPa, respectively. The stress curve exhibits the same behavior as stainless steel 316, in which the allowable stress drops gradually with increasing temperatures up to a high critical temperature, after which the stress curve declines drastically. The allowable stress at 815°C is approximately 1.25 MPa, which is significantly greater than the

operating pressure in this DCHX. The allowable stress study concludes that stainless steel 309 can withstand the pressure exerted within the heat exchanger without failing.

The creep rupture should be studied to comprehensively analyze the stainless steel 309 and its ability to be used for this heat exchanger's body design. The creep properties of stainless steel 309 are presented in the tables below [79]. The heat exchanger pressure is considerably lower than both the yield stress of the stainless steel 309 and all the creep stresses, as shown in the tables below. Therefore, stainless steel 309 is a good material for this heat exchanger design due to its good creep properties.

Table 30. Creep stress to produce 1% strain [81].

Temperature (°C)	Stress (MPa) to have a 1% strain	
	10,000 hours	100,000 hours
600	80	40
700	25	20
800	10	8
900	4	3
1000	2.5	1.5

Table 31. The creep rupture stress criterion [81].

Temperature (°C)	Stress (MPa) to have a rupture	
	1000 hours	10,000 hours
600	190	120
700	75	36
800	35	18
900	15	8.5
1000	8.0	4.0

Stainless steel 309 has good creep properties; however, stainless steel 316 has better creep values, giving grade 316 a slight advantage over grade 309. In conclusion, due to this extensive analysis, this grade is a great candidate for the construction of this DCHX.

2. Inconel 740H

Alloy 740H is an enhanced version of Inconel 740 due to improvements made to its chemical composition, resulting in much superior characteristics. Therefore, Inconel 740's commercial expansion ceased following the introduction of Inconel 740H [82]. Inconel 740H possesses exceptional features, such as high strength, excellent creep resistance, good corrosion and oxidation resistance, and superior ductility and weldability. In addition to its outstanding mechanical, physical, and thermal qualities, this alloy is appropriate for numerous industries. Inconel 740H is utilized in a variety of applications, including superheater boiler tubes, steam boiler chambers, and ultracritical steam boiler pipelines [83, 84].

The good features that this superalloy has are obtained mainly because of its chemical combination. The chemical composition of this alloy is presented in Table 32 below [85].

Table 32. The chemical composition of the Inconel 740H [85].

Material	**Weight %**
Carbon C	0.005 – 0.8
Manganese Mn	1.00
Phosphorus P	0.03
Sulfur S	0.03
Silicon Si	1.0
Chromium Cr	23.50 - 25.50
Nickel Ni	Balance
Molybdenum Mo	2.0
Niobium Nb	0.5 – 2.5
Iron Fe	3.0
Aluminum Al	0.2 – 2.0
Titanium Ti	0.5 – 2.5
Copper Cu	0.50
Boron B	0.0006 – 0.006
Cobalt Co	15.0 – 22.0

Due to its composition, Inconel 740H has demonstrated excellent corrosion resistance at extreme temperatures. Notably, the alloy's high chromium content makes it suitable for use in extremely corrosive settings. This material has use in boiler tubes, combustion gas, and coal ash [82]. Inconel 740H has a good resistance to oxidation due to its high chromium content. This superalloy offers excellent scaling resistance in both dry air and steam at elevated temperatures. All these characteristics encourage numerous businesses to adopt Inconel 740H for their designs [85]. Consequently, Inconel 740H could be a viable choice for use in this heat exchanger, in which air and particles are circulating without fear of corrosion. However, Inconel 740H will be examined further in this chapter to determine its other qualities and suitability for the body design of this heat exchanger.

The physical and mechanical properties and the mean coefficient of thermal expansion are studied to analyze the potentiality of this alloy in manufacturing the heat exchanger's body. Those essential characteristics are presented in the tables below [85].

Table 33. Physical properties of Inconel 740H [85].

Property	**Value**
Density	8050 Kg/m^3
Specific Heat	449 J/kg-°C (100°C)
Thermal Conductivity (100°C)	11.7 W/m-°C
Modulus of Elasticity	218 GPa
Melting Range	1288 – 1362°C
Electrical Resistivity	1.168μΩ-m

Inconel 740H has excellent physical attributes that are comparable to those of the preceding alloys. Consequently, this alloy is another good material that should be considered for use in the design of this DCHX. This alloy has the same melting temperature range as Inconel 625, which is greater than the air and energy carrier medium temperatures within the heat exchanger, making it an ideal contender for the construction of the DCHX body.

The mean coefficient of the thermal expansion of this metal is shown in Table 34 below [85]. As shown in the table, Inconel 740H has a broad spectrum of temperatures with low thermal expansion. The values of this alloy are slightly lower than those of Inconel 625 and stainless steel 316 and 309.

Table 34. Mean coefficient of thermal expansion of Inconel 740H [85].

Temperature range (°C)	**Value (µm/m°C)**
100	12.38
500	14.27
900	15.81

The mechanical properties of this metal at room temperature, including the minimum tensile stress, minimum yield stress, and other properties, are shown in Table 35 below [82].

Table 35. Mechanical properties of Inconel 740H [82].

Property	**Value**
Min. tensile strength	1035 MPa
Min. yield strength	620 MPa
Elongation in 50 mm	20 %

As shown in the table above, the Inconel 740H has much higher tensile and yield strength than all the previous alloys, which shows this metal's strength superiority. The allowable stress of this alloy is studied and obtained from ASME BPV codes and is presented in Figure 45 below [61].

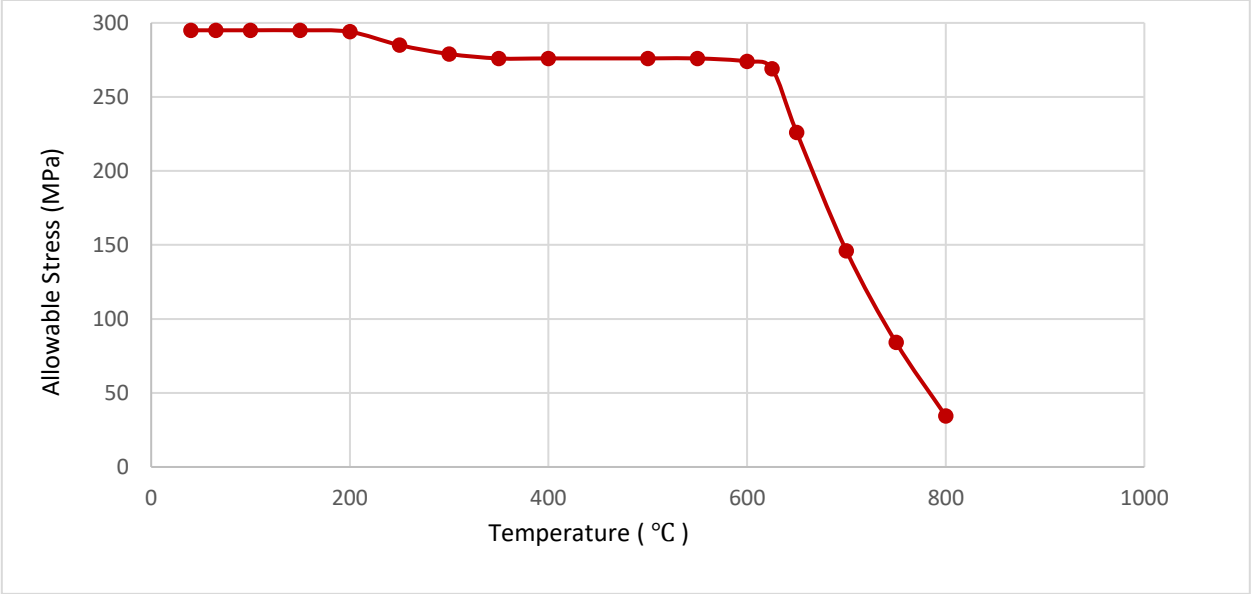

Figure 45. Allowable stress of Inconel 740H at elevated temperatures [61].

The allowable stress of Inconel 740H was obtained from ASME BPVC. This alloy has greater allowable stress than any of the preceding alloys. At 510°C, the maximum allowable stress for grades 316 and 309 is approximately 106 and 93 MPa, for Inconel 625 it is approximately 190 MPa, and for Inconel 740H it is approximately 276 MPa. At 800°C, the maximum allowable stress is roughly 9 and 1.3 MPa for alloys 316 and 309, respectively, whereas it is 34.5 MPa for Inconel 740H. Although stress curve exhibits the same behavior as those of the preceding metals, allowable stress falls gradually with increasing temperatures up to a high critical temperature, below which stress curve fall. This allowable stress curve demonstrates that Inconel 740H has higher stresses than the heat exchanger operating pressure. Therefore, there is no risk of failure associated with the use of Inconel 740H when subjected to this pressure.

Oak Ridge National Laboratory (ORNL) investigated and manufactured Inconel 740H rupture qualities based on a variety of products and compositions. The creep rupture is analyzed to determine the suitability of Inconel 740H for the body of this heat exchanger. The rupture life is depicted in the figure that follows [82]. As seen in the graph below, the heat exchanger pressure is considerably less than the yield stress of Inconel 625 and substantially less than all creep stresses. This superalloy is a suitable material for the construction of the body of this heat exchanger because of its high creep strength and characteristics.

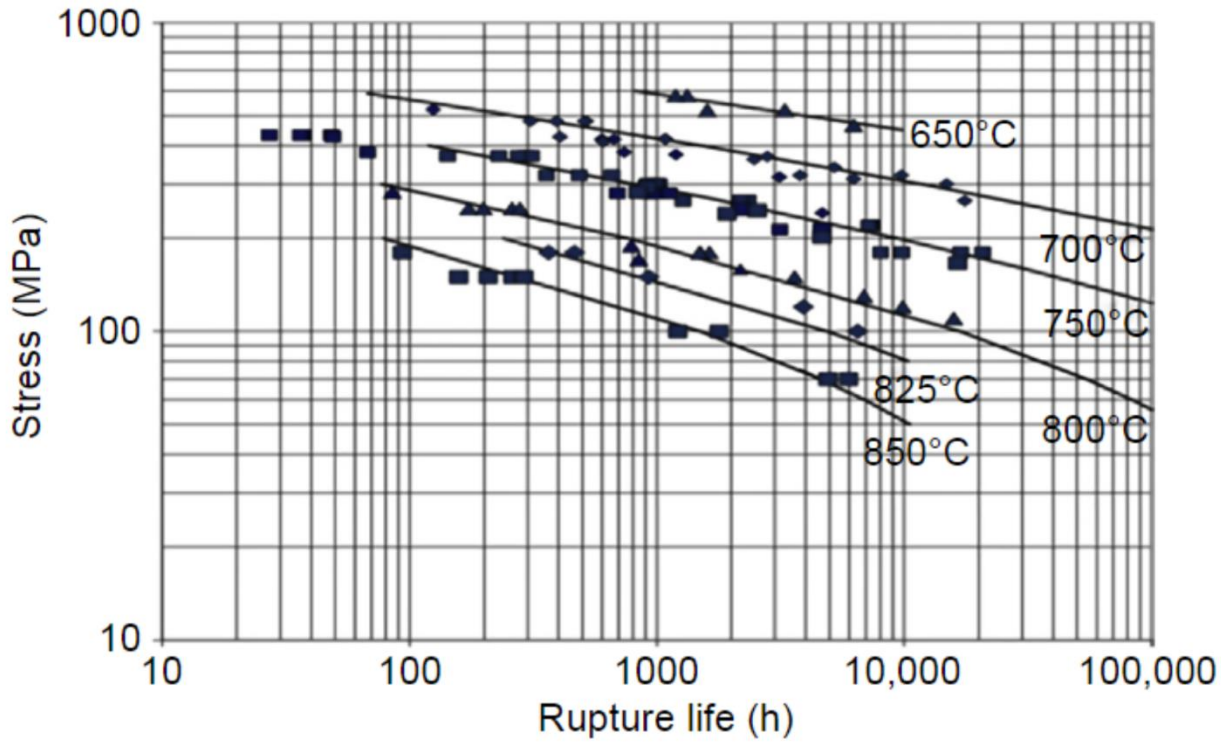

Figure 46. Creep strength of Inconel 740H [82].

3. Haynes 282

Haynes 282 is an additional nickel-based alloy created for high-temperature applications. This alloy possesses remarkable characteristics such as high strength, creep, thermal stability, fabricability, and weldability. The microstructure of Haynes 282, which includes carbides and borides, the generous inclusion of molybdenum, and the gamma-prime strengthening precipitates, which make the alloy weldable, all contribute to the alloy's exceptional properties.

This alloy was originally designed for use in aeronautical structural applications and land-based gas turbine engines. In addition, it is regarded as an excellent candidate material for application in sophisticated ultra-supercritical boiler and steam turbines, concentrating solar power plants, and supercritical carbon dioxide power cycles [86, 87].

There are several elements involved in the composition of Haynes 282. The chemical composition of this alloy is presented in Table 36 below [69].

Table 36. The chemical composition of the Haynes 282 [69].

Material	**Weight %**
Carbon C	0.04 - 0.08
Manganese Mn	0.30
Phosphorus P	0.015
Sulfur S	0.015
Silicon Si	0.15
Chromium Cr	18.50 - 20.50
Nickel Ni	Balance
Molybdenum Mo	8.00 - 9.00
Niobium Nb	0.20
Iron Fe	1.50
Aluminum Al	1.38 - 1.65
Titanium Ti	2.30
Copper Cu	0.10
Tantalum Ta	0.10
Boron B	0.003 - 0.010
Tungsten W	0.50
Cobalt Co	9.00 - 11.00

Nickel-based superalloys are good corrosion and oxidation-resistant metals, one of which is Haynes 282. It has good corrosion and oxidation resistance in several environments [87]. Some researchers have demonstrated that Haynes 282 can perform under extreme conditions, such as in environments with high levels of water vapor saturation, which accelerates the metal's corrosion rate. In addition, Haynes 282 has been researched in advanced supercritical settings, in which corrosion and oxidation are accelerated due to increased temperatures and pressures. However, no research has yet been undertaken on the Haynes 282's long-term performance under various conditions [82]. In this heat exchanger, the working materials, air, and particulates, are not highly corrosive, and the pressure within the heat exchanger chamber is not very high. Thus, Haynes 282 could be a suitable candidate for this DCHX body's design.

The physical and mechanical properties and the mean coefficient of thermal expansion are studied to examine the capability of this alloy in this heat exchanger's design. Those essential characteristics are presented in the tables below [69].

Table 37. Physical properties of Haynes 282 [69].

Property	**Value**
Density	8270 Kg/m^3
Specific Heat	463 J/kg-°C (100°C)
Thermal Conductivity (100°C)	12.0 W/m-°C
Modulus of Elasticity	213 GPa
Melting Range	1300-1375°C
Electrical Resistivity	127.8 μΩ-cm (100°C)

Haynes 282 has excellent physical properties and is comparable to the previous nickel-based alloys in terms of their values. The range of melting temperatures for Inconel 740H is identical, which is higher than the melting temperatures of working materials. Hence, this alloy is another ideal metal for use in the design of this DCHX.

The mean coefficient of the thermal expansion of this metal is shown in Table 38 [82]. The values of Haynes 282 are slightly higher than all the previous alloys.

Table 38. Mean coefficient of thermal expansion of Haynes 282 [82].

Temperature range (°C)	**Value (µm/m K)**
100	12.1
500	13.5
1000	16.9

The mechanical properties of this alloy at room temperature, including the minimum tensile stress, minimum yield stress, and other properties, are shown in the table below [69].

Table 39. Mechanical properties of Haynes 282 [69].

Property	**Value**
Min. tensile strength	1147 MPa
Min. yield strength	715 MPa
Elongation in 50 mm	30 %

As shown in the table above, the Haynes 282 has much higher tensile and yield strength than all the previous alloys, which shows this metal's strength superiority.

The allowable stress of this alloy is studied and obtained from Haynes International and is presented in Figure 47 below [69].

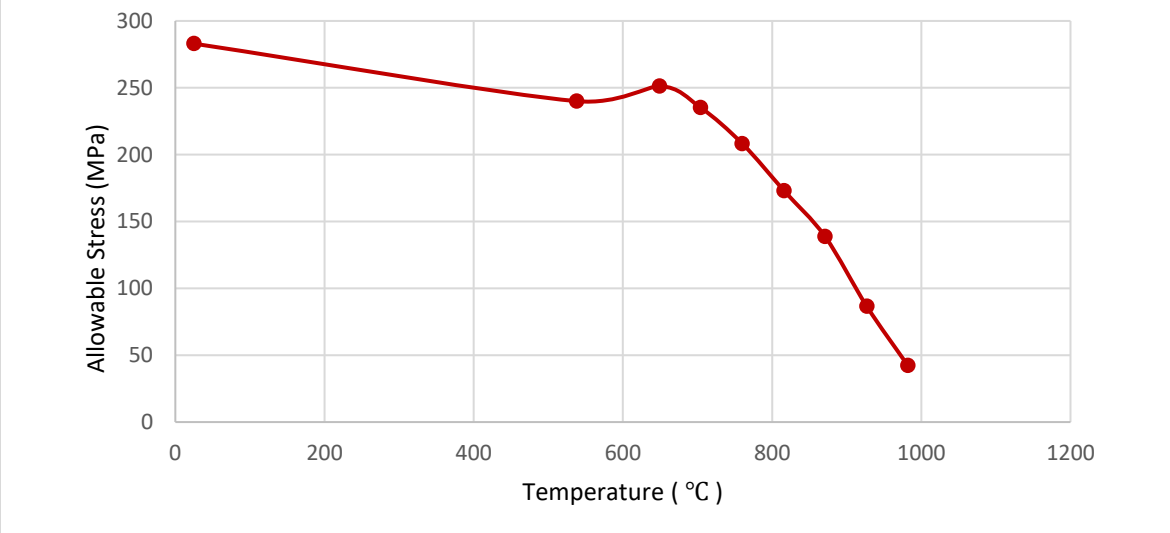

Figure 47. Allowable stress of Haynes 282 at elevated temperatures [69].

The allowable stress for Haynes 282 was obtained from Haynes International, the metal's developer. This alloy's allowable stress is greater than the previous four alloys. As anticipated, the curve exhibits the same behavior as the curves for the preceding metals. Allowed stress reduces slightly with increasing temperatures up to a high critical temperature, where the curve falls. This allowable stress curve demonstrates that Haynes 282 is subjected to greater stresses than the operating pressure exerted within the heat exchanger. Consequently, this metal can withstand this amount of force without breaking.

The Haynes 282 rupture properties were studied and produced by ORNL and other organizations. The studies show that this alloy has outstanding creep strength in the temperature range of 649 – 927°C, as presented in the tables below [69].

Table 40. Creep stress to produce 1% strain [69].

Temperature (°C)	Stress (MPa) to have a 1% creep	
	100 hours	1000 hours
649	-	545
704	496	365
760	331	241
816	221	145
871	124	69
927	62	34

Table 41. The creep rupture stress data [69].

Temperature (°C)	Stress (MPa) to have a rupture	
	100 hours	1000 hours
649	-	552
704	517	386
760	386	262
816	255	159
871	152	83
927	83	41

Studies indicate that the creep lifetime of Haynes 282 at 750°C and 100 MPa would approach 100,000 hours. In addition, these investigations indicate that Haynes 282 has a higher creep strength than Inconel 740H, making it one of the most robust materials for creep resistance [82]. This extensive analysis of Haynes 282 proves its potential to be used in the construction of this heat exchanger's body.

APPENDIX E: VERY PRELIMINARY COST ANALYSIS

This DCHX was assumed to consist of a thin inner shield made of a superalloy, an internal insulation layer, a shell made of stainless steel 316, an outer external insulation layer, particle distribution and recovery, and air inlet and outlet subsystems. The schematic below shows the DCHX.

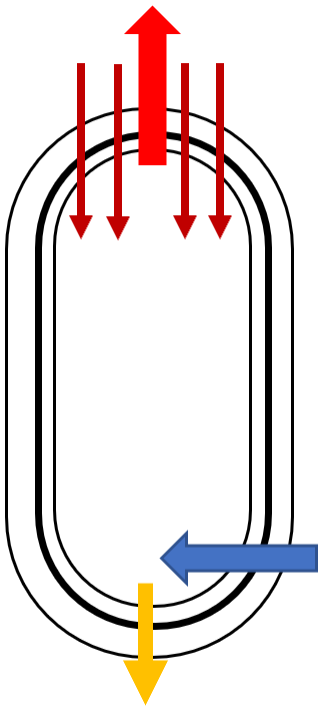

Figure 48. Schematic of DCHX showing inside out: superalloy shield, internal insulation, low alloy shell, and outer external insulation.

In this cost analysis, some assumptions were made to estimate the cost of this DCHX:

1. This DCHX is of a simple geometry with hemispherical heads.
2. There is an internal insulation layer to reach a moderate shell temperature.
3. The Total Cost (capital expenditure) is based on a simplistic material cost factor (MCF)
    a. Typical MCF for steel fabrication is 3 [88]; however, 4 was used to be more conservative.

The cost of materials that could be used in this DCHX are found to be:

1. The stainless steel 316 was found to be around 2.20 $/kg [63].
2. The Superalloy, e.g. Haynes 600; was found to be 20 times the price of stainless steel 316 [89]; which was expected to be much more expensive than the stainless steel 316.
3. The third important material used here is insulation. High-quality mineral wool insulation was estimated to be around 2060 $/m^3 [90].

A very thin shield was assumed to be placed between the internal insulation layer and heat exchanger volume to protect the insulation from the air and particles. This shield is of a thickness of 0.3 mm.

There are two layers of insulation, an external insulation layer and an internal layer placed between the shield and the shell. The overall insulation thickness was found to give a specified heat loss of 0.5% of the heat transfer rate. The internal insulation was distributed to give a specified shell temperature of 650°C.

The shell in this heat exchanger was assumed to be made of stainless steel 316 as the design hoop strength is 48MPa [61] with a specified temperature of 650°C, as mentioned above.

There are other internal components in this DCHX and they were estimated to be at 10% of shell mass, but they are made from superalloy material. These components include the following subsystems:

1. Particle distribution subsystem
2. Particle collection subsystem
3. Air distribution subsystem
4. Air discharge subsystem

Typical results:

The capital expenditure per kW-th was found to be 19 to 27 $/kW-th for 1.0 to 4.0 MW-th. The figure below shows the capital cost is slightly increasing with increasing the designed heat transfer rate, which was not expected. However, the DCHX costs are still well below the 150 $/kW-th target.

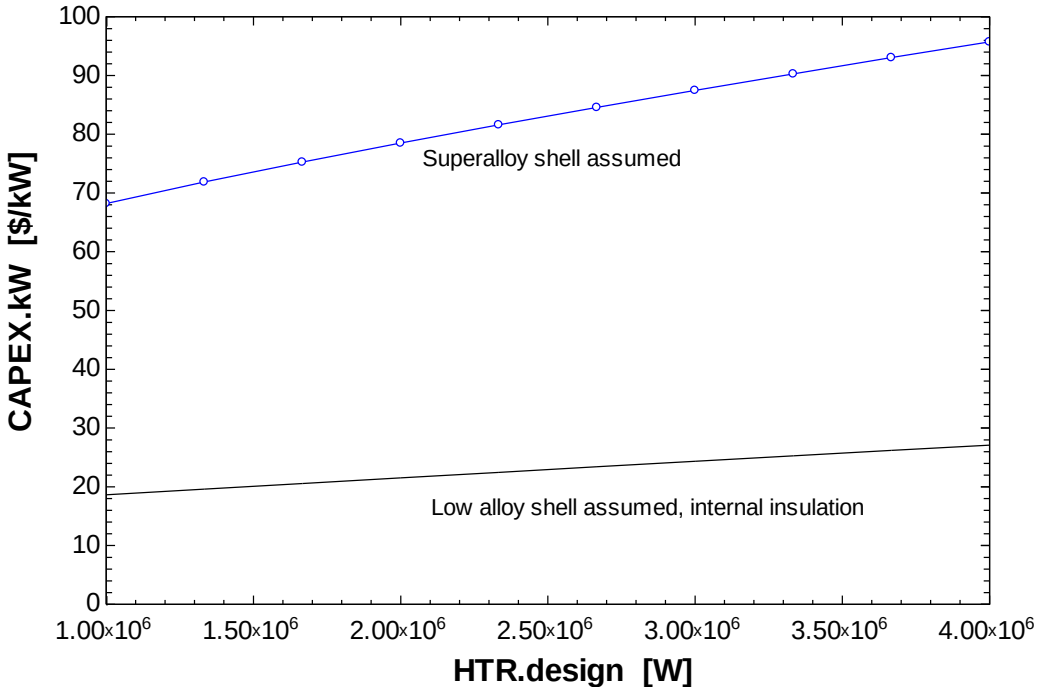

Figure 49. The capital expenditure at different designed heat transfer rates.

The figure above shows the importance of internal insulation in DCHX. When the shell was made of a superalloy, the cost for the same range of designed heat transfer rate increased exponentially. The capital expenditure per kW-th was found to be 69 to 95 $/kW-th for 1.0 to 4.0 MW-th, which way more expensive when the shell was made of stainless steel 316. This illustrates the DCHX design's internal insulating benefit.

Other costs for in-feeding and de-feeding components will be considerable but probably their cost will be acceptable.

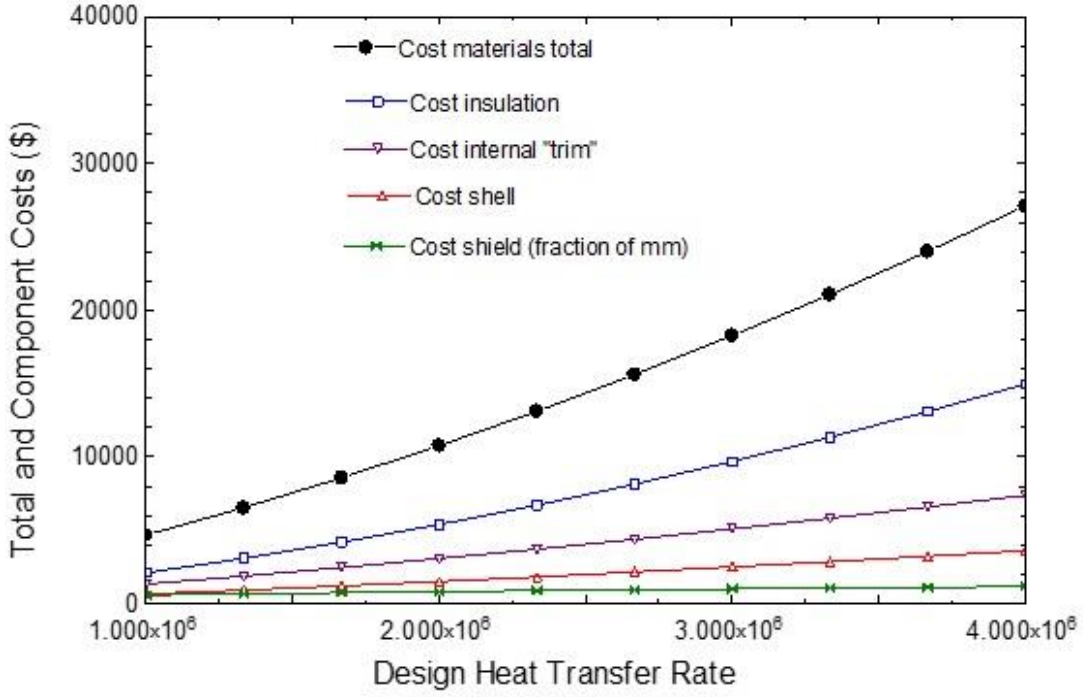

Figure 50. Cost of DCHX components at different design heat transfer rates.

The figure above shows the total cost and several component costs at different design heat transfer rates. As shown, the shield had the lowest cost since it was made of a very thin layer, then the shell since it was made from inexpensive metal. The cost of internal components had higher costs than the shield and shell as they were made of superalloy metals. However, the most expensive component in this DCHX was found to be the insulation. It is recommended that more investigation on insulation should be done. Even though the cost of insulation in this DCHX, it still had a great impact on the capital expenditure, as was shown in the previous figure. The cost of this DCHX without insulation is much higher than with insulation which indicates the importance of insulation in direct-contact heat exchangers.

APPENDIX F: EES MODEL FOR ONE-DIMENSIONAL DCHX

```
// DCHX sizing

Procedure heatlosscosting(Dia_CS_design, Length_TOP, T_P_avg, T_shell_est, P_abs, L_int, L_ext,
HTR.design : Area_shell, Q_dot_loss, T_shell_calc, cost.mat.total, CAPEX.total, CAPEX.kW,
cost.mat.shell, cost.mat.shield, cost.mat.trim, cost.mat.insulation)
// L_int=0.0[m]
//   L_ext=0.0[m]
    T_amb=(25+273)*1[K]
    //density_shell=density(Stainless_AISI316, T=T_shell_est)
    density_shield=density(Inconel_718, T=T_P_avg)

    k_int_typ=conductivity(Blanket_Al_silica_rho_48, T=1073[K])                    "similar to
Superwool k = 0.16 W/m-K at 800 C"

    T_int=0.5*(T_P_avg+T_shell_est)
    k_int=conductivity(Blanket_Al_silica_rho_48, T=T_int)
    R_V_int=L_int/k_int
    T_ext=0.5*(T_amb+T_shell_est)
    k_ext=conductivity(Blanket_Al_silica_rho_48, T=T_int)
    R_V_ext=L_ext/ k_ext
    R_V_total=R_V_int+R_V_ext
    U_value=1/R_V_total   "units should be W / m-sq K"

    P_g=P_abs-100.0[kPa]
    stress_design=48000[kPa]

    D_shell=Dia_CS_design+2*L_int
    L_shell=Length_TOP*(1.20)

    "allow for some extra cylindrical head and bottom space"
    Area_shell=pi*D_shell*L_shell+pi*D_shell^2   "add hemispherical heads to cylindrical shell"
    Area.HTF=Area_shell "area for heat loss"
    Area_shield=pi*Dia_CS_design*Length_TOP

   cost.shell.mass=1.0[$/lbm]*convert($/lbm, $/kg)
    cost.shield.mass=20*cost.shell.mass  "high temperature alloys are much more expensive than
common SS"
    cost.insulation.vol=(486[$]/8.33[ft^3])*convert($/ft^3, $/m^3)
    FCF=4.0 "conservative, based on commonly accepted assumption of 3"

    thick_shell=D_shell*P_g/(2*stress_design)
    vol_shell=thick_shell*Area_shell
    mass_shell=vol_shell*density_shell
    vol.ins_int=Area_shell*L_int
    vol.ins_ext=Area_shell*L_ext
    vol.ins_total = vol.ins_int+vol.ins_int

    vol.shield=Area_shield*.0003[m]
    mass_shield=vol.shield*density_shield
```

```
    vol.trim=0.10*vol_shell
    mass_trim=vol.trim*density_shield

    cost.mat.shell=mass_shell* cost.shell.mass
//  cost.mat.shell=mass_shell* cost.shield.mass "alternative superalloy shell"

    cost.mat.shield=mass_shield*cost.shield.mass
    cost.mat.trim=mass_trim*cost.shield.mass
    cost.mat.insulation=vol.ins_total*cost.insulation.vol

    cost.mat.total=cost.mat.shell+                    cost.mat.shield+cost.mat.trim+cost.mat.insulation
    cost.mat.kW=cost.mat.total/(HTR.design*convert(W, kW) )

    CAPEX.total=FCF*cost.mat.total
    CAPEX.kW=CAPEX.total/(HTR.design*convert(W, kW) )


    Q_dot_loss=U_value*Area.HTF*(T_P_avg-T_amb)
    T_shell_calc=T_P_avg-(T_P_avg-T_amb)*R_V_int/R_V_total


End

Procedure cp.id50(T_K: CP, h_mass)
    T_ND=T_K/1.0[K]
    CP=0.365[kJ/kg-K]*(T_ND-273.15)^0.18
    h_mass=0.30932[kJ/kg]*(T_ND-273.15)^1.18
End

Procedure sim.falling(MUX, N.steps, DELTAL, DELTAVOL : testn, error, Q_dot_HX, DELTAP.DCHX,
DELTAT.air.DCHX, DELTAT.par.DCHX, T_air_bot, T_p_bot, Num.density.avg,
Vel.par.avg,Vel.fluid.avg,DELTAP.drag.avg, DELTAP.mom.avg, Velocity.status$, Lside.particle)
$COMMON dia_p, Vol_p, mass_p, A_CS_p, grav, G_mass_air, G_mass_particle, C_dot_air,
C_dot_particle, P_air[0], T_f_in, T_air[0],  T_p[0], Vel[0], Vel_air[0], Area_sur_p, Area_CS_DCHX
$ARRAYS ON
n=0
testn=0

Fall[0]=0.0[m]
Vel_FF.TOP=VEL[0]
Vel_FF=Vel_FF.TOP
HT_on=1.0   "use HT_on to deactivate HT during debugging or modify HT performance"
// enhance resolution
ER.mux=1.0
N.steps=N.steps*ER.mux
DELTAL=DELTAL/ER.mux
DELTAVOL=DELTAVOL/ER.mux
Q_dot_HX=0.0[W]
Num.density.avg=0.0[1/m^3]
Vel.par.avg=0.0[m/s]
Vel.fluid.avg=0.0[m/s]
DELTAP.drag.avg=0.0[Pa]
DELTAP.mom.avg=0.0[Pa]
mass_PARS=0.0[kg]
Velocity.status$='Vel OK'
Repeat
```

```
n=n+1
//    Length[n]=Length[n-1]-DELTAL
    Fall[n]=Fall[n-1]+DELTAL
    Vel_air[n]=G_MASS_AIR/density(Air,T=T_air[n-1],P=P_air[n-1]) "air facial velocity"

   Vel.fluid.avg=Vel.fluid.avg+Vel_air[n]
//
    Vel_rel=Vel[n-1]+ Vel_air[n-1] "relative vel of air WRT particle for drag calculation"
// calculate drag based on calculated T and claculated relative velocity, use explicit known upstream
values
    Call dragprocedure(T_air[n-1], P_air[n-1], DIA_P, MASS_P, A_CS_P, Vel_rel, MUX : P_dyn_p, Re,
C_d_p_EES, gee_p, F_D_p, HTC_sphere)
//  Call dragprocedure(T_air[n-1], P_air[n-1], DIA_P, MASS_P, A_CS_P, Vel_rel, MUX : gee_p, F_D_p,
HTC_sphere)
    g_net=GRAV*gee_p
    g_net[n]=g_net "better to call this acceleration; a_cc[n] = g_grav * gee_ND"
//
//  Vel[n]=Vel[n-1]+g_net*DELTAL/(Vel[n-1]) "explicit formula"
   Arg=(Vel[n-1]*Vel[n-1] + 2*g_net*DELTAL)
    If (Arg <= 0.04[m^2/s^2]) Then

    Vel[n]=.2[m/s]

    Velocity.status$='LOW Vel Warn'
// NDensity_p=1/1.0[m^3]
    Else
                                                    Vel[n]=sqrt(Arg)
// NDensity_p=G_MASS_PARTICLE/ (mass_p*Vel[n] )
    Endif

    Vel.par.avg=Vel.par.avg+Vel[n]
   Vel_FF=Vel_FF+GRAV*DELTAL/Vel_FF
    NDensity_p=G_MASS_PARTICLE/ (mass_p*Vel[n] )
    mass_PARS=mass_PARS+NDensity_p*DELTAVOL*MASS_P

    NDensity_par[n]=NDensity_p
    Num.density.avg= Num.density.avg+NDensity_p
    Vol.particles.vol=NDensity_p*VOL_P "Vol fraction of Particles"
    Vol.air.vol[n]=1.00- Vol.particles.vol "Vol fractionn of Air"

    UA_particles= (NDensity_p*AREA_SUR_P*DELTAVOL)*HTC_sphere
// LMTD[n] approx the T difference
   LMTD=T_p[n-1] - T_air[n-1]
    Q_dot[n]=UA_particles*LMTD*HT_on
    DELTAT_air=Q_dot[n]*convert(W, kW)/C_dot_air
    DELTAT_PAR=Q_dot[n]*convert(W, kW)/C_dot_particle
    T_air[n]=T_air[n-1]-DELTAT_air
//
    T_p[n]=T_p[n-1]-DELTAT_PAR
    DELTAP_drag=NDensity_p*F_D_p*DELTAL "P drop due to drag on particles, N/sq-m or Pa"
    DELTAP.drag.avg=DELTAP.drag.avg+DELTAP_drag
    DELTAP_momentum=G_MASS_AIR*(Vel_air[n-1]-Vel_air[n]) "P drop due to acceleration of air, N/sq-
m or Pa"
    DELTAP.mom.avg=DELTAP.mom.avg+DELTAP_momentum
```

```
    P_air[n]=P_air[n-1]+(DELTAP_drag+DELTAP_momentum)*convert(Pa, KPa) "P ressure increses
downstream due to drag and acceleration"
   testn=testn+1
    Q_dot_HX=Q_dot_HX+Q_dot[n]

    If n =N.steps/2 Then
                                                HTC_sphere.typ=HTC_sphere
                                                Re.typ=Re
                                                k_solid=conductivity(Al_oxide_polycryst, T=T_p[n])
                                                Biot.num.typ=HTC_sphere.typ*DIA_P/ k_solid
                                                k_gas=conductivity(Air,T=T_air[n])
                                                Nu.num.typ=HTC_sphere.typ*DIA_P/ k_gas
                                                P.dyn.typ= P_dyn_p

                                                F_D_p.typ=F_D_p
    Endif
Until (n=N.steps)

Num.density.avg=                                Num.density.avg/N.steps
Vel.fluid.avg=Vel.fluid.avg/N.steps
Vel.par.avg=Vel.par.avg/N.steps
DELTAP.drag.avg=                                DELTAP.drag.avg/N.steps
DELTAP.mom.avg=                                 DELTAP.mom.avg/N.steps
Length.DCHX=Fall[n]
DELTAP.DCHX=P_air[n]-P_air[0]
DELTAT.air.DCHX=-T_air[n]+T_air[0]
DELTAT.par.DCHX=T_p[n]-T_p[0]
T_air_bot=T_air[n]
T_p_bot=T_p[n]

Vel_FF_calc =sqrt(VEL[0]*VEL[0]+2*GRAV*Length.DCHX)
Vel.PAR.out=Vel[n]

error=T_F_IN-T_air[n]  "how close does calculated air T approach design spec"
// volume per particle
Vol.DCHX= AREA_CS_DCHX*Fall[n]
Num.particles=Num.density.avg*Vol.DCHX
Vol.perparticle= Vol.DCHX/Num.particles
Lside.particle=(Vol.perparticle)^(1/3) "Representative Average Particle Spacing"

// overall force and momentum balance; vertical component, vertical positive
F_P=DELTAP.DCHX*AREA_CS_DCHX*convert(kPa, Pa)
F_G=mass_PARS*GRAV
MF_PAR= -G_MASS_PARTICLE*AREA_CS_DCHX*(Vel[n]-Vel[0])
MF_fluid= G_MASS_AIR*AREA_CS_DCHX*(Vel_air[0]-Vel_air[n])
F_CV=F_P-F_G
NETMF=MF_PAR+MF_fluid
//
End

Procedure  dragprocedure(T_air, P_air, dia_p, mass_p, A_CS_p, Vel_rel, MUX : P_dyn_p, Re,
C_d_p_EES, gee_p, F_D_p, HTC_sphere)
//  Procedure  dragprocedure(T_air, P_air, dia_p, mass_p, A_CS_p, Vel_rel, MUX : gee_p, F_D_p,
HTC_sphere)
gav=9.81[m/s^2]
fluid$='air'
```

```
// MUX can be a drag multiplier If needed; eg for rough particles, etc

nu_vis=kinematicviscosity(fluid$,T=T_air,P=P_air)
Pr_air=prandtl(fluid$,T=T_air)
rho_air=density(fluid$,T=T_air,P=P_air)
k_th=conductivity(fluid$,T=T_air)

Vel_rel= Vel_rel
P_dyn_p=rho_air*Vel_rel^2/2

// HTC and drag and net force and NU on nominal size particle
Re=dia_p*Vel_rel/nu_vis

Call external_flow_sphere_nd(Re, Pr_air: Nusselt_p_air, C_d_p_EES)
HTC_sphere=Nusselt_p_air*k_th/ dia_p

F_D_p=MUX* C_d_p_EES*A_CS_p*P_dyn_p
F_G=mass_p*gav
gee_p=(F_G-F_D_p)/F_G  "this is non-dimensional gee, multiplier of gravitational acceleration"

End

// Equation Set begins here
N_steps=200

HT_on = 1 "eg 1 if HT enabled"
fluid$='Air'
P_0=100[kPa]
T_0=300[K]
// CL_fill=0.075[m]/2
MUX=1.0 "adjustment factor for drag; If needed from experiment"
// Vel_p_0=2.0[m/s] "important consideration: vel of particles before encountering air current"
DELTAT_fluid=400[K]
// dia_p=0.000800[m]


T_f_in=converttemp(C, K, 661[C]) "inlet temperature, based on power cycle requirement"
T_f_out=T_f_in + DELTAT_fluid "outlet temperature, based on power cycle requirement; defines length
LEN of exchanger"
T_f_avg=(T_f_out+T_f_in)/2 "average air T"

LMTD_spec=50[K]
T_particle=T_f_avg+LMTD_spec "defines the particle average T, based on fluid T and reasonable Delta-
T"

P_M50=837[kPa]
P_A400=490[kPa]
P_f=P_A400
// P_f=800[kPa]
// P_f=P_0
h_fluid_in=enthalpy(Air, T=T_f_in)
h_fluid_out=enthalpy(Air, T=T_f_out)
Cp_air=(h_fluid_out-h_fluid_in)/DELTAT_fluid

// consider normalizing these mass flows
$IFNOT PARAMETRICTABLE
```

```
    HTR.design=1.0*1.0E6[W]
    m_dot_particle=4.0[kg/s]
//  m_dot_particle=4.0[kg/s]
    Vel_p_0=1.0[m/s]
    T_shell_spec=(650+273)*1[K]
    F_LOSS_spec=.005

$ENDIF
m_dot_fluid=m_dot_particle "note this typical approximation"
Area_CS_DCHX=1.0[m^2]  "nominal 1.0 sq-m cross section for analysis; scale the cross section for other
HTF rate"


// nom G_MASS_PARTICLE=6.922 [kg/s-m^2]
G_mass_particle=m_dot_particle/ Area_CS_DCHX
G_mass_air=m_dot_fluid/ Area_CS_DCHX
G_mass_air=Vel_air_avg*rho_air_avg

// some example calculations
P_air=P_f
T_air=T_f_avg
rho_air_avg=density(Air,T=T_air,P=P_air)
rho_air_top=density(fluid$,T=T_f_out,P=P_air)
rho_air_BOT=density(fluid$,T=T_f_in,P=P_air)
Vel_air_TOP=G_mass_air/rho_air_top
Vel_air_BOT=G_mass_air/rho_air_BOT
DELTAP_mom_HX=G_mass_air*(Vel_air_TOP-Vel_air_BOT)

rho_accucast_bulk=1810[kg/m^3]
Cp_accucast=1.160[kJ/kg-K]
rho_accucast_particle=rho_accucast_bulk/0.6
rho_accucast_bulk_lbm=rho_accucast_bulk*convert(kg/m^3, lbm/ft^3)
rho_accucast_particle_lbm=rho_accucast_particle*convert(kg/m^3, lbm/ft^3)
rho_alumina= density(Al_oxide_polycryst, T=300[K])


rho_p=rho_accucast_particle
A_CS_p=pi*dia_p^2/4
Vol_p=pi*dia_p^3/6
Area_sur_p=4*A_CS_p
mass_p=Vol_p*rho_p

Vel_p=Vel_p_0
G_mass_particle=NDensity_p_0*mass_p*Vel_p_0

// calculate drag force and HTC at average fluid properties and particle inlet velocity (only nominal)
Call dragprocedure(T_air, P_air, dia_p, mass_p, A_CS_p, Vel_p, MUX : P_dyn_p, Re, C_d_p_EES,
gee_p, F_D_p, HTC_sphere)
grav=9.81[m/s^2]
acc_p=grav*gee_p

acc_FF=grav

// L_mux=3  "moved to diagram window"

Length_TOP=1.0[m]*L_mux
```

```
Length_BOT=0.0[m]

DELTAL=Length_TOP/N_steps
Length[0]=Fall[0]
Fall[0]=0.0[m]
VEL[0]=Vel_p_0 "Vel is particle velocity"
P_AIR[0]=P_air
VEL_AIR[0]=G_MASS_AIR/rho_air_TOP
T_f_est=T_f_out-DELTAT_fluid*Fall[0]/Length_TOP
T_AIR[0]=T_f_out
T_air_calc[0]=T_f_out
T_P[0]=T_f_out+LMTD_spec "this TTD fixes the particle inlet T; hot particle T"
T_p_in=T_p[0]
// summary specs
T_f_in_C=converttemp(K, C, T_f_in)
T_f_out_C=converttemp(K,C, T_f_out)
T_P_in_C=converttemp(K, C, T_p[0] )
T_P_out_C=converttemp(K, C, T_f_in+LMTD_spec )
T_P_out=T_f_in+LMTD_spec
T_P_avg=(T_P_out+T_P_in)/2

Call cp.id50(T_P_in: CP_in, h_mass_in)
Call cp.id50(T_P_out: CP_out, h_mass_out)
Call cp.id50(T_P_avg: CP_avg, h_mass_avg)


C_dot_air=Cp_air*G_mass_air*Area_CS_DCHX
C_dot_particle=CP_avg*G_mass_particle*Area_CS_DCHX


DELTAVol=DELTAL*Area_CS_DCHX

Call sim.falling(MUX, N_steps, DELTAL,DELTAVOL : testn, error.sim, Q_dot_HX.sim, DELTAP.DCHX,
DELTAT.air.DCHX, DELTAT.par.DCHX, T_air_bot, T_p_bot, Num.density.avg, Vel.par.avg,Vel.fluid.avg,
DELTAP.drag.avg, DELTAP.mom.avg, Velocity.status$, RPS.particle)

// T_air_bot = T_f_in
error= T_air_bot - T_f_in
error=0  "EES iterates the simulation top find the proper length of DCHX to satisfy this design constraint"

Q_dot_HX=Q_dot_HX.sim
Q_dot_HX_nom=Q_dot_HX " nominal HTR for simulation"

//prelim sizing data
// Heat Transfer Rate, HTR per unit CS area:
HTR.CSarea=Q_dot_HX/ Area_CS_DCHX
// design DCHX for specified HTR
// HTR.design=1.0*1.0E6[W] "see above"
Area_CS_design=HTR.design/ HTR.CSarea
Dia_CS_design=sqrt(4*Area_CS_design/pi)
Vol_active_design=Area_CS_design*Length_TOP
HTR.Vol=Q_dot_HX/Vol_active_design
Vol_active_design.gal=Vol_active_design*convert(m^3, gal)
{L_int=0.2[m]
L_ext=0.3[m] }
T_shell_est=T_shell_spec
```

```
HTR.design.MW =HTR.design*convert(W, MW)

Call heatlosscosting(Dia_CS_design, Length_TOP, T_P_avg, T_shell_est, P_f, L_int, L_ext, HTR.design
: Area.shell, Q_dot_loss, T_shell_calc, cost.mat.total, CAPEX.total, CAPEX.kW, cost.mat.shell,
cost.mat.shield, cost.mat.trim, cost.mat.insulation)
L_TOTAL = L_int+L_ext
F_LOSS=Q_dot_loss/Q_dot_HX
F_LOSS=F_LOSS_spec
T_shell_calc=T_shell_est
// Q_dot_loss=.005*Q_dot_HX


//prelim cost data
{Vol_active_DCHX=Area_CS_DCHX*Length_TOP
Vol_active_DCHX_gals=Vol_active_DCHX*convert(m^3,gal)
Vol_gross_DCHX=Area_CS_DCHX*(Length_TOP+2[m])*1.3
Vol_gross_DCHX_gals=Vol_gross_DCHX*convert(m^3,gal)
HT_density=Q_dot_HX/ Vol_active_DCHX
HT_CSarea=Q_dot_HX/Area_CS_DCHX}
```

REFERENCES

[1] U.S. Energy Information Adminstration, "International Energy Outlook 2021," 6 10 2021. [Online]. Available: https://www.eia.gov/outlooks/ieo/pdf/IEO2021_ReleasePresentation.pdf. [Accessed 19 09 2022].

[2] U.S. Energy Information Adminstration, "U.S. Electricity Generation by Energy Source," 02 2022. [Online]. Available: https://www.eia.gov/tools/faqs/faq.php?id=427&t=3. [Accessed 19 09 2022].

[3] V. Sivaram, Taming the Sun: Innovations to Harness Solar Energy and Power the Planet, 1st ed., The MIT Press, 2018.

[4] B. F. Towler, The Future of Energy, Cambridge: Academic Press, 2014, p. 600.

[5] Global Solar Atlas, "Global Solar Atlas," 2019. [Online]. Available: https://globalsolaratlas.info/download/world. [Accessed 20 09 2022].

[6] P. Breeze, Power Generation Technologies, 3rd ed., Newnes, 2019.

[7] M. . A. Hanif , F. Nadeem and U. Rashid, Renewable and Alternative Energy Resources, 1st ed., Cambridge: Academic Press, 2021.

[8] American Chemical Society, "American Chemical Society," 2014. [Online]. Available: https://www.acs.org/content/acs/en/education/resources/highschool/chemmatters/past-issues/archive-2013-2014/how-a-solar-cell-works.html#:~:text=When%20sunlight%20strikes%20a%20solar,to%20the%20p%2Dtype%20layer.. [Accessed 24 09 2022].

[9] O. Kwon, S. Lee and J. Park, "A numerical study to compensate duck curve of ESS integrated gas turbine system with reused-battery," *Journal of Energy Storage,* Vols. 55, Part A, p. 105422, 2022.

[10] A. A. İnada, S. Arman and B. Safaei, "A novel review on the efficiency of nanomaterials for solar energy storage systems," *Journal of Energy Storage,* Vols. 55, Part C, p. 105661, 2022.

[11] U. D. o. Energy, "U.S. Department of Energy," [Online]. Available: https://www.energy.gov/eere/solar/solar-integration-solar-energy-and-storage-

basics#:~:text=The%20most%20common%20type%20of,(fluids)%20with%20CSP%20plants.. [Accessed 27 09 2022].

[12] Y. Jiang, L. Duan, M. Yang, Y. Tong and L. Pang, "Performance analysis of tower solar aided coal-fired power plant with thermal energy storage," *Applied Thermal Engineering*, vol. 206, p. 118101, 2022.

[13] K. Lovegrove and W. Stein, Concentrating Solar Power Technology : Principles, Developments, and Applications, 2nd ed., Elsevier Science & Technology, 2020.

[14] P. Breeze, Solar Power Generation, 1st ed., Cambridge: Academic Press, 2016.

[15] M. Blanco, Advances in Concentrating Solar Thermal Research and Technology, 1st ed., Cambridge: Woodhead Publishing, 2016.

[16] A. Madhlopa, Solar Receivers for Thermal Power Generation, 1st ed., Cambridge: Academic Press, 2022.

[17] A. K. Azad, Advances in Clean Energy Technologies, 1st ed., Cambridge: Academic Press, 2020.

[18] M. Geyer and C. Prieto, Storing Energy: with Special Reference to Renewable Energy Sources, 2nd ed., Elsevier, 2022.

[19] S. Revankar, Storage and Hybridization of Nuclear Energy: Techno-economic Integration of Renewable and Nuclear Energy, 1st ed., Cambridge: Academic Press, 2018.

[20] S. Qazi, Standalone Photovoltaic (PV) Systems for Disaster Relief and Remote Areas, 1st ed., Elsevier, Elsevier.

[21] M. Parzen, *Comparison Of Heat Transfer Fluids for Solar Tower Systems*, 2017.

[22] H. Zhang, H. Benoit, D. Gauthier, J. Degrève, J. Baeyens, I. P. López, M. Hemati and G. Flamant, "Particle circulation loops in solar energy capture and storage: Gas–solid flow and heat transfer considerations," *Applied Energy*, vol. 161, pp. 206-224, 1 1 2016.

[23] F. Nie, Z. Cui, F. Bai and Z. Wang, "Properties of solid particles as heat transfer fluid in a gravity driven moving bed solar receiver," *Solar Energy Materials and Solar Cells*, vol. 200, p. 110007, 15 9 2019.

[24] S. Alaqel, *An Experimental Investigation of Particle-to-Working Fluid Counter-Flow Direct-contact Heat Exchanger*, Riyadh, 2021.

[25] F. P. Incropera, D. P. DeWitt, T. L. Bergman and A. S. Lavine, Fundamentals of Heat and Mass Transfer, 6 ed., Hoboken: John Wiley & Sons, 2006.

[26] S. S. M. Murshed and M. M. Lopes, Heat Exchangers - Design, Experiment and Simulation, London: In Tech Open, 2017.

[27] R. K. Shah and D. P. Sekulic, Fundamentals of heat exchanger design, Hoboken: John Wiley & Sons, 2002.

[28] M. J. Lee and S. W. Kim, "Preparation of MWCNT microbeads for the application of bed materials in a fluidized bed heat exchanger," *MDPI,* vol. 13, no. 6, p. 10, 2020.

[29] C. Wu, H. Yang, X. He, L. Yang and H. Li, "Principle, development, application design and prospect of fluidized bed heat exchange technology: Comprehensive review," *Renewable and Sustainable Energy Reviews,* vol. 157, p. 17, 2021.

[30] Z. Ma, J. C. Gifford, P. G. Davenport and X. Wang, "Fluidized-Bed Heat Exchanger for Conversion of Thermal Energy to Electricity". United States Patent WO2022015919, 20 01 2022.

[31] H. J. Green, C. M. Leboeuf and M. S. Bohn, "Technical and Economic Evaluation of A Solid-Particle/Air Direct-Contact Heat Exchanger," Solar Energy Research Institute, U.S. Department of Energy, 1986.

[32] S. Alaqel, N. Saleh, R. Saeed, E. Djajadiwinata, M. Sarfraz, A. Alswaiyd, H. Al-Ansary, O. Zeitoun, S. Danish, Z. Al-Suhaibani, A. El-Leathy, S. Jeter and A. Khayyat, "A novel particle-to-fluid direct-contact counter-flow heat exchanger for CSP power generation applications: Design features and experimental testing," *Renewable Energy,* vol. 170, pp. 905-926, 2021.

[33] S. Alaqel, N. Saleh, R. Saeed, E. Djajadiwinata, M. Sarfraz, A. Alswaiyd, H. Al-Ansary, O. Zeitoun, S. Danish, Z. Al-Suhaibani, A. El-Leathy, S. Jeter and A. Khayyat, "Particle-to-fluid direct-contact counter-flow heat exchanger: Simple-models validation and integration with a particle-based central tower system," *Case Studies in Thermal Engineering,* vol. 33, p. 101994, 2022.

[34] J. D. Hertel and S. Zunft, "Experimental validation of a continuum model for local heat transfer in shell-and-tube moving-bed heat exchangers," *Applied Thermal Engineering,* vol. 206, p. 11, 4 2022.

[35] S. I. Park, "Performance analysis of a moving-bed heat exchanger in vertical pipes," *Energy,* vol. 21, no. 10, p. 8, 1996.

[36] C. G. Hill, Introduction to Chemical Engineering Kinetics & Reactor Design, Second ed., Hoboken: John Wiley & Sons, 2014.

[37] S. T. Science, "direct Versus Indirect Heating Technology, SOLEX Thermal Science," 02 2022. [Online]. Available: https://www.solexthermal.com/assets/Resources/Direct-vs-Indirect-Heating-and-Cooling.pdf.

[38] J. Hertel, M. Ebert, L. Amsbeck, B. Gobereit, J. Rheinländer, A. Hirt and C. F. Cathy Frantz, "Development and Test af a Direct Contact Heat Exchanger (Particle - Air) for Industrial Process Heat Applications," in *ASME 13th International Conference on Energy Sustainability*, Bellevue, 2019.

[39] T. D. Hadley, Y. Pan, K.-S. Lim and J. Orellana, "Engineering design of direct contact counter current moving bed heat exchangers," *International Journal of Mineral Processing*, vol. 142, p. 10, 2015.

[40] A. Jain, B. Mohanty, B. Pitchumani and K. S. Rajan, "Studies on Gas-Solid Heat Transfer in Cyclone Heat Exchanger," *Journal of Heat Transfer, ASME,* vol. 128, no. 8, pp. 761-768, 2006.

[41] A. Shimizu, T. Yokomine and T. Nagafuchi, "Development of gas–solid direct contact heat exchanger by use of axial flow cyclone," *International Journal of Heat and Mass Transfer*, vol. 47, no. 21, pp. 4601-4614, 2004.

[42] M. S. Sagoo, "The development of a falling cloud heat exchanger—Air and particle flow and heat transfer," *Journal of Heat Recovery Systems*, vol. 1, no. 2, pp. 133-138, 1981.

[43] M. J. Frain, D. P. Schmidt and W. A. Fiveland, "An Experimental Investigation of the Influence of Gas and Solid Particle Interaction on the Heat Transfer Effectiveness of a Falling-Bed Heat Exchanger," *Journal Heat Transfer, ASME,* vol. 127, no. 10, pp. 1077-1086, 2005.

[44] R. W. Fox, A. T. McDonald and J. W. Mitchell, Fox and McDonald's Introduction to Fluid Mechanics, Hoboken, New Jersey: John Wiley & Sons, INC, 2020.

[45] G. Bagheri and C. Bonadonna, "On the drag of freely falling non-spherical particles," *Powder Technology*, vol. 301, pp. 526-544, 2016.

[46] R. Clift and W. H. Gauvin, "Motion of entrained particles in gas streams," *Journal of Chemical Engineering*, vol. 49, no. 4, pp. 439-448, 1971.

[47] M. J. Rhodes, Introduction to Particle Technology, Hoboken: John Wiley & Sons, 2008.

[48] S. Whitaker, "Forced convection heat transfer correlations for flow in pipes, past flat plates, single cylinders, single spheres, and for flow in packed beds and tube bundles.," *AIChE Journal*, vol. 18, no. 2, pp. 361-371, 1972.

[49] W. Ranz and W. Marshall, "Evaporation from Drops," *Chemical Engineering Progress,* vol. 48, pp. 141-146, 1952.

[50] N. Ellendt, A. M. Lumanglas, S. I. Moqadam and L. Mädler, "A model for the drag and heat transfer of spheres in the laminar regime at high temperature differences," *International Journal of Thermal Sciences,* vol. 133, p. 98–105, 2018.

[51] A. Calderon, C. Barreneche, A. Fernandez and M. Segarra, "Thermal cycling test of solid particles to be used in concentrating solar," *Solar Energy Materials and Solar Cells,* vol. 222, p. 110936, 2021.

[52] T. Tan and Y. Chen, "Review of study on solid particle solar receivers," *Renewable and Sustainable Energy Reviews,* vol. 14, p. 265–276, 2010.

[53] M. I. Khan, F. Asfand and S. G. Al-Ghamdi, "Progress in technology advancements for next generation concentrated solar power using solid particle receivers," *Sustainable Energy Technologies and Assessments,* vol. 54, p. 102813, 2022.

[54] R. K. Imam, *Development of a Direct Contact Heat Exchanger for a PArticle Heating Concentrator Solar Power Application,* Atlanta: Georgia Institute of Technology, 2018.

[55] D. Mills, Pneumatic Conveying Design Guide, Oxford: Butterworth-Heinemann, 2004.

[56] M. J. Frain, D. P. Schmidt and W. A. Fiveland, "An Experimental Investigation of the Influence of Gas and Solid Particle Interaction on the Heat Transfer Effectiveness of a Falling-Bed Heat Exchanger," *Journal of Heat Transfer, ASME,* vol. 127, pp. 1077-1086, 2005.

[57] H. Wang, Z. Shi, X. Yaer, Z. Tong and Z. Du, "High mechanical performance of AISI304 stainless steel plate by surface nanocrystallization and microstructural evolution during the explosive impact treatment," *Journal of Materials Research and Technology,* vol. 8, no. 1, p. 6, 2019.

[58] X. Guo, P. Lei, C. Mohanty and T. Yao, "Enhanced crevice corrosion of stainless steel 316 by degradation of Cr-containing hollandite crevice former," *Corrosion Science,* vol. 205, p. 15, 2022.

[59] Sandmeyer Steel, "Sandmeyer Steel Company," 6 2014. [Online]. Available: https://www.sandmeyersteel.com/images/316-316l-317l-spec-sheet.pdf. [Accessed 25 6 2022].

[60] F. A. Leckie and D. J. Bello, Strength and Stiffness of Engineering Systems, New York: Springer, 2009.

[61] ASME, *Boiler and Pressure Vessel Code,* ASME, 2017.

[62] M. E. Kassner, Fundamentals of Creep in Metals and Alloys, third, Ed., Butterworth-Heinemann, 2015.

[63] North American Stainless, "North American Stainless," 10 2010. [Online]. Available: https://www.northamericanstainless.com/wp-content/uploads/2010/10/Grade-316-316L1.pdf. [Accessed 22 6 2022].

[64] North American Stainless, "North American Stainless," 10 2010. [Online]. Available: https://www.northamericanstainless.com/wp-content/uploads/2010/10/Grade-309S.pdf. [Accessed 25 6 2022].

[65] V. Shankar, K. B. S. Rao and S. L. Mannan, "Microstructure and mechanical properties of Inconel 625," *Journal of Nuclear Materials,* vol. 288, no. 2-3, p. 11, 2001.

[66] Metals, High Temp, "High Temp Metals," 2015. [Online]. Available: https://www.hightempmetals.com/techdata/hitempInconel625data.php. [Accessed 27 6 2022].

[67] F. Chen, Q. Wang, C. Zhang, Z. Huang, M. Jia and Q. Shen, "Microstructures and mechanical behaviors of additive manufactured Inconel 625 alloys via selective laser melting and laser engineered net shaping," *Journal of Alloys and Compounds,* vol. 917, p. 11, 5 10 2022.

[68] Special Metals, "Special Metals," 27 8 2013. [Online]. Available: https://www.specialmetals.com/documents/technical-bulletins/inconel/inconel-alloy-625.pdf. [Accessed 27 06 2022].

[69] Haynes International;, "Haynes International," 10 12 2021. [Online]. Available: https://haynesintl.com/docs/default-source/pdfs/new-alloy-brochures/high-temperature-alloys/brochures/282-brochure.pdf?sfvrsn=20. [Accessed 29 06 2022].

[70] S. Tran-Cong, M. Gay and E. EMichaelides, "Drag coefficients of irregularly shaped particles," *Powder Technology,* vol. 139, no. 1, pp. 21-32, 2004.

[71] M. Duan, Y. Wang, D. Wang, G. Da, L. Liu and Y. Yang, "Modeling dynamic variation of drag force acting on single hot particle," *Powder Technology,* vol. 344, pp. 432-442, 2019.

[72] N. Gat, "The Circulating Balls Heat Exchanger (CIBEX)," *Journal of Thermophysics and Heat Transfer,* vol. 1, pp. @article{Gat1986TheCB,, 1986.

[73] J. H. Park, S. W. Baek and S. Kwon, "Analysis of a Gas-Particle Direct-Contact Heat Exchanger with Two-Phase Radiation Effect," *Numerical Heat Transfer Applications,* vol. 33, no. 7, pp. 701-721, 1998.

[74] E. Saatdjian and J. F. Large, "Heat Transfer in a Countercurrent, Gas–Solid, Packed Column," *Journal of Heat Transfe,* vol. 110, no. 2, pp. 385-389, 1988.

[75] E. Achenbach, "Heat and flow characteristics of packed beds," *Experimental Thermal and Fluid Science,* vol. 10, no. 1, pp. 17-27, 1995.

[76] A. Liu, S. Liu, Y. Duan and Z. Pan, "Numerical simulation of heat transfer in a gas solid crossflow moving packed bed heat exchanger," *Journal of Thermal Science volume,* vol. 10, no. 3, pp. 228-232, 2001.

[77] Y. A. Çengel and J. M. Cimbala, Fluid Mechanics: Fundamentals and Applications, New York: McGraw-Hill, 2006.

[78] R. C. Knott, *High-Temperature Durability of Metals for Use in a Particle Heating Receiver for Concentrated Solar Power.,* Atlanta: Georgia Institute of Technology, 2014.

[79] Sandmeyer Steel Company, "Sandmeyer Steel Company," 6 6 2014. [Online]. Available: https://www.sandmeyersteel.com/images/Alloy309-SpecSheet.pdf. [Accessed 24 6 2022].

[80] J. A. Lichtenfeld, C. J. Van Tyne and M. C. Mataya, "Effect of Strain Rate on Stress-Strain Behavior of Alloy 309 and 304L Austenitic Stainless Steel," *Metallurgical and Materials Transactions A,* vol. 37, p. 15, 1 2006.

[81] Penn Stainless Products, "Penn Stainless Products," 7 2013. [Online]. Available: https://www.pennstainless.com/wp-content/plugins/wonderplugin-pdf-embed/pdfjslight/web/viewer.html?v=2&file=https%3A%2F%2Fwww.pennstainless.com%2Fwp-content%2Fuploads%2F2018%2F11%2FPSP-108-Alloy309.pdf. [Accessed 25 6 2022].

[82] J. J. de Barbadillo, Materials for Ultra-Supercritical and Advanced Ultra-Supercritical Power Plants, Cambridge: Woodhead Publishing, 2016.

[83] J. J. de Barbadillo, B. A. Baker, R. D. Gollihue and S. A. McCoy, "Properties Of Inconel Alloy 740h For High Pressure Steam And Supercritical Co2 Applications," in *The ASME 2018 Symposium on Elevated Temperature Application of Materials for Fossil, Nuclear, and Petrochemical Industries,* Seattle, 2018.

[84] A. Zielinski, M. Sroka and T. Dudziak, "Microstructure and Mechanical Properties of Inconel," *MDPI,* p. 13, 30 10 2018.

[85] PCC Energy Group, "PCC Energy Group," 13 5 2015. [Online]. Available: https://www.specialmetals.com/documents/technical-bulletins/inconel/inconel-alloy-740h.pdf. [Accessed 28 6 2022].

[86] M. Komarasamy, C. Smith, J. Darsell, W. Choi, S. Jana and G. Grant, "Microstructure and mechanical properties of friction stir welded Haynes 282," *Materials Characterization,* vol. 182, p. 8, 2021.

[87] b. S. Shaikh, F. Schulz, K. Minet-Lallemand and E. Hryha, "Microstructure and mechanical properties of Haynes 282 superalloy produced by laser powder bed fusion," *Materials Today Communications,* vol. 26, p. 12, 2021.

[88] CostOwl, "How Much Does Metal Fabrication Cost," 2021. [Online]. Available: https://www.costowl.com/home-improvement/other/other-metal-fabrication-cost/.

[89] Material Properties, "Costs of Superalloys," [Online]. Available: https://material-properties.org/what-are-costs-of-superalloys-inconel-price-definition/. [Accessed 12 2022].

[90] Grainger, "Ceramic Fiber Blanket," Grainger, 2022. [Online]. Available: https://www.grainger.com/product/UNITHERM-Ceramic-Fiber-Blanket-25-ft-34DA11.

[91] "Particle-to-fluid direct-contact counter-flow heat exchanger: Simple-models validation and integration with a particle-based central tower system," *Case Studies in Thermal Engineering,* vol. 33, p. 101994, 2022.

[92] B. F. Towler, The Future of Energy, Academic Press, 2014.

[93] M. . A. Hanif , F. Nadeem and U. Rashid, Renewable and Alternative Energy Resources, 1st ed., Academic Press, 2021.

[94] O. Kwon, S. Lee and J. Park, "A numerical study to compensate duck curve of ESS integrated gas turbine system with reused-battery," *Journal of Energy Storage,* vol. 55, p. 12, 2022.

[95] A. A. İnada, S. Arman and B. Safaei, "A novel review on the efficiency of nanomaterials for solar energy storage systems," *Journal of Energy Storage,* vol. 55, p. 25, 2022.

[96] Y. Jiang, L. Duan, M. Yang, Y. Tong and L. Pang, "Performance analysis of tower solar aided coal-fired power plant with thermal energy storage," *Applied Thermal Engineering,* vol. 206, p. 13, 2022.

[97] P. Breeze, Solar Power Generation, 1st ed., Academic Press, 2016.

[98] A. Madhlopa, Solar Receivers for Thermal Power Generation, 1st ed., Academic Press, 2022.

[99] A. K. Azad, Advances in Clean Energy Technologies, 1st ed., Academic Press, 2020.

[100] S. Revankar, Storage and Hybridization of Nuclear Energy: Techno-economic Integration of Renewable and Nuclear Energy, 1st ed., Academic Press, 2018.

[101] H. Zhang, H. Benoit, D. Gauthier, J. Degrève, J. Baeyens, I. P. López, M. Hemati and G. Flamant, "Particle circulation loops in solar energy capture and storage: Gas–solid flow and heat transfer considerations," *Applied Energy*, vol. 161, p. 19, 2016.

[102] F. Nie, Z. Cui, F. Bai and Z. Wang, "Properties of solid particles as heat transfer fluid in a gravity driven moving bed solar receiver," *Solar Energy Materials and Solar Cells*, vol. 200, p. 16, 2019.

[103] C. Nunez, "Deserts, explained," National Geographic, [Online]. Available: https://www.nationalgeographic.com/environment/article/deserts.

[104] NREL, "Solar resources maps and data," 22 02 2018. [Online]. Available: https://www.nrel.gov/gis/solar-resource-maps.html.

[105] U.S. Energy Information Adminstration, "U.S. Energy Information Amdinstration," 08 12 2021. [Online]. Available: https://www.eia.gov/tools/faqs/faq.php?id=87&t=1.